Lens Based High Directivity Simultaneous Transmit and Receive Systems

by

Carlos A. Mulero Hernández

B.S., University of Puerto Rico, Mayagüez Campus, 2014

M.S., University of Puerto Rico, Mayagüez Campus, 2016

A thesis submitted to the

Faculty of the Graduate School of the

University of Colorado in partial fulfillment

of the requirements for the degree of

Doctor of Philosophy

Department of Electrical, Computer and Energy Engineering

2021

Committee Members:

Dejan S. Filipović, Chair

Mohamed A. Elmansouri

Zoya B. Popović

Alan S. Brannon

Neil W. Kefauver

Mulero Hernández, Carlos A. (Ph.D., Electrical Engineering, Antenna Design)

Lens Based High Directivity Simultaneous Transmit and Receive Systems

Thesis directed by Prof. Dejan S. Filipović

Simultaneous transmit and receive (STAR) has the potential to theoretically double the capacity of wireless networks making it a highly desirable technology for modern wireless systems. Self interference (SI) is the chief challenge and high Tx/Rx isolation (greater than 100 dB) is required to mitigate this issue and realize STAR operation. The required isolation level is typically achieved by using a multi-layer cancellation approach across the antenna, analog, and digital domains [1]. A well-designed antenna or propagation layer can provide a significant portion of the SI cancellation (SIC) enabling simplified and more practical transceiver realization. For typical wireless networks and electronic warfare systems, monostatic or shared-aperture STAR antennas are often required to maintain the aperture compactness. At millimeter waves, high directivity and beam steering characteristics are highly desired; particularly for access point and backhaul antennas, to overcome the path loss, achieve the required communication range, and improve the signal-to-noise ratio in dynamic multi-user environments.

A co-polarized, co-channel STAR antenna system utilizing a two-layer, spherically stratified lens with nominal directivity of 24.3 dBic is demonstrated in the 27 to 29 GHz frequency band. The STAR operation is achieved with a WR28 waveguide-implemented balanced circulator beam forming network (BC-BFN), which relies on two 90° hybrids and two circulators along with antenna symmetry to cancel the circulator leakages and achieve theoretically infinite isolation between the transmit and receive ports. The sensitivity of the BC-BFN to alignment and other imperfections is studied. To comply with the BC-BFN's symmetry requirements, a highly symmetric WR28 waveguide ortho-mode transducer (OMT) is developed. Tx/Rx isolation of 30 and 34 dB is measured with and without the lens, respectively, indicating acceptable impact of the lens on system isolation. To demonstrate STAR with the beam steering in an equatorial field of view, the pro-

posed configuration is modified into a mechanically rotated half spherical lens over a ground plane. The experiments show that the isolation of the rotating half-lens system degrades compared to the full-lens counterpart due to the break of the geometrical symmetry. However, respectable isolation greater than 27 dB and high quality circularly polarized radiation patterns are still maintained over the operational bandwidth.

Another co-polarized, co-channel, lens-based STAR system based of the same BC-BFN and OMT subsystem but using a compact planar graded index (GRIN) lens is also introduced. The compact lens achieves broadside directivity greater than 24 dBic in the band centered about 28 GHz. The beams are steered by mechanically rotating the proposed compact lens, maintaining the focal point on the antenna's phase center. A maximum scan loss of 4.5 dB is seen in an 80° conic field of view while preserving system isolation. The measured system maintains 30 dB of isolation with at most 2 dB degradation in isolation at the more severe inclination angles.

Finally, closed-form expressions are derived for the component of the radar cross section (RCS) due to the BFN in the context of retrodirective systems. The ability to accurately predict the effect of feedback and infinite reflections is shown with numerical simulations. The derived equations allow calculating the bounds for the maximum loop gain for the system before feedback leads its response into the non-linear domain. The potential of using STAR to improve the performance of retrodirective systems is evaluated with the spherical lens antenna and BC-BFN subsystem. Improvements of 20 dB are obtained when data from the fabricated STAR system is used in the equation and compared to passive lens reflectors.

Dedication

To us.

Acknowledgements

I would like to express my gratitude to my advisor, Prof. Dejan Filipović for his endless support, patience, motivation, and guidance. Didn't think I'd make it a few times-thank you. Special appreciation also goes out to Dr. Maxim Ignatenko and Dr. Mohamed Elmansouri who have been involved in my research at different points of my time here as well as to Ljubodrag Bošković who provided invaluable support for every fabrication.

I would like to thank the members of my thesis committee: Prof. Popović, Dr. Brannon, and Dr. Kefauver for their time, comments, encouragements, and efforts to evaluate my research.

I would like to thank all the postdoctoral fellows, graduates students, and alumni from the Antenna Research Group and RF Group, especially: Dr. Ha, Dr. Abdelraham, Dr. Etellisi, Dr. Valaleprasannakumar, Liliana Rodriguez, Conrad Andrews, Aman Samaiyar, Jake Cazden, Selena Leitner, Merarys A. Caquías Olivera, Theodore Prince, Dong-Chan Son, Gaeron Friedrichs, Songyi Yen, Laila Marzall, Dakotah Simpson, Andrea Ashley, Dan Fishler, Chanci King, Amy Robinson, Dr. Tianang, Dr. Pack, Dr. Sanghai, Dr. Hoel, Dr. Pinto, Bradley Allen, Sean Mckee, Milica Notaros, Roger Hasse, Emmanuel Valentín Hernández, and many many others. Thank you for enriching my academic life with frienship and camaraderie.

Most importantly, I'll never be able to thank my family enough for the support they have always provided. Thank you to my girlfriend, Jessica, who has been patient and encouraging while I finish this work. Thanks to Dr. Osvaldo, Pacheco, Phillip, and Carlitos who don't let distance or time get in the way of our friendship. Lastly, thank you to Dr. Rafael Rodriguez Solis who gave me the chance and set me on the path to become an RF engineer.

Contents

Chapter

Tables

Table

Figures

Figure

Chapter 1

Introduction

1.1 Simultaneous Transmit and Receive

Simultaneous transmit and receive (STAR), also known as in-band full-duplex(IBFD) operation, improves data rate and spectral efficiency of RF communications; both are important for an effective use of the congested electromagnetic spectrum. These improvements come about from STAR avoiding duplexing. In time domain duplexing, as shown in Fig. 1.1(a), each base station would have to take turns between listening and transmitting. Frequency domain duplexing, represented in Fig. 1.1(b) would have both base-stations transmit at the same time but at different frequencies, allowing only half the bandwidth for data transfer. STAR has both base stations simultaneously transmit and receive on the same frequencies, maximizing time and spectrum use. The self-interference (SI) from higher power-transmitted (Tx) signal to the co-located receiver (Rx) is what renders the STAR realization to be extremely challenging. Depending on the Tx power, channel bandwidth, and system electronics the SI cancellation on the order of 100 to 150 dB is required to fully suppress the coupled signals [1, 5]. To achieve this level of SI elimination, the cancellation stages on antenna, analog, and digital domains are commonly considered [6, 7].

STAR antenna subsystems can be broadly divided into four categories: bistatic, quasi-monostatic, monostatic, and hybrid. Bistatic systems utilize two spatially separated antennas and generally rely on the path loss, surface treatment [8], and pattern shaping to achieve high SI cancellation (SIC). In quasi-monostatic systems, the Tx and Rx apertures are co-located [9,10]; yet one aperture is used for Tx and another for Rx. The monostatic systems use the same antenna for

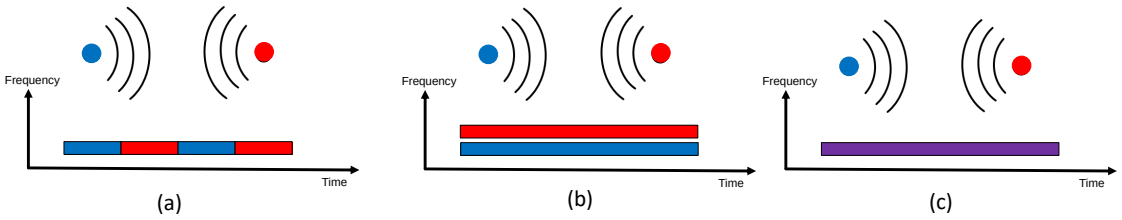

Figure 1.1: Conceptual depiction of (a) time domain duplexing (b) frequency domain duplexing and (c) simultaneous transmit and receive (STAR).

Tx and Rx, leading to greater space savings when compared to their bistatic counterparts. Monostatic STAR systems are the focus of this thesis and are discussed in more depth in the coming section. Hybrid STAR systems allow achieving an extremely wideband STAR antenna subsystem, where stand alone monostatic, bistatic, or quasi-monostatic are typically insufficient. Two or more of the other subsystems are combined into a single, multi-port antenna topology. The individual subystems must be designed to take advantage of synergistic SIC effects while avoiding antagonistic interactions between the different parts. A hybrid IBFD antenna configuration with four different subsystems, each operating over a distinct band, is designed to work from 0.5GHz to 45GHz in [11, 12] and a hybrid IBFD antenna comprised of a monocone and two circular arrays is shown in [13].

1.2 Monostatic STAR

As mentioned, monostatic STAR antenna subsystems share the aperture for both Tx and Rx. This makes them attractive for space-constrained platforms. The conventional approach to achieve monostatic IBFD is to use a single circulator as shown in Fig. 1.2. A caveat to this configuration is the circulator's port-to-port leakage which provides a direct path between the Tx and Rx. The SI is further compounded by antenna reflections and environmental reflection path, as outlined in Fig. 1.2, which are all routed towards the Rx port. Instead, by taking advantage of geometrical and electrical symmetries of the antenna and signal routing within BFNs, it is possible to obtain infinite isolation, in theory.

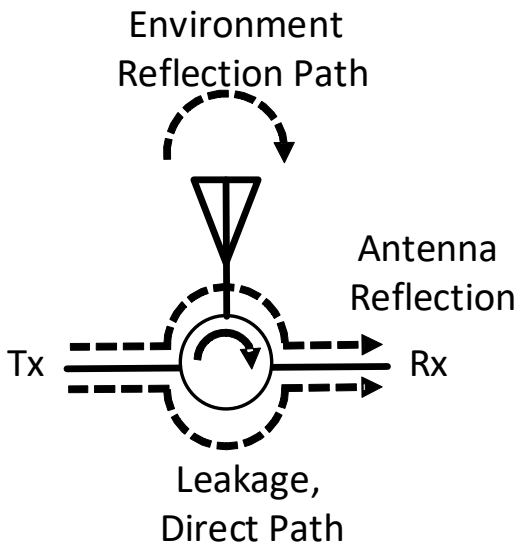

Figure 1.2: Conventional approach to achieve STAR using a single circulator.

1.2.1 Polarization Diversity

Polarization multiplexing can take advantage of the orthogonality between polarizations to achieve theoretically infinite SIC over the bandwidth. Generally, any well-designed dual-polarized antenna may serve this purpose. For example, very high isolation is demonstrated in patches [14,15] or in waveguide-fed antennas that utilize ortho-mode transducers (OMT) [2,3,9,16]. The achievable level of SIC is typically subject to fabrication imperfections. The use of polarization multiplexing, while space saving, is suboptimal. The advantages of using circular polarization (CP) to mitigate environmental reflection path [17] is wasted if the Rx antenna is oppositely polarized from its Tx counterpart.

1.2.2 Antiphase Spirals

Antiphase spirals are another type of STAR antenna. In [18], a four-arm spiral is reconfigured into a monostatic STAR configuration by pairing the two sets of opposite arms into respective Tx and Rx channel. The symmetry of the spiral and the 180° phase difference between both arms makes

the signals cancel at the ports to the spiral arms, resulting in theoretically infinite SIC between the Tx and Rx channels. The same principle is demonstrated with an 8-arm spiral where multiple modes and different operational scenarios are also shown to be possible [19]. The drawback with the antiphase spirals is reduced efficiency and radiation from the parasitic arms that distorts the antenna polarization quality. Helical terminations are used in [18] to reduce the currents that are reflected back whereas lens loading [19] can be used to improve both the axial ratio and efficiency of the antenna. These antennas can also be used in arrays [20], [21], however, certain tradeoffs in terms of scan/bandwidth/isolation/efficiency need to be considered. The cancellation mechanism discussed above is not restricted to spirals only. In [22], an 8-element planar inverted F antenna (PIFA) is seen to achieve monostatic operation using two 4-element circular arrays that are embedded within each other, reminiscent of the 8-arm spiral in [19]. The cancellation mechanism in antiphase spirals is independent of frequency and the imperfect SIC can be attributed to the configuration asymmetries. Printed circuit board (PCB) manufacturing produces high accuracy layouts and the tolerance errors are considered negligible in most cases. A more significant challenge is to remedy the imbalance of the baluns and (if required) hybrids.

1.2.3 Sequentially Rotated Array Antennas

A sequentially rotated array comprised of 2x2 linearly-polarized (LP) elements when excited with the same magnitude and a $\{0, \pm 90^\circ, 180^\circ, \pm 270^\circ\}$ phase progression will generate CP radiation [23–26]. By connecting each antenna port to a different BFN, it is possible to obtain an antenna that can take the place of the circulator in Fig. 1.2. In [23] delay lines are used whereas two Butler matrices are deployed in [24], both achieving true dual-polarized STAR operation. The compromise with this configuration is the reduced aperture efficiency which for practical topologies is theoretically limited to 50% [25]. This can be overcome by using CP radiating components.

1.2.4 Circular Arrays

Circular arrays with linearly polarized elements can be configured to achieve omni-directional (i.e. dipole-like) STAR operation without polarization multiplexing. To do so, they are excited with the modal phase progression through a Butler matrix-like feed where modal orthogonality and symmetries are utilized to achieve high level of isolation over wide bandwidth [27–31]

1.2.5 Balanced Circulator Beam Forming Network

Especially relevant for the research in this thesis is the balanced circulator beam forming network (BC-BFN). The BC-BFN consists of two hybrids and two circulators feeding a dual-polarized antenna. The coupling due to antenna reflections can be obtained by tracing the signal paths in Fig. 1.3 and expressed as (1.1) where $|B|$ is the magnitude of the circulator's leakage and Γ is the reflection coefficient at the antenna [17].

$$S_{\mathrm{TxRx}} = PathA + PathB = \frac{1}{2}\Gamma\left(1-|B|^2\right) - \frac{1}{2}\Gamma\left(1-|B|^2\right) = 0 \tag{1.1}$$

The reflections, and similarly the circulator leakage, add destructively at the Rx port and constructively at the loaded port. A more detailed breakdown of the signal paths is provided in Chapter 2. The antenna used for this system must support two orthogonal linear polarizations that will be excited with a 90° phase difference. The reflection coefficients of the antenna ports should ideally be identical and the ports should be isolated from each other. If the antenna ports are not isolated from each other, the port-to-port coupling shows up as a signal at the Rx port [32] and in Chapter 2 (1.1) will be expanded to describe non-isolated antennas. A system with dual polarized circular patches [17] and a dual-pol reflector antenna [33] are two among many possible implementations. In [34], a different variation of the balanced feed network is proposed where the 90° hybrids are replaced with modified Butler matrices. This enables excitation of different spiral modes for the 4-arm spiral. Corresponding ports on the Rx side serve to receive the incoming signal from the same mode. The balanced feed network provides theoretically infinite isolation as before while the Butler matrix provides mode-to-mode isolation, allowing for simultaneous use of each spiral mode

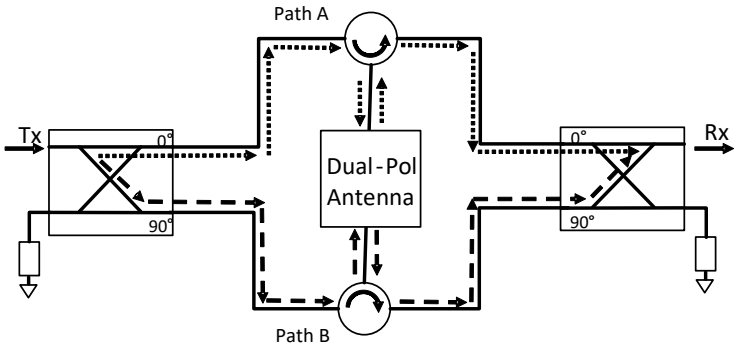

Figure 1.3: Balanced circulator beam former identifying the two main signal paths.

as a different IBFD channel. The patterns are spatially diverse between the different modes as the spiral mode 1 transmits at broadside while modes 2 and 3 have conical spatial distributions.

1.2.6 Table of Monostatic Systems

Table 1.2.6 summarizes the monostatic systems cited in the discussion so far. The measured SIC is included along with a brief description of the method and style of antenna for a side by side comparison between systems.

1.3 Lens Antennas

Growing interest in millimeter wave applications necessitates the need for researching antenna concepts with in-band full-duplex capability that can be readily realized with applicable technologies for these frequencies. In this thesis, a monostatic highly directive STAR antenna subsystem for operation within the Ka-band is proposed. Unlike [33], which uses reflectors to achieve high directivity, this thesis discusses an inhomogeneous lens-based approach. The advantage of a lens over a reflector is that the feed and associated guides feeding the antenna do not occlude the reflected signal. Spherical lenses also provide the potential of theoretically identical beams when scanning. This comes at a cost in efficiency due to losses in the dielectric.

While spherical electrically large lenses may be impractically size-wise at lower frequencies,

Reference	Method	Measured SIC	Frequency Band	Antenna Type
[14]	Polarization Diversity	43 dB	2.45 GHz	Dual LP Patch
[15]	Polarization Diversity	>65 dB	4.4 to 6 GHz	2x2 Dual LP Patch Array
[2]	Polarization Diversity	>35 dB	7.2 to 8.2 GHz	OMT Fed Circular Horn Antenna
[16]	Polarization Diversity	>35 dB	18 to 45 GHz	OMT Fed Quad Ridge Horn
[9]	Polarization Diversity	>30 dB	6 to 19 GHz	OMT Fed Quad Ridge Horn
[18]	Antiphase Spiral	>37 dB	0.5 to 2.5 GHz	4-Arm Archimedean Spiral
[21]	Antiphase Spiral	>40 dB (boresight) >30 dB (scanned to 30°)	2 to 5 GHz	3x3 4-Arm Archimedean Spiral Array
[19]	Antiphase Spiral	>38 dB	0.5 to 2.5 GHz	8-Arm Archimedean Spiral
[35]	Antiphase Spiral	>27 dB	0.65 to 2.75 GHz	4-Arm Spirals in Hexagonal Array
[22]	Antiphase Circular Array	>32	2.45 GHz	Circular PIFA arrays
[23]	Sequentially Rotated Array	54 dB	5.53 GHz	2x2 Dual polarized Patch Array
[24]	Sequentially Rotated Array	>47 dB	2.4 to 2.5 GHz	2x2 Dual Polarized Patch Array
[26]	Sequentially Rotated Array	>38 dB	1.25 to 2.5 GHz	2x2 Archimedean Spiral Array
[27]	Circular Array with Center Element	>55 dB	2.4 to 2.5 GHz	Circular Monopole Array
[28]	Circular Array with Center Element	>53 dB	2.42 to 2.48 GHz	Circular Monopole Array
[29]	Circular Array with Center Element	>40 dB	0.6 to 1.75 GHz	Circular Bent Loop Array
[30]	Orthogonal Mode Circular Array	>40 dB (M1/M0+M2) >28 dB (M0/M1)	0.8 to 1.7 GHz	Circular Monocone Array
[31]	Orthogonal Mode Circular Array	>30 dB (M0/M1) >43 dB (M1/Mixed Mode)	1.75 to 1.85 GHz	Circular Monopole Array
[17]	Balanced Feed	>40 dB	902 to 928 MHz	Circular Patch
[34]	Balanced Feed	>27 dB (Mode 1) >24 dB (Mode 3)	2 to 8 GHz	4-Arm Archimedean Spiral
[33]	Balanced Feed	>30 dB	4 to 8 GHz	Coaxial Cavity Fed Reflector

Table 1.1: Comparison of different Monostatic STAR systems in the literature

like the 1.7 meter lenses used for cellular LTE communications in [36], at higher frequencies the resulting system can be reasonably compact. For example, a 5 cm lens is designed for automotive radar in [37] operating at 77 GHz. This opens up the possibility for these lenses to appear in more diverse electronic warfare and commercial applications. For inhomogeneous spherical graded index of refraction (GRIN) lenses the resulting permittivity profile is typically implemented as multiple discrete layers with uniform permittivity [38–40]. Obtaining or manufacturing materials for the different permitivites can be complicated. Metamaterials [41, 42] have been employed and, more recently, 3D printing effective permittivities [43] have been used to achieve the permittivity profile.

If a planar profile is desired then planar cylindrical GRIN lenses are a viable choice. There are multiple ways to manufacture these lenses, including composite materials [44], machined substrates [45, 46], and 3D printing cylindrical GRIN structures using partially air-filled dielectrics in millimeter wave applications [47–51]. As seen, the 3D printing leads to practical manufacturing of lightweight lenses that provide high directivity while maintaining scanning operation. Some flat GRIN lenses from the literature are shown in Fig. 4.1. References [44,45,51] present beam scanning by switching between different antennas positioned off the optical axis. While fast, this technique incurs a significant amount of scan loss since antennas are displaced from the focal point and the rays are not properly collimated.

1.4 Retrodirective Systems

Retrodirective (RD) systems that provide enhanced radar cross section (RCS) have long been of interest for airborne, satellite and naval communications as well as wide-angle and wide-bandwidth radar targets. Commercial applications such as RF identification of vehicles and items have been emerging in more recent times as well. RD arrays (RDA) use an array to enhance the RCS in the direction of the received signal. In Van-Atta RDA (VA-RDA) [52–58], retrodirectivity is achieved by interconnecting the array elements. Passive VA-RDAs can be implemented with transmission lines of equal length to provide equal phase delay between pairs of elements that mirror each other with respect to the center of the array. This phase delay self-steers the

beam towards the direction of the incident wave. Heterodyne phase conjugators would also allow achieving retrodirectivity [59] [56]. Recent work has demonstrated that STAR can improve the performance of VA-RDA with quasi-monostatic spiral elements [10] that reduce the feedback, allowing for potentially greater RCS enhancement.

Using completely passive components, Luneburg lens reflectors [60–62] provide simple ways to achieve wide-angle and wide-bandwidth retrodirectivity. By placing reflective material on this focal surface it is possible to create a passive reflector. An active RD system using a 2D Luneburg lens was developed in [63] and reported 10dB measured improvement. The feedback in the system creates a limit in how much amplification can be expected and in this work the BC-BFN is examined to demonstrate a proof of concept for a co-polarized circularly polarized retrodirective system that can greatly surpass the amplification of passive reflectors.

1.5 Thesis Objectives

This thesis presents various ways that lens based STAR systems can achieve highly directive beam steerable full-duplex operation. To enable the demonstration of these systems a waveguide implementation of the BC-BFN is developed and an ultra-low imbalance symmetric OMT is designed to complement this STAR BFN. A high directivity monostatic STAR subsystem is demonstrated using a spherical lens antenna along with investigations into the sensitivity of the BC-BFN to lens positioning errors.

Beam steerable STAR using mechanical techniques is demonstrated using the half-lens in Chapter 3 and the planar lens in Chapter 4. Though not as fast as electronic scanning means cited from literature, these techniques show sustained in-band full duplex performance as the beam is scanned and present viable candidates for systems that do not require the speed. The techniques presented do not depend on complicated electro-mechanical joints. Instead, the waveguide components are all static and motion of the lenses, which are not in direct contact with the feeds, is used to move the beam. The novel mechanical scanning of the planar lens in Chapter 4 presents advantages, when compared to its beam-switched counterpart, in the form of reduced scan loss in

a larger field of view. Most importantly, this research shows that the impact of near-field imperfections (symmetry, structure, inhomogeneous materials, etc), while observable, is not detrimental for the role of these antenna systems in STAR.

STAR's capability to improve retrodirective systems is also introduced. A closed form expression for the RCS due to the BFN applicable to arrays or lens manifolds is developed and algebraic solutions for the maximum loop gain in various retrodirective systems are presented to show the limits of amplification that these systems could provide. This mathematical framework is combined with measured data from the STAR subsystem discussed in Chapter 3 to demonstrate how STAR subsystems could augment lens based retrodirective systems to surpass in performance passive lens reflector systems.

1.6 Methodology

To accomplish the thesis objectives the following methodology is employed. The theory regarding the different lenses is studied until understood and a suitable feed antenna is designed, considering impedance and gain bandwidth. Full wave simulations in the appropiate solvers are used to verify guiding theoretical principles. The numerical methods for these are: finite element method using Ansys HFSS [64], method of moment in Altair's FEKO [65], and finite integral time domain in Dasault Systemes' CST [66]. Data from both simulation and measurement is analyzed using Python 2.7 [67] using the scipy stack [68] and scikit-rf [69] which enables manipulating touchstone files. All designs are then fabricated and tested. The components for the BC-BFN in Chapter 2 are mostly purchased from different vendors. The hybrids and the OMT are first designed here and then fabricated using split-block computer numericallly controlled (CNC) machining from third party vendors. The spherical lens in Chapter 3 is purchased from Lun-Tech [70] and the half lens was fabricated in-house. The lens in Chapter 4 is 3D printed using a Formlab's Form 2 printer using Tough RS-F2-TOTL-05 resin. S-parameters for the systems are measured with an Agilent 8719ES Vector Network Analyzer, and antenna patterns are characterized using an NSI 700S-30 combined spherical near-field and far-field chamber at the University of Colorado Boulder.

1.7 Thesis Organization

The thesis is organized in Chapters as follows:

- Chapter 2 examines the coupling paths within a BC-BFN along with how different assumptions are made about the antenna and components to arrive at the forms seen in the literature. A term representing the coupling between imperfectly isolated ports in an antenna is added. With this augmentation, the resulting equation is suitable to describe the Tx/Rx coupling in a BC-BFN with a reciprocal dual-polarized antenna that is not necessarily symmetric or has good port-to-port isolation.

  To comply with the BC-BFN's symmetry requirements, a highly symmetric WR28 waveguide OMT is developed. This OMT not only maintains balance in the transmission coefficients between both polarizations but also in the reflection coefficients at each port. In full wave simulations the new design is shown to provide isolation near the numerical noise levels and the fabricated BC-BFN and OMT have a measured isolation better than 30 dB, significantly surpassing the single circulator configurations constructed with the same components.

- Chapter 3 examines the design of a spherically stratified lens antenna for STAR. The sensitivity of the BC-BFN to lens displacement is numerically studied and the system is found to be resilient to this imperfection. Measurements are taken of the BC-BFN configuration with and without the lens. For comparison, 2 configurations using the single circulator are assembled using the same COTS components and tested with and without the lens. The BC-BFN is shown to provide significant improvement in Tx/Rx isolation.

  The design of a rotating half lens is discussed in the later sections as a way to include beam scanning. The system is experimentally shown to maintain high Tx/Rx isolation while generating consistent circularly polarized beams in a 360° equatorial FOV.

- Chapter 4 a flat GRIN lens is proposed as a viable alternative to achieve high-directivity

beam-steerable monostatic-STAR system. The lens is designed so it can be 3D printed. Air-filled spaces are left in the material to effectively lower the resulting permittivity and achieve the necessary profile. The beams are steered by mechanically rotating the proposed compact lens in an 80° conic field of view while preserving system isolation. Full wave analysis and measurements are used to demonstrate the performance of the proposed system.

- In Chapter 5, closed-form expressions are derived for the component of the RCS due to the BFN. The derived expression is studied in the context of the retrodirective systems. The ability to accurately predict the effect of feedback and infinite reflections is shown with numerical simulations. The derived equations are shown to allow calculating what the maximum loop gain for the system before feedback would take its response into the non-linear domain. The potential of using STAR to improve the performance of retrodirective systems is evaluated with a spherical lens antenna. Improvements are shown when data from the system discussed in Chapter 3 is compared to passive lens reflectors.

- Chapter 6 provides a summary of the work and the contributions to the scientific community. Possible directions for future research are also outlined.

Chapter 2

OMTs for Balanced Circulator Beamforming Networks (BC-BFN)

When separating the Tx and Rx ports in a STAR antenna subsystem it makes intuitive sense to use a circulator as their ideal behaviour readily translates into 3 ports; Tx port, antenna port, and Rx port. Antennas, however well designed, often have mismatch reflections in the range of -10 to -15 dB. In a STAR system using the single circulator shown in Fig. 1.2, any signal from the Tx port would be routed to the antenna and any signal coming from the antenna would be routed to the Rx port. At the antenna, the Tx signal is reflected with the Γ_a reflection coefficient and fed back into the Rx port. From the discussion above it is readily found that $S_{\mathrm{Rx,Tx}} = \Gamma_a$. It should be noted that this assumes a perfectly isolating circulator. If the coupling between the circulator's isolated ports (i.e. ports in the direction opposite the arrow in Fig. 1.2) is added as B then the expression for the max usable loop gain becomes:

$$S_{\mathrm{Rx,Tx}} = \Gamma_a + B \tag{2.1}$$

where both, Γ_a and B are complex numbers. Having these two values cancel out is not the focus within this writing but recent work such as [71] has devised ways to tune the antenna reflections and circulator leakage to achieve a high level of self interference cancellation (SIC) in a narrow band. This method would require designing the system such that B and Γ_a have comparable amplitudes and are phased to interfere destructively. While it is possible to do so in a narrow band, a wider bandwidth system will see these two interact in and out of phase at different frequencies, therefore making this problem much more difficult.

The balanced circulator beam forming network (BC-BFN) is designed to completely remove both the antenna reflections and the circulator leakage. The following sections detail how this is achieved for the main coupling paths.

This chapter is organized as follows:

- Section 2.1 breaks down the different coupling paths within the BC-BFN and combines them into one concise expression.
- Section 2.2 shows the design of the highly symmetric orthomode transducer (OMT) which complements the BC-BFN
- Section 2.3 covers the details behind the fabrication and testing of the BC-BFN and OMT.
- Section 2.4 provides a summary and conclusions on the results obtained in this chapter.

2.1 Coupling Expressions for the BC-BFN

There are 3 coupling paths of interest in this work. Diagrams representing these paths can be seen in Fig. 2.1. Specifically:

- Path shown in Fig. 2.1(a) is the coupling path due to the antenna reflections (ARP).
- Path shown in Fig. 2.1(b) is the circulator leakage path (CLP).
- Path shown in Fig. 2.1(c) is the leakage due to the coupling through the antenna ports (ACP).

The total coupling is the sum of these three components arising through all paths.

$$S_{\mathrm{Rx,Tx}} = S_{\mathrm{ARP}} + S_{\mathrm{CLP}} + S_{\mathrm{ACP}} \tag{2.2}$$

In an ideal system all three components are independently zero resulting in zero coupling between the Rx and Tx ports. The conditions for this are discussed below for each. Fig. 2.2 labels the ports and should be referenced when discussing the different coupling paths.

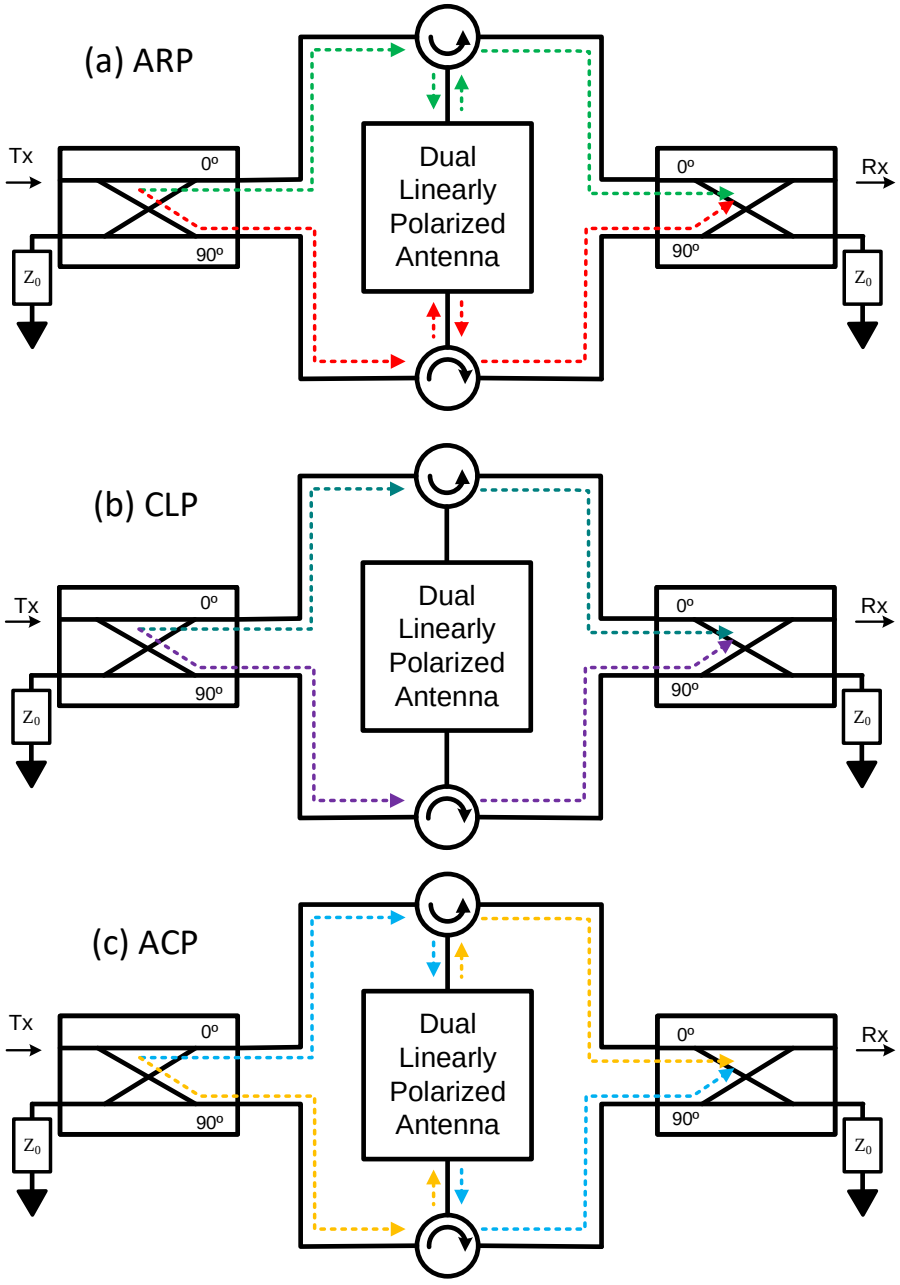

Figure 2.1: Coupling paths from the Tx to the Rx port in a BC-BFN STAR system. (a) Path due to antenna reflections (ARP). (b) Path due to circulator leakage (CLP). (c) Path due to the antenna coupling (ACP)

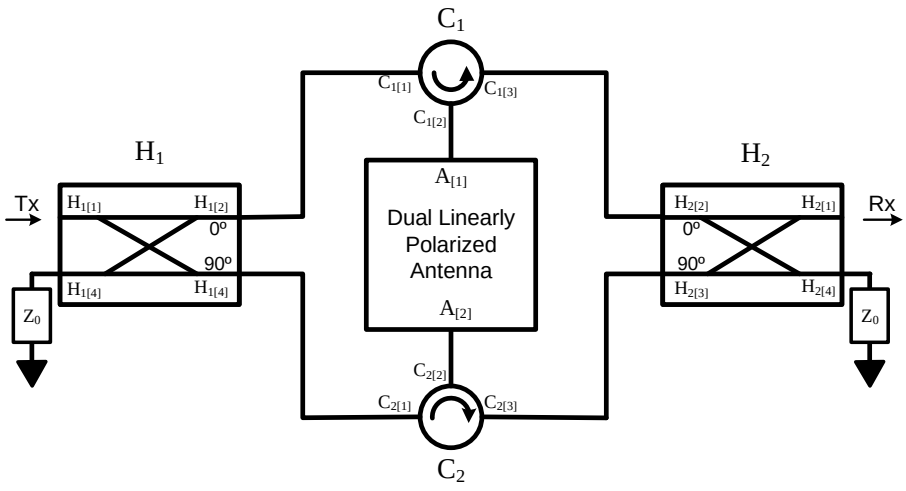

Figure 2.2: Port and device labels used when examining the coupling paths

2.1.1 Antenna Reflection Path

By tracing the signal through the green (upper) and red (lower) paths in Fig. 2.1(a) an expression for the S_{ARP} is denoted in (2.3).

$$S_{\text{ARP}} = H_{1[21]}C_{1[21]}\Gamma_1 C_{1[32]}H_{2[12]} + H_{1[31]}C_{2[21]}\Gamma_2 C_{2[32]}H_{2[13]} \tag{2.3}$$

The above expression uses the labeling of the ports as identified in Fig. 2.2. H_1 and H_2 are the scattering matrices for the hybrid on the left and right side of the diagram. C_1 and C_2 are the matrices for the upper and lower circulator respectively. The bracketed subscripts indicate which ports the component being used corresponds to. Γ_1 and Γ_2 are the antenna reflection coeffients at the indicated port. In order to simplify the above expression some supositions regarding the components in the BC-BFN are used. First, both circulators and both hybrids are assumed to be identical, meaning (2.4) for all valid ports p,q.

$$C_{1[pq]} = C_{2[pq]} \text{ and } H_{1[pq]} = H_{2[pq]} \tag{2.4}$$

Quadrature hybrids are reciprocal components so they satisfy $H_{1[pq]} = H_{1[qp]}$ but for the BC-BFN they must also be balanced, meaning that the signal is divided evenly between ports 2 and 3 with

exactly 90° between them. This leads to the equation below.

$$H_{1[31]} = jH_{1[21]} \tag{2.5}$$

Making all the substitutions one is left with

$$S_{\text{ARP}} = H_{1[21]}C_{1[21]}C_{1[32]}\Gamma_1 H_{2[12]} + jH_{1[21]}C_{1[21]}C_{1[32]}\Gamma_2 jH_{2[12]} \tag{2.6}$$

which factors further to

$$S_{\text{ARP}} = H_{1[21]}^2 C_{1[21]}C_{1[32]}(\Gamma_1 - \Gamma_2) \tag{2.7}$$

This result is reminiscent of the result in [17]. Therein the added phase contribution in the hybrids and circulators are reasonably discarded as their interests was the magnitude of (2.7). The hybrids are assumed to be lossless, meaning

$$H_{1[21]} = \frac{1}{\sqrt{2}} \tag{2.8}$$

and the amplitude of the circulator's transmissions is described in terms of the leakage B while assuming the circulator is symmetrical from all three ports, meaning

$$|C_{1[21]}| = |C_{1[32]}| = |C_{1[13]}| = \sqrt{1 - |B|^2} \tag{2.9}$$

and both of these assumptions then turn (2.7) into

$$S_{\text{ARP}} = \frac{1}{2}\left(1 - |B|^2\right)(\Gamma_1 - \Gamma_2) \tag{2.10}$$

which is the same result as [17]. Expression (2.7) shows that the only reasonable way for $S_{\text{ARP}} = 0$ is enforcing $\Gamma_1 = \Gamma_2$.

2.1.2 Circulator Leakage Path

In a similar fashion to the preceding discussion, the CLP depicted in Fig. 2.1(b) is expressed by

$$S_{\text{CLP}} = H_{1[21]}C_{1[31]}H_{2[12]} + H_{1[31]}C_{2[31]}H_{2[13]} \tag{2.11}$$

which can be summarily reduced to zero with the condition that the circulators are equal, (2.4), along with the reciprocity and balance of the hybrids, (2.5). Certainly ideal circulators with zero leakage between their isolated ports (1 and 3 in the above) would also results in a $S_{\text{CLP}} = 0$.

2.1.3 Antenna Coupling Path

The final path to be discussed herein is the path through the antenna. This signal results from the coupling between the antenna ports, $A_{[1]}$ and $A_{[2]}$. This coupling will be expressed as S_{21} and since the antenna is assumed reciprocal, $S_{21} = S_{12}$. The resulting equation from tracing the path in Fig. 2.1(c) is

$$S_{\text{ACP}} = H_{1[21]}C_{1[21]}S_{21}C_{1[32]}\Gamma_1 H_{2[12]} + jH_{1[21]}C_{1[21]}S_{12}C_{1[32]}\Gamma_2 jH_{2[12]}. \tag{2.12}$$

Applying the conditions from (2.4), (2.5), and the reciprocity of the hybrids reduces the expression to

$$S_{\text{ACP}} = 2jH_{1[21]}^2 C_{1[21]}C_{1[32]}S_{21}. \tag{2.13}$$

This expression clearly shows that the coupling through the antenna does not cancel out and that the leakage between the antenna ports should not be ignored. However, most dual polarized antennas can be designed with very low coupling, S_{21}.

2.1.4 All Paths Combined

Replacing the results from the previous 3 subsections into (2.2) allows writing a final expression

$$S_{\text{Rx,Tx}} = H_{1[21]}^2 C_{1[21]}C_{1[32]}\left(\Gamma_1 - \Gamma_2 + 2jS_{21}\right). \tag{2.14}$$

The assumptions (2.8) and (2.9) can be applied to this equation as well to re-write it as

$$S_{\text{Rx,Tx}} = \frac{1}{2}\left(1 - |B|^2\right)\left(\Gamma_1 - \Gamma_2 + 2jS_{21}\right). \tag{2.15}$$

This expression summarizes how an arbitrary reciprocal dual polarized antenna's network parameters affect the expected isolation of BC-BFN based STAR systems.

2.2 Ortho Mode Transducers

OMTs are 6-port devices that enable dual-polarized polarized performance of horn antennas. To maximize the isolation of a BC-BFN, it is critical that the antenna ports are highly isolated (S_{21}

in (2.15)) and that the reflection coefficients (Γ_1, Γ_2) are symmetrical [17, 32, 72]. Thus the design and fabrication of OMT is critical, therefore requiring special attention. OMTs can be broadly grouped in three classes [3].

- Class 1 OMTs consist of main and side arms, often orthogonal to each other [2, 73, 74], creating large physical asymmetries that generally lead to different network parameters along each path.
- Class 2 OMTs use side arms and a septum to separate polarizations [3, 75]. This kind of junction is often called the Boiføt junction. Though the structure is symmetric, the path that each polarization travels is different. This leads to asymmetries in between both ports.
- Class 3 OMTs use Turnstile junctions and allow for realization of symmetric polarization paths [4, 9, 11, 16, 75, 76] and will be the focus of the discussion moving forward.

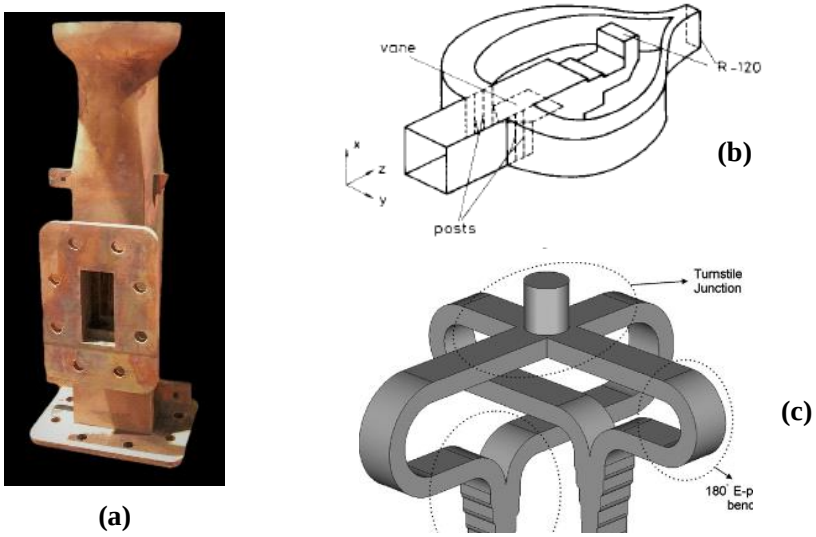

Figure 2.3: Examples of different OMT types. (a) Type 1, showing orthogonal arms. [2] (b) Type 2, often called Boiføt junction OMTs, [3]. (c) Type 3, turnstile junction based OMT [4]

.

The use of a class 3 junction guarantees symmetry between the two polarizations at the

junction but as it will be shortly discussed, the overall structure of the OMT must still be taken into consideration.

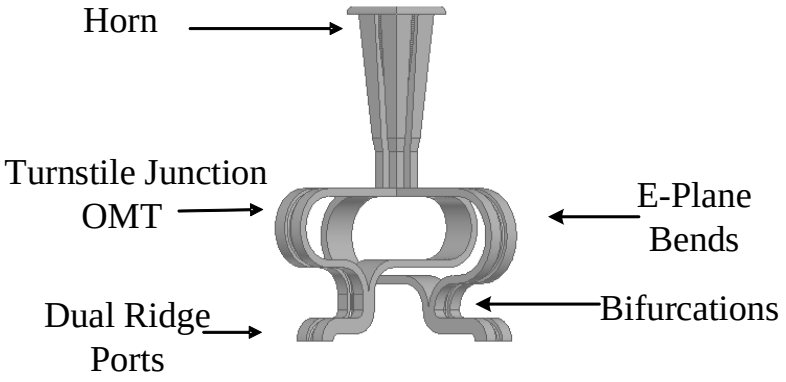

Figure 2.4: Dual ridge waveguide based class 3 OMT used for preliminary testing

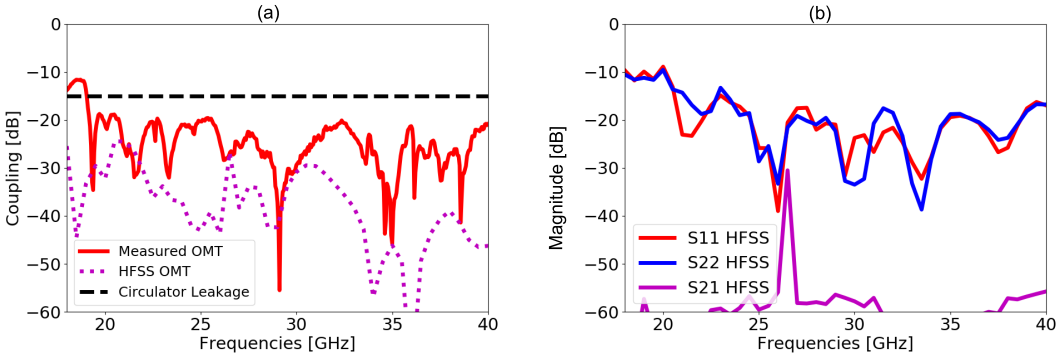

Figure 2.5: (a) Expected TxRx coupling using an ideal BFN network (balanced matched hybrids; identical matched circulators with -15d dB leakage, as indicated in the figure) (b) HFSS simulated S-paramters for the OMT shown in Fig. 2.4

Fig. 2.3(c) shows a good example of a common way to route the waveguides, focusing on using the space bellow the junction to place the bifurcations and the ports. In order to test how well this kind of OMT would perform with a BC-BFN a class 3 OMT [12] was used. An image of the HFSS model is presented in Fig. 2.4. The performance with an ideal BC-BFN using measured

and simulated data can be seen in Fig. 2.5(a). The ideal BC-BFN in this case is a BFN composed of balanced 90° hybrids and identical circulators with a -15 dB leakage between isolated ports. -15 dB is chosen as it is a nominal value that is readily available in commercial products. All components in the BC-BFN are assumed to be lossless and matched to the system impedance Z_0. The about 20 dB of isolation in this initial system is not satisfactory when compared to the systems in the literature (see Table 1.2.6). The simulated data is included for comparison and to asses the possible impact of fabrication errors. While an improvement of 10 dB or better is seen at many frequencies, even with simulated data the system is not yielding perfect isolation. After inspecting the S-parameters for the simulated OMT, it can be seen that coupling between the polarizations is very low, as expected of a numerical simulation, and does not account for the elevated coupling. The difference then, is adjudicated to asymmetries in routing of the waveguides. The differing E-plane bends and bifurcation heights are clearly observed in Fig. 2.4. These cause small but sufficient discrepancies in the magnitude and phase of the reflection coefficients of both channels, preventing the cancellation of the coupling in the BC-BFN.

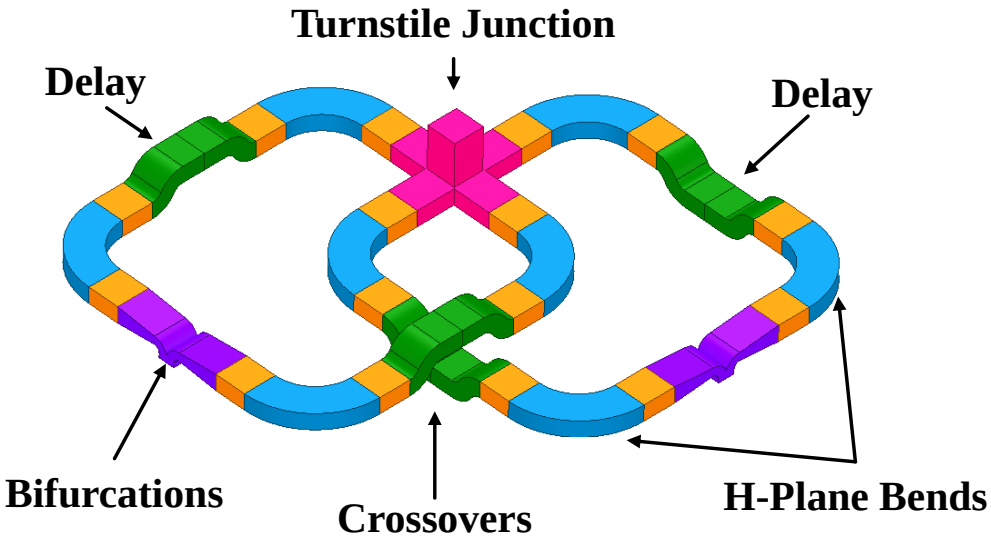

Figure 2.6: CAD model of the WR28 turnstile junction based OMT with its constitutive parts highlighted.

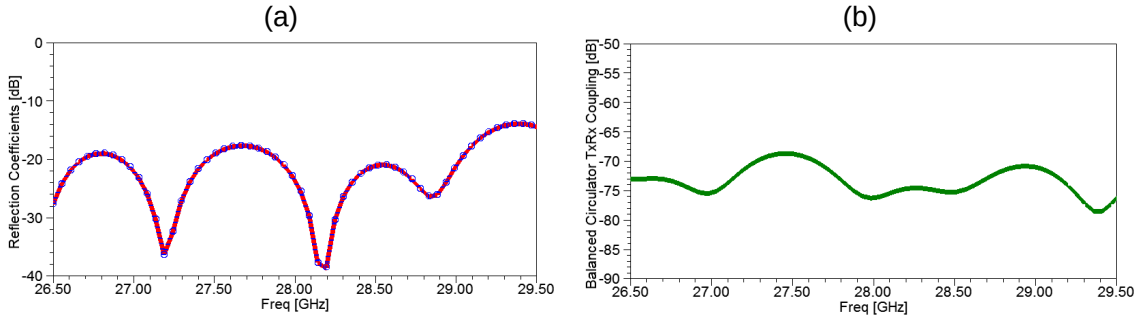

Figure 2.7: (a) Simulated reflection coefficients for the designed WR28 OMT shown in Fig. 2.6. (b) Simulated TxRx coupling with an ideal balanced BC-BFN (as before, $B = -15$ dB and all components identical).

To overcome asymmetries from the required interconnects used to join the two branches of each polarization, the turnstile junction based OMT shown in Fig. 2.6 is developed. The symmetry is achieved by carefully routing H-plane bends, crossovers, and delays; designing them such that the equalization of phased delays in all four paths is emphasized. The key to maintaining equality between Γ_1 and Γ_2 is ensuring a signal traveling on any path experiences the same number of changes located at the same distances from each other. This keeps the reflection coefficients highly similar in amplitude and phase which is crucial to keep the $\Gamma_1 - \Gamma_2$ term in (2.15) close to zero. Using E-plane bends such as the OMTs in [4, 9, 11, 16, 75] it is possible to obtain phased-matched transmission for both polarizations. However, the offsets in the height of the junctions and the radii of the bends introduce small asymmetries between the reflection coefficients, leading to a finite isolation when used with a BC-BFN [32, 72]. The turnstile junction is symmetric, thus a high isolation between the two channels is achieved, and the S_{21} term is kept small. To the author's knowledge the closest reference in the open literature is [77] where a highly symmetric OMT is realized using TEM coaxial lines. The TE line OMT developed here achieves nearly identical reflection coefficients shown in Fig. 2.7(a). The phase is omitted but it too is identical to within the numerical precision. When tested with an ideal BC-BFN (as defined in the previous section) an isolation better than 69 dB is obtained. This is a significant improvement over the previous result obtained in Fig. 2.5. The results where obtained with stringent mesh parameters within HFSS. A delta-s convergence bellow -40 dB(0.01) was used with at least 2 convergent passes. Curvilinear

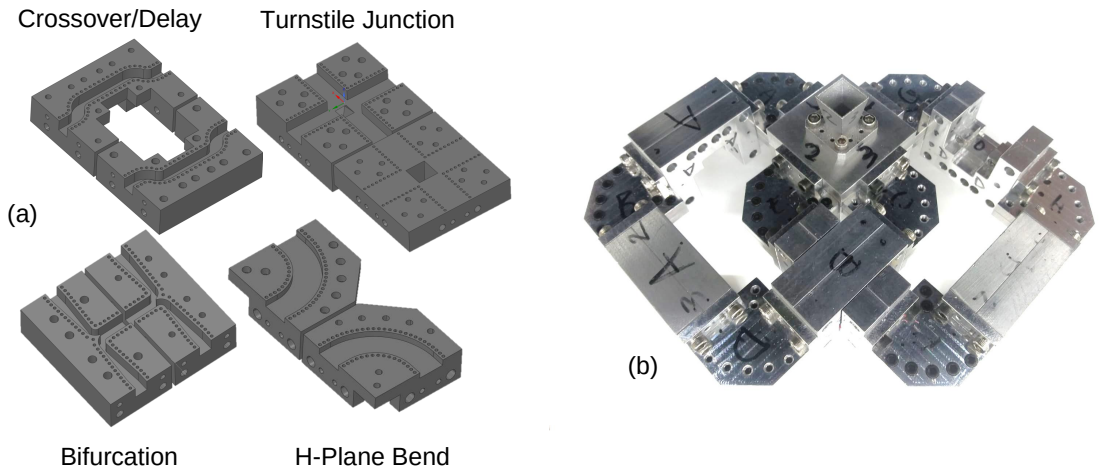

Figure 2.8: (a) CAD model of the 4 different components that make up the OMT. (b) Photo of the fabricated OMT. The photo includes to horn which will be discussed in the next section

elements as well as a surface deviation of 7.5 degrees was used to improve the accuracy of all the curved surfaces. The model was solved using second order basis functions.

2.3 Fabrication and Testing

The OMT is realized with a split-block approach where the potential leakage, particularly in the H-plane cuts, is suppressed by the use of a pin wall [78]. 3D models and a photograph of the fabricated OMT are shown in Fig. 2.8 whereas the measurements are given in Fig. 2.9(a). For the measurements the OMT is terminated with a square aperture horn that will be further discussed in the next chapter. For now, it suffices to indicate that this horn is matched to better than -20 dB in the band. Due to the fabrication imperfections, the reflection coefficients, though similar, are not identical and therefore limit the isolation through the Γ_1 and Γ_2 in (2.15). Other asymmetries in the OMT, for example in the junction, contribute to a non-zero $|S_{21}|$ between the two ports. The measurements show that this coupling between polarizations, sometimes the most important parameter for these microwave devices, lies below the -50 dB range for most of the band of interest between 27 and 29 GHz.

The BC-BFN is assembled from commercial off the shelf (COTS) circulators (JQL Technolo-

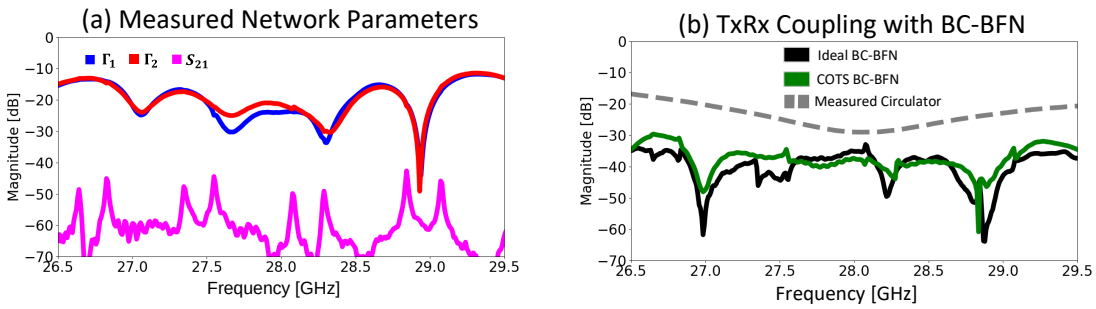

Figure 2.9: (a) Measured network parameters showing good port-to-port isolation in the OMT. (b) Resulting isolation using an ideal and COTS BC-BFN.

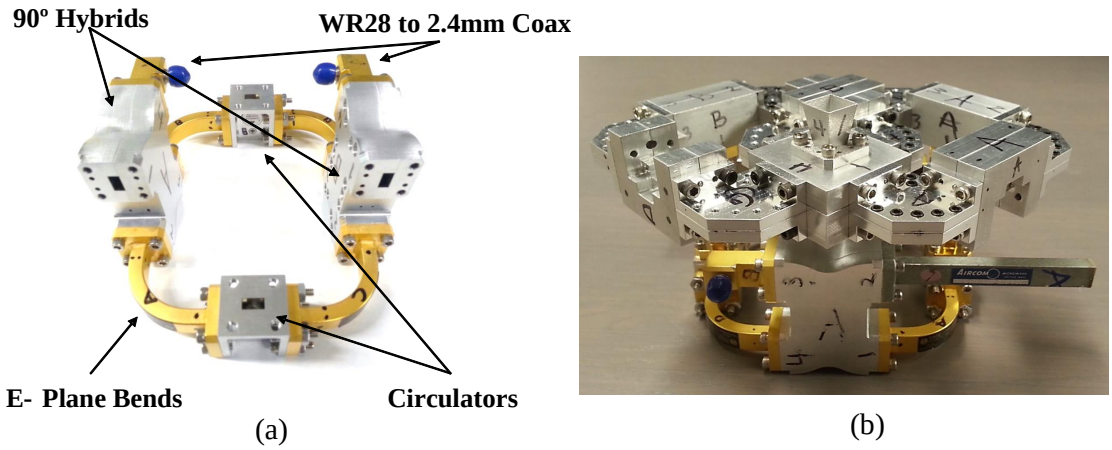

Figure 2.10: (a) WR28 BC-BFN and (b) fabricated OMT assembled with the BC-BFN.

gies JCWR28-21A-27K0T29K0), loads, adapters, and bends, as well as in-house CNC machined 90° hybrids. The circulators operate from 27 to 29 GHz with a nominal isolation of 21 dB (measured values shown in Fig. 2.9(b)). The 90° hybrids are designed to operate within the bandwidth of the COTS circulators and have maximum amplitude and phase imbalances of 0.25 dB and 5°, respectively. Four E-plane bends connect the components as shown in Fig. 2.10(a). Loads matched to better than -25 dB are used to terminate the hybrids.

Fig. 2.9(b) shows the resulting coupling using the simulated and fabricated BC-BFN. The performance remains consistent when the COTS BC-BFN is used thus, the comparison with the

ideal BC-BFN shows that the finite isolation is due to the fabrication imperfections in the OMT. Compared to the circulator, there is an improvement of 13 dB on average (min 7.6, max 32.8 dB). Fig. 2.10(b) shows how the OMT sits above the BC-BFN. Not visible are two 45° twists that connect the circulators and the OMT's bifurcations. The insertion loss of the BC-BFN and OMT from the input of the hybrids to the output of the OMT was measured to be around 1 dB for both the Tx and Rx channels.

2.4 Conclusion

The coupling paths in an ideal BC-BFN network have been presented and the term representing imperfect port-to-port isolation in the antenna has been introduced in the study. The derived expression will be used in the following chapters to evaluate how different lenses affect the TxRx coupling. In order to achieve a dual pol waveguide based system, the class 3 OMT is chosen to connect the antenna and the BC-BFN as its turnstile junction allows for maintaining symmetry between both polarizations while providing high isolation. The importance of the routing of the lines to the ports has been demonstrated to limit the isolation that can be expected of these systems. A design that routes the lines in such a way that not only the transmitted, but also the reflected signal maintains symmetry has been presented and shown to yield very high isolation in simulation. The system was built and tested to demonstrate that this OMT provides a better isolation when integrated with the BC-BFN. Average increase in isolation over the single circulator of 13 dB is obtained. More careful fabrication with tighter tolerances can further improve the system performance

Chapter 3

Spherically Stratified Lens Based System

Highly directional antennas are indispensable for many applications, especially at millimeter wave frequencies where high directivity is needed to compensate significant free space path loss. Spherically stratified lens antennas support high directivity and high quality beam steering. The Luneburg lens is a spherically symmetric graded index of refraction (GRIN) lens [79]. In general, this lens will focus an incoming plane wave from any given direction onto a focal point on the opposite side of the lens. The set of focal points creates a spherical focal surface in the shape of a sphere, concentric to the lens. The radius of the focal surface can be greater than, equal to, or less than the radius of the lens itself. By placing an antenna at this focal surface, the beam is collimated and a higher directivity is achieved. Due to the symmetry of the lens, moving the antenna or switching between copies along this focal surface results in consistent beams that, in theory, see no beam squinting, beam broadening, or scan loss. In practice, some interaction between the feeds, construction, and tolerances impact the consistency among the beams. The lens is single or dual-pol capable and inherently broadband.

The following sections explore the sensitivity of the performance of a STAR antenna subsystem utilizing the previously discussed BC-BFN to the presence of a spherical lens. The symmetry of the lens is then used to develop a STAR antenna which maintains a high TxRx isolation while beam steering.

This chapter is organized as follows:

- Section 3.1 covers the design of a spherical lens antenna. Sensitivity to the lens displacement

on STAR performance is studied. The fabricated system's isolation is compared across various circulator configurations and far-field data is presented for the antenna as well.

- Section 3.2 presents the design and testing of a rotating spherical half lens to enable beam-scanning while preserving STAR performance.
- Section 3.3 provides summary and conclusions on the results obtained in this chapter.

3.1 Dual-Pol Spherical Lens Antenna

3.1.1 Spherical Lens

Luneburg topology has a continuously varying index of refraction n which satisfies [79]

$$n = \exp\left[\frac{1}{\pi}\int_{nr}^{1}\frac{\arcsin\left(k/f\right)}{\sqrt{k^2-(nr)^2}}\,dk\right] \tag{3.1}$$

where r and f are the normalized radial position and normalized focal radius of the lens such that $r = R/R_{Lens}$ and $f = F/R_{Lens}$ using the dimensions identified in Fig. 3.1. This expression has algebraic solutions when the focal point is internal to the lens($f < 1$) or when the focal point is on the surface of the lens ($f = 1$) [79].

$$n = \frac{1}{f}\sqrt{1+f^2-r^2},\ f < 1 \tag{3.2}$$

$$n = \sqrt{2-r^2},\ f = 1 \tag{3.3}$$

A simple algebraic solution does not exist for the $f > 1$ case but [80] provides an iterative solution for (3.1). Plots for the permittivity for all three cases are shown in Fig. 3.2. The resulting permittivity profile is typically implemented as multiple discrete layers with uniform permittivity [38–40]. Obtaining or manufacturing materials for the different permitivites can be complicated. Metamaterials [41, 42] have been employed and, more recently, 3D printing effective permittivities [43] have been used to achieve the permittivity profile. Care must be taken with these techniques to maintain the bandwidth as well as consistent properties for both polarizations since the resulting

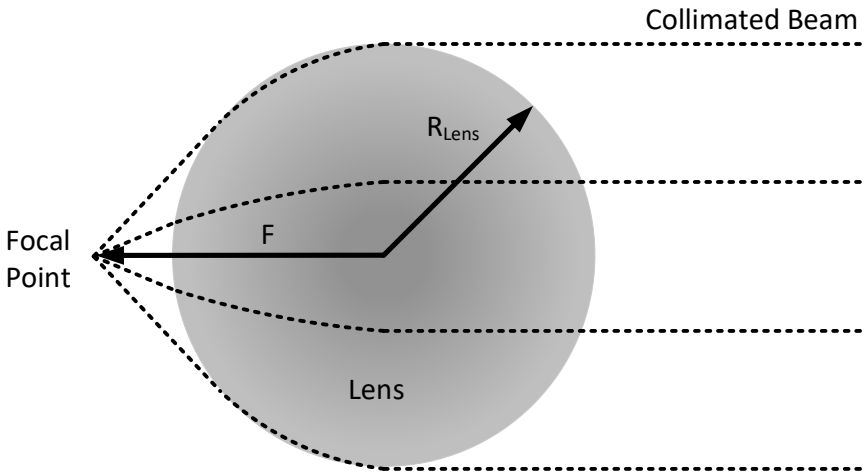

Figure 3.1: Diagram showing the basic concept behind the Luneburg lens. The rays from a source placed at the focal point a distance F from the center of the lens are collimated onto a plane wave.

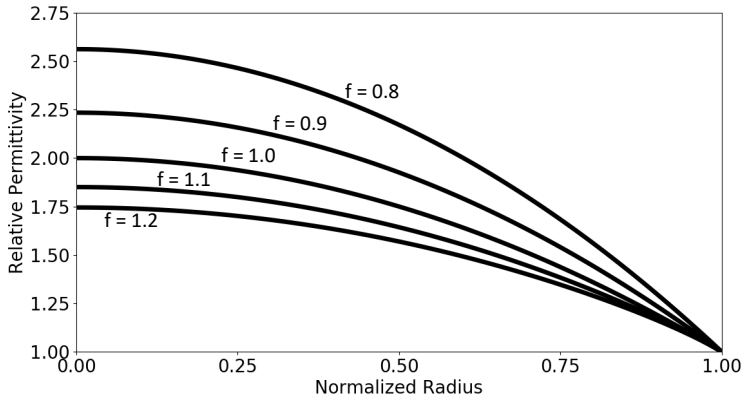

Figure 3.2: Relative permittivity as a function of normalized lens radius $r = R/R_{Lens}$ for 5 different focal lengths $f = F/R_{Lens}$. The relative permittivity, ϵ_r, is obtained from (3.1), (3.2), and (3.3) through the relationship $n^2 = \epsilon_r \mu_r$ with the assumption that the material is non-magnetic; i.e. $\mu_r = 1$

effective material is often anisotropic. 3D printing effective permittivity will be discussed further in the next chapter.

An alternative technique to obtain a spherical lens with performance similar to a Luneburg

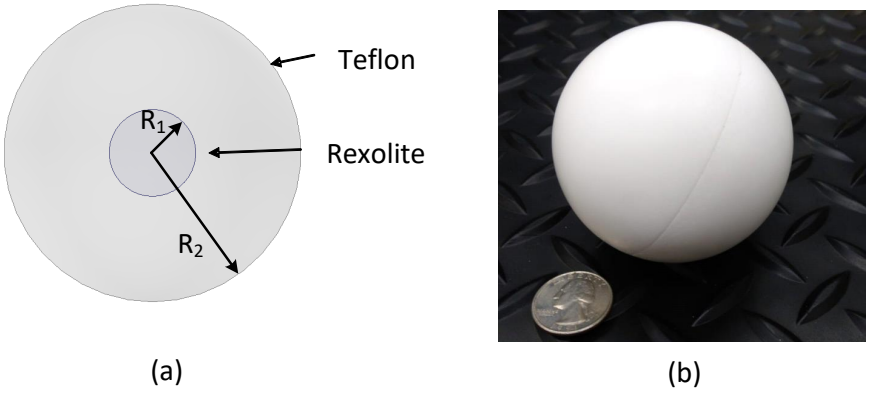

Figure 3.3: Two layer spherical lens. The radius of the inner rexolite sphere is R_1 =10.5 mm and the layer of the outer PTFE sphere is R_2 =36 mm.

lens is presented in [81]. By numerically tuning the ratio between two spheres of known material parameters it is possible to obtain lens with comparable behavior that is much easier to machine using conventional techniques like CNC. The lens used in this part of the thesis is a 72 mm diameter configuration built by Lun'Tech in Perols, France. It is pictured in Fig. 3.3 and is built from 2 layers; an outer PTFE(Teflon) shell, and an inner Rexolite core. The former has a relative permittivity of 2.1 , whereas the latter has relative permittivity of 2.53. The focal point for this lens has been determined to be 4.5 mm away from the lens' surface [82].

3.1.2 Lens Feed

The feed is a dual-polarized square aperture horn, shown in Fig. 3.4, designed to achieve directivity above 25 dBi from 27 to 29 GHz when integrated with the lens. The horn's phase center is aligned with the lens's focal point throughout the band of interest with its phase center variation (PCV) tuned by varying aperture width, h_{aw}, and axial length, h_{al}. The resulting values for horn parameters are shown in Table 3.1. The horn's PCV, calculated by the slope method [82], is 0.6 mm around a point 0.15 mm above the aperture. To maximize aperture efficiency of the antenna system, lens's illumination taper is 11 dB [83]. For easy assembly of the prototype, the section of straight guide is increased to h_{sl} = 8.25 mm. The horn's interface to the common junction of the OMT is

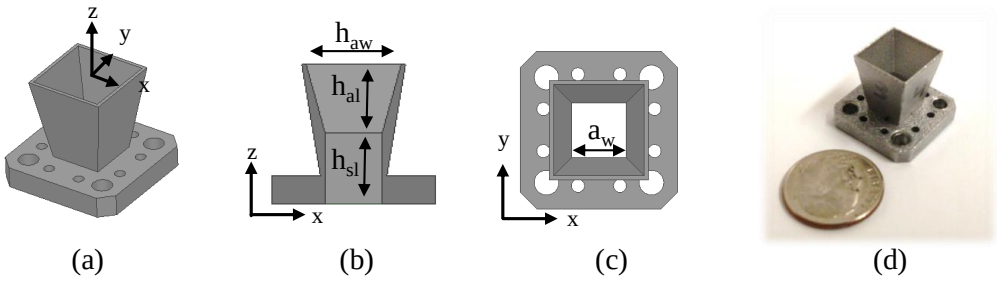

Figure 3.4: (a) Perspective view of the feed horn, (b) Side view through the middle of the horn, (c) top view of the horn and (d) picture of the 3D printed horn with a dime for scale. Values for all parameters are listed in Table 3.1

Table 3.1: Square Aperture Horn Parameters

Parameter	Value [mm]	Description
h_{al}	8	Axial Length
h_{sl}	8.25	Straight Section
h_{aw}	11	Aperture Width
a_w	6.6	Width Waveguide

square with a_w of 6.6 mm. Unlike an ideal Luneburg lens, the two-layer stratified lens is not well matched to free space, and thus affects the antenna return loss. The simulated reflection coefficients of the feed horn with and without the lens are below -12 and -20 dB, respectively, as shown in Fig. 3.5. Differences between the two full-wave methods for the case with the lens is due to the impact of meshing peculiarities between the finite element method as implemented in Ansys HFSS [64] and the finite integral time domain method in CST [66].

3.1.3 Far-Field Performance

The measured circularly polarzied (CP) patterns with and without the lens are shown in Fig. 3.6. CP is chosen since the BC-BFN enables dual-CP. As expected, over the band, the half power beamwidth (HPBW) is consistent between 10.5° and 10°, whereas the sidelobe levels (SLLs) remain lower than -17.5 dB. Due to the PCV and imperfections of the horn pattern, the SLLs are slightly higher than those obtained with the theoretical lens illumination. Similarly like with the

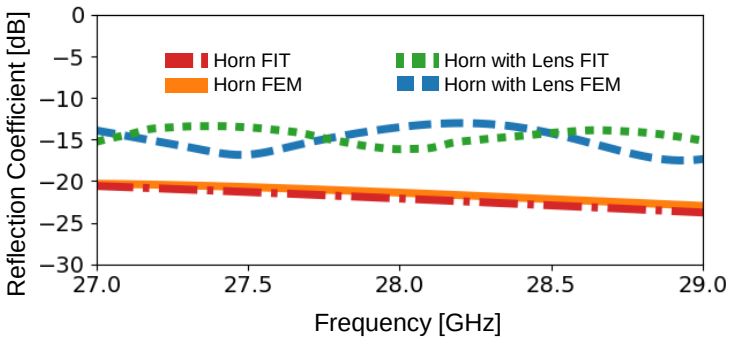

Figure 3.5: Simulated reflection coefficients of the horn with and without the lens utilizing two different computational methods (FEM-Ansys HFSS [64] and FIT-CST MST [66]).

patterns, the measured directivity aligns well with simulations (see Fig. 3.7) and ranges from 10.1 to 10.4 dBic for the horn without the lens and 24.5-24.1 dBic for the horn with the lens.

3.1.4 BC-BFN Sensitivity to Lens Displacement

The imperfect placement of the lens above the dual-polarized horn leads to electrical asymmetry impacting the system isolation when integrated with a BC-BFN network. A sensitivity study to positioning imperfections is carried out with Ansys HFSS [64]. Shown in Fig. 3.8(a) is the self interference (SI) based on (2.15) computed for different offsets of the lens from the feed axis. As clearly seen, the effect of the lens positioning imperfections on the system's coupling is not significant as long as the misalignment errors remain small, that is practically feasible to realize. Specifically, the highest coupling is -44 dB obtained when the lens is offset by 5.5mm which coincides with the edge of the horn's aperture. This extreme case should not happen in practice. Closer to the center of the contour plot, the coupling is extremely low, below -70 dB for displacement values of less than 1 mm.

Deeper examination of the contributions of each part of (2.15) reveals some underlying features that can be seen in Fig. 3.8(b) and (c). S_{21} is nearly zero along the axes while $\Gamma_2 - \Gamma_1$ is nearly zero along the diagonals. Examining the symmetry at these points indicates the presence of some theoretical zeros at different positions. These locations are identified in Fig. 3.9 and are

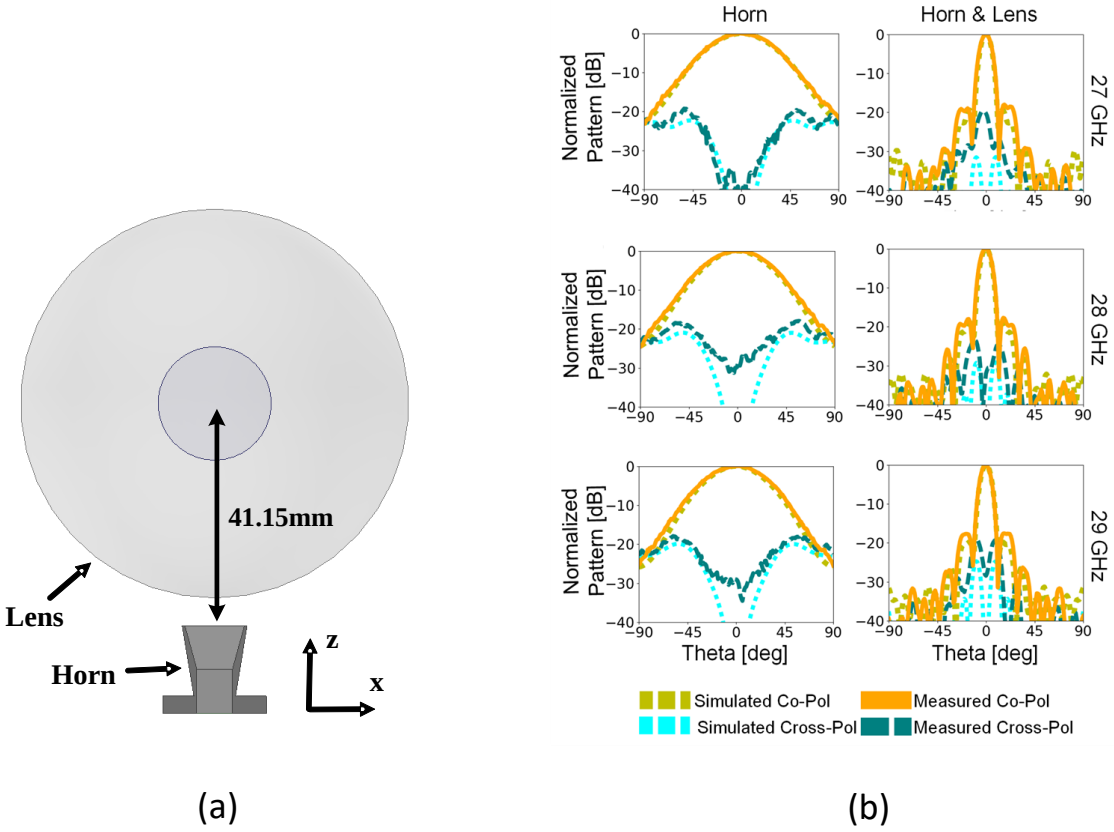

Figure 3.6: (a) Diagram showing a side view through the middle of the horn and the lens and (b) simulated (HFSS) and measured normalized CP elevation cuts of the horn with and without the lens.

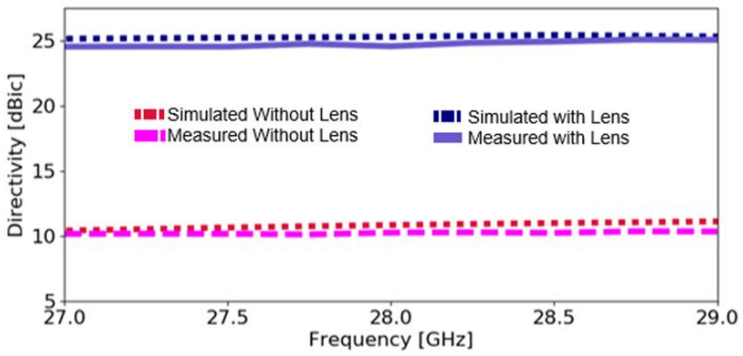

Figure 3.7: Simulated and measured directivities with and without the lens

explained as follows:

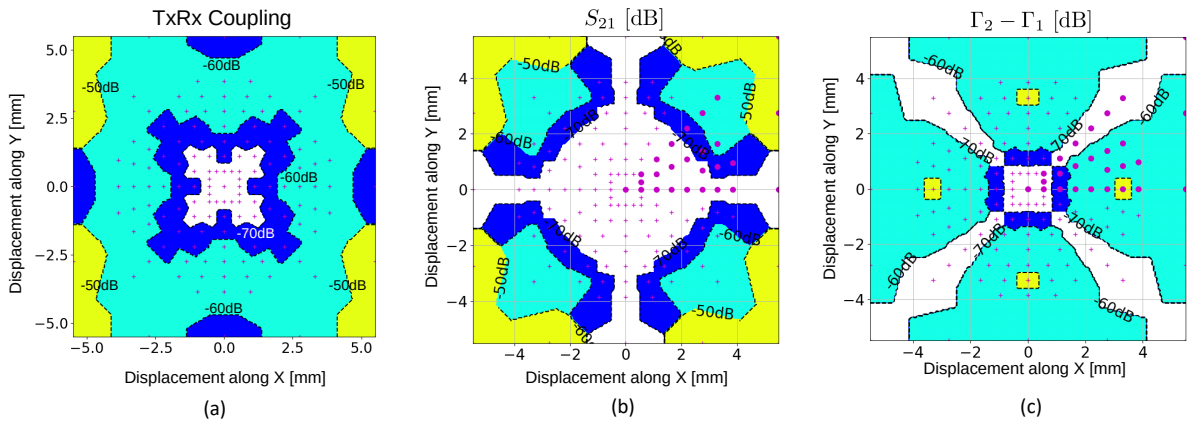

Figure 3.8: (a) Contour map of the Tx/Rx coupling at 28 GHz as the lens if offset from its center position. The BC-BFN is ideal with identical hybrids and circulators. The small crosses are the positions simulated. The model used circulators with a 30 dB isolation. (b) Magnitude of S_{21} at the different positions. (c) Magnitude of the $\Gamma_2 - \Gamma_1$ term at the different positions.

(A) $x = 0$ and $y = 0$: Perfectly centered and ideal case. Would yield perfect isolation with a perfect OMT and BFN. $S_{21} = 0$, $\Gamma_2 - \Gamma_1 = 0$.

(B) $x \neq 0$ xor $y \neq 0$: Offset along an axis, aligned with a mode. Possesses enough symmetry for the coupling between polarizations to still be zero but yields unequal reflection coefficients. $S_{21} = 0$, $\Gamma_2 - \Gamma_1 \neq 0$.

(C) $x = y \neq 0$: Offset along the diagonal. This case is reflection symmetric but the coupling between polarizations is generally non-zero $S_{21} \neq 0$, $\Gamma_2 - \Gamma_1 = 0$.

(D) $x \neq 0$, $y \neq 0$, and $x \neq y$: General case. This case has no special symmetry and in general none of the quantities critical for BC-BFN STAR will be zero. $S_{21} \neq 0$, $\Gamma_2 - \Gamma_1 \neq 0$.

Much as the SI will never be truly zero in simulation, these individual symmetries too will be limited by the numerical noise floor.

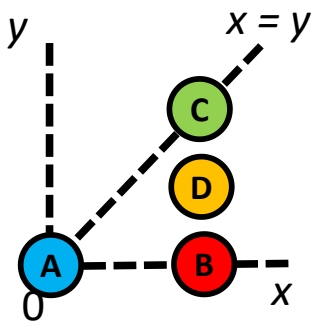

Figure 3.9: Identification of 4 different cases when examining sensitivity of the system to the lens' displacement.

3.1.5 Isolation Measurements

The OMT discussed in Chapter 2 is designed to excite the antenna with dual polarized waves and for corresponding operation. Fig. 3.10 shows the measured network parameters for the OMT with and without the lens. As seen, the reflection coefficients at both ports are increased with the lens, but the system's match remains better than -10 dB. The port-to-port coupling is also increased but remains below -50 dB for most frequencies. These measurements show that the mechanism by which the lens can be expected to noticeably degrade SI cancellation is through modulation of the reflection coefficients.

To experimentally assess and demonstrate the impact of the lens on the BFN, three circulator-based STAR configurations, seen in Fig. 3.11, are assembled and tested. Shown in the same figure are pictures of the assembled BFN's. The single circulator configuration in Fig. 3.11(a) produces dual-linear polarization and the system in Fig. 3.11(d) creates dual-circular operation, which is a fairer comparison to the BC-BFN shown in Fig. 3.11(g) which also produces circular polarization. All three use the same COTS components and hybrids that were used in the BC-BFN described in Chapter 2. The WR28 OMT fed horn with and without the lens is used as the dual-polarized

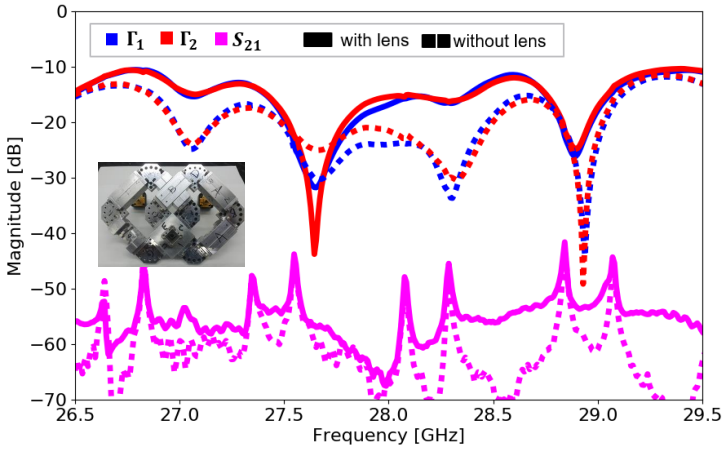

Figure 3.10: Measured S-parameters for the OMT/antenna system with (solid) and without (dotted) the spherical lens in place.

antenna.

The dual-linearly polarized system has comparable performance for both channels, with Fig. 3.11(c) showing the results for Γ_1(from Fig. 3.10). The effect of the lens is clear as it raises the reflection, which are directed to the Rx port; thus increasing the coupling. The couplings in the dual-CP system with and without the lens are shown in Fig. 3.11(f). As seen, the effect of the lens is barely noticeable because the lens' reflections have the opposite CP handedness. In both cases, the isolation is worse than that of the circulator itself. The results for the fully assembled BC-BFN with the antenna, with and without lens, are shown in Fig. 3.11(i). As expected, the BC-BFN has a better performance than the two conventional circulator configurations. Also seen is that the lens increases the system's worst case coupling from -34 to -30 dB, a result adjudicated to the imperfect two-layer configuration of the lens. Specifically, the increased reflection coefficients with the lens observed in Fig. 3.10 combined with other imbalances in the BC-BFN, lead to increased coupling between the Tx and Rx ports. Overall, compared with the two single circulator topologies, the BC-BFN has about 19 and 15 dB on average better isolation than the dual-circular and dual-linear single circulator based configurations, respectively. The measured isolation of the COTS circulators used in the BC-BFN's construction is surpassed by an average of 9.6 dB with the lens in place.

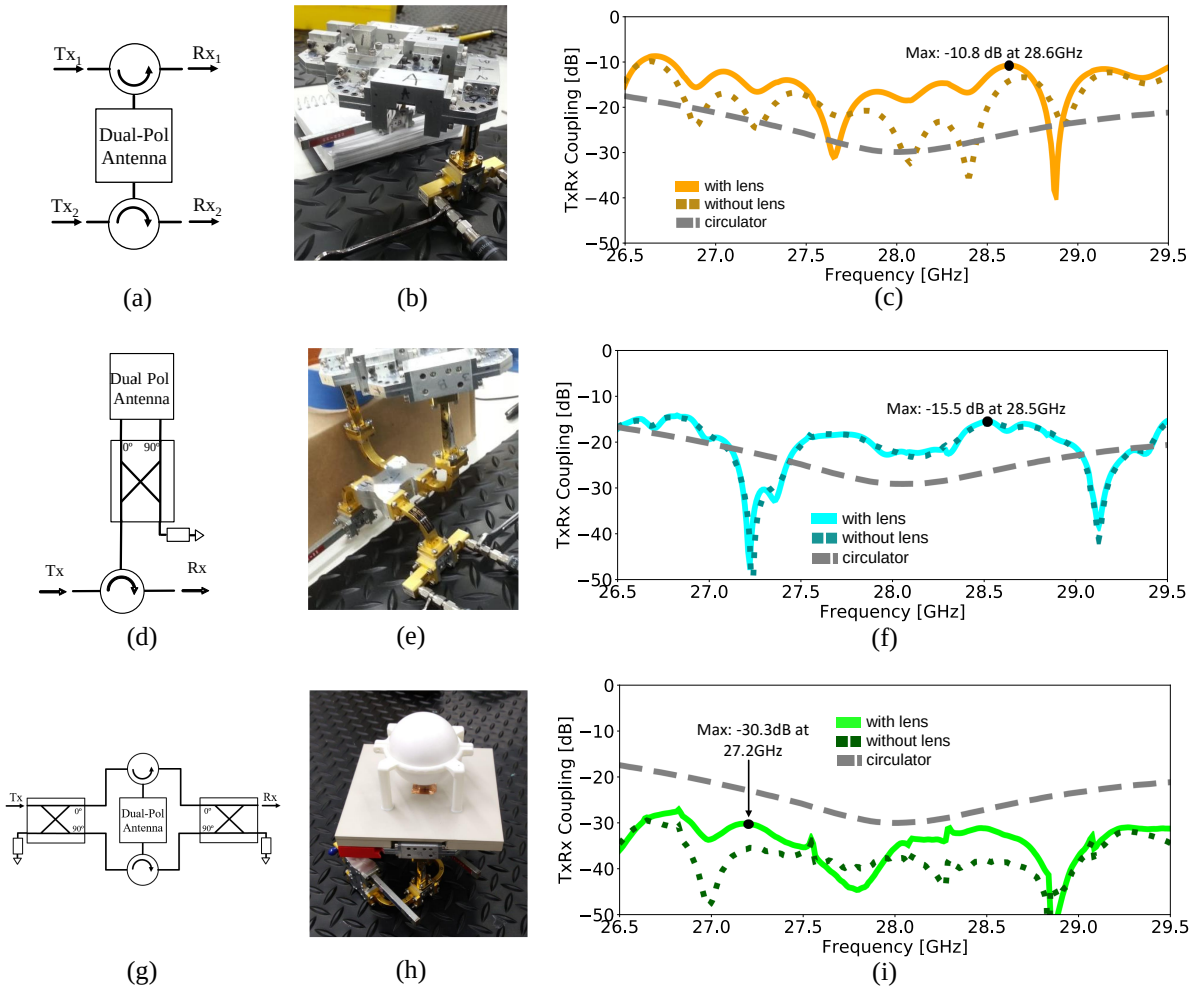

Figure 3.11: (a) Schematic showing single circulator dual-linear based STAR. (b) Picture of realized single circulator system (c) Measured Coupling between the Tx and Rx channels in the single circulator system. (d) Schematic showing single circulator CP based STAR. (e) Picture of realized single circulator CP system (f) Measured Coupling between the Tx and Rx channels in the single circulator CP system. (g) Schematic showing BC-BFN. (h) Picture of realized BC-BFN with the spherical lens (i) Measured Coupling between the Tx and Rx channels in the BC-BFN subsystem. All realized systems use the same COTS components and hybrids. Individual circulator performance used in the measurements is included for reference.

Finally, note the insertion loss of the BC-BFN from the input of the hybrids to the output of the OMT was measured to be around 0.95 dB for both the Tx and Rx channel. The BC-BFN's insertion loss is almost identical to that of the single circulator with hybrid configuration since the difference between these two configurations is an added H-plane bend in the signal path which contributes

less than 0.1 dB to the measured loss. The average losses are 0.97 dB for the single circulator with hybrid (Fig. 3.11(e)) and 0.70 dB for the single circulator (Fig. 3.11(b)). The latter has a small insertion loss due to the lack of the hybrid and H-bends as pictured.

3.2 Spherical Half-Lens for Beam Scanning

To scan the beam with the previously discussed configuration one can either move the feed along the focal arcs or switch between different antennas in a feed manifold. Whereas the former is not practical due to the fixed waveguide plumbing, the latter is challenging due to the high cost and practical realization. Instead, a mechanically moving half-lens with fixed feed [84, 85] is a viable approach to achieve scanning. By placing a ground plane through the equator of a spherical lens, as shown in Fig. 3.12, we can obtain the same increase in directivity as with the full spherical lens. The angle of the reflected beam will follow Snell's law; therefore, scanning is achieved by changing the angle of incidence [86]. By judiciously truncating the size of the ground plane and mounting the lens and plane in such a way that the plane and the lens rotate about the center of the lens as shown in Fig. 3.13, it is possible to scan the beam [84–86]. Rotations of the type shown in Fig. 3.13(a) will modify the elevation angle and those of the type in Fig. 3.13(b) will modify the azimuth. Generally speaking, the antenna is aimed in new directions by combining both. Theoretically, the resulting beams are identical with the resolution of the angles that can be scanned limited by the employed control system. Details of how the mechanical motion is achieved are omitted since they are beyond the scope of this work, however, [84] presents a possible implementation that allows moving the lens with the required degrees of freedom. To the author's knowledge, these antenna systems have not been evaluated for in-band full-duplex operation. The chief challenge for isolation is the asymmetry of the scattering environment beyond the horn. As discussed in Chapter 2, this affects the performance of the BC-BFN system which relies on a symmetric environment to achieve high Tx/Rx isolation. Chapter 4 discusses a system with a planar lens which achieves mechanical steering over a conical path around broadside. The STAR configuration introduced here is able to span full 360° azimuth and wide off-horizon angular coverage.

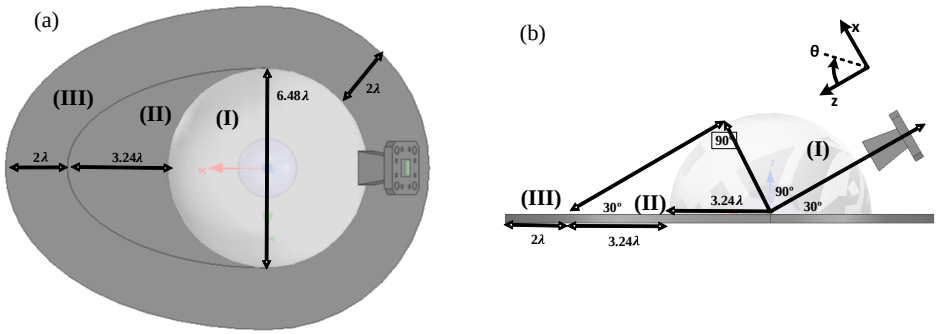

Figure 3.12: Gimbal lens schematic (a) top and (b) side views. Identified with roman numerals are: (I) Half lens version of the lens in Fig. 3.3; (II) lens shadow area whose size is determined from the geometry of the lens; and (III) expanded ground area needed to reduce edge-diffraction effects. All dimensions are for 27 GHz which is the lowest frequency considered here.

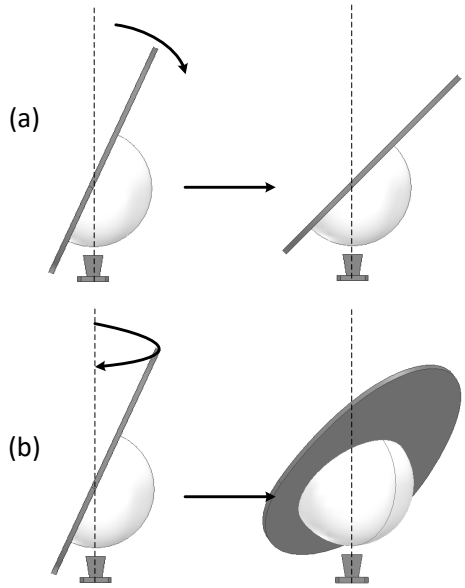

Figure 3.13: Diagram showing (a) how the lens rotates to change the elevation of the beam and (b) how the lens rotates to change the azimuth of the beam.

3.2.1 Rotating Half-Lens Design

A rotating half-lens as shown in Fig. 3.12 has three distinguishable areas, denoted by roman numerals:

I Ground backed half-lens version of the spherical lens.

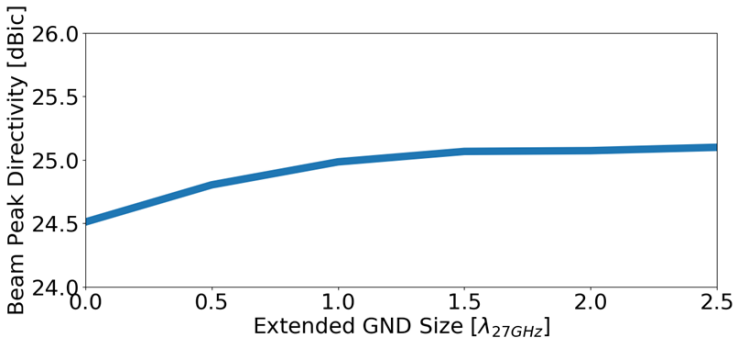

Figure 3.14: Simulated beam directivity at 28 GHz as a function of the expanded ground size. Extending the ground over 2λ has minimal impact on directivity. The angle of the selected beam is 60°.

II Lens shadow area whose size is determined from the geometry of the lens. In a geometrical optics derivation, the rays from an ideal Luneburg lens would impact this area.

III Expanded ground for reducing edge-diffraction effects which size is found by ensuring the convergence of a desired far-field parameter (directivity in our case, see Fig. 3.14). Its size coincides with that reported in the open literature [85].

The half lens was fabricated using a computer numerical control (CNC) machine to create the rexolite half sphere and the PTFE outer shell. The outer shell is affixed to the aluminum GND plane using nylon screws. No adhesives or screws are used on the rexolite. Rather, the outer shell presses it against the plane.

3.2.2 Half-Lens Coupling Measurements

The addition of the ground plane introduces a highly reflective surface near the horn in a manner that creates an asymmetric scattering environment between orthogonal linear polarizations of the system. As seen in Fig. 3.15, the effect of these imperfections results in a 2.5 dB increase in coupling when comparing to the spherical configuration.

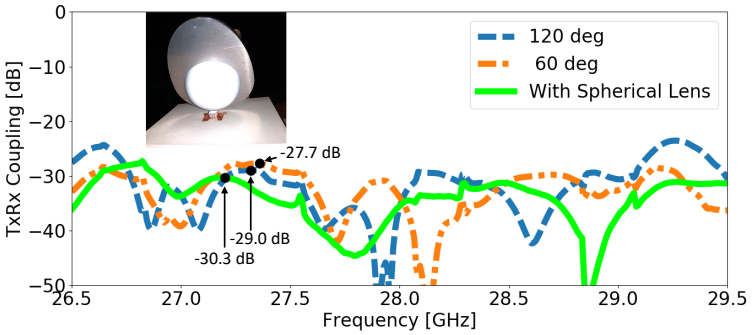

Figure 3.15: Tx/Rx coupling in the presence of the gimbal lens. The degrees indicate the direction of two of the beams whose isolation was tested. The markers indicate the peak SI for each curve.

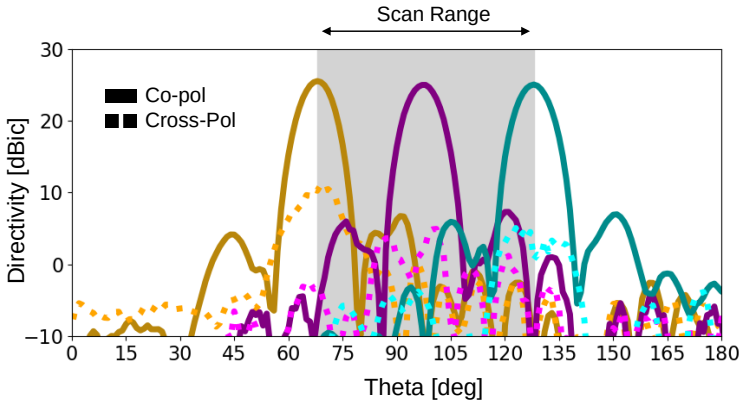

Figure 3.16: Measured CP patterns for the rotating half-lens. The scan range measured extends from 68° to 128°. Coordinate system shown in Fig. 3.12.

3.2.3 Half-Lens Far Field Performance

The measured patterns for three different beams are shown in Fig. 3.16. As seen, the co-polarized main beams suffer little to no change between the considered scan angles. The difference in cross-polarization levels is expected due to the asymmetry. In-band directivity remains similar for all three angles; varying across frequency from 25.1 to 25.4 dBic for the 60° beam, 24.6 to 25.2 dBic for the 90° beam, and 24.8 to 24.5 dBic for the 120° beam. These values are consistent with the 24.5-25.1 dBic range obtained for the full spherical lens. The pattern parameters at 28 GHz have been summarized in Table 3.2 for a side by side comparison. It is clear that the beam scanning does not result in noticeable degradation of the pattern through scan loss or other changes.

Table 3.2: Rotating Half Lens Pattern Properties

	Spherical Lens	60° Beam	90° Beam	120° Beam
HPBW	10°	8.7°	9.1°	9.1°
Directivity [dBi]	24.6	25.5	25.0	25.1
SLL [dB down]	18.0	18.8	17.5	18.1

3.3 Conclusion

A waveguide-implemented BC-BFN is used to achieve dual-polarized, high directivity full-duplex STAR with a spherical and rotating spherical half-lens. The sensitivity of the full spherical lens based system to alignment imperfections is found to be small. SI cancellations of 30 and 34 dB are achieved with and without the lens in the assembled system; a considerable improvement over the single circulators configurations that achieved -10 dB without the hybrid and -15 dB with the hybrid in place. To overcome the limitations of the fixed beam and demonstrate scanning around the horizon, the rotating half-lens configuration is designed and tested. Acceptable isolation with consistent scanned patterns comparable to those of the full-spherical lens are measured demonstrating a full beam scanning capable STAR system. The results presented in this chapter show that care needs to be taken when designing spherical lenses for STAR performance. The asymmetries and imperfections impact the isolation and its performance, however, viable solutions that work well in full-duplex environment and as antenna are still possible. Impact of these scatterers in the vicinity of the BC-BFN is characterized and shown to be acceptable. This chapter clearly demonstrates that highly directive steerable STAR systems are possible at millimeter wave frequencies.

Chapter 4

Flat GRIN Lens STAR Subsystem

In this chapter, a flat graded index (GRIN) lens is proposed as a viable alternative to the Luneburg lens from the previous chapter to achieve a high-directivity beam-steerable monostatic-STAR system. There are multiple ways to manufacture these lenses, including composite materials [44], machined substrates [45, 46], and 3D printing cylindrical GRIN structures using partially air-filled dielectrics in millimeter wave applications [47–51]. As seen, the 3D printing leads to practical manufacturing of lightweight lenses that provide high directivity while maintaining scanning operation. Some flat GRIN lenses from the literature are shown in Fig. 4.1.

References [44, 45, 51] present beam scanning by switching between different antennas positioned off the optical axis. While fast, this technique incurs a significant amount of scan loss since antennas are displaced from the focal point and the rays are not properly colimated. The work herein presents simulated and measured results for a novel way to mechanically scan the cylindrical GRIN lenses. At the cost of speed, this method will be shown to produce beams that maintain higher directivity over a broader range of scan angles. The viability of beam steerable STAR using the BC-BFN is demonstrated. The lenses discussed herein should not be confused with the planar lenses discussed by [87, 88]. In the former, parallel plates are used to create the delays whereas in the later a 2D cut of a conformally mapped luneburg lens is used to create a focal surface along a straight line.

This chapter is organized as follows:

- Section 4.1 covers the design of a planar GRIN lens antenna.

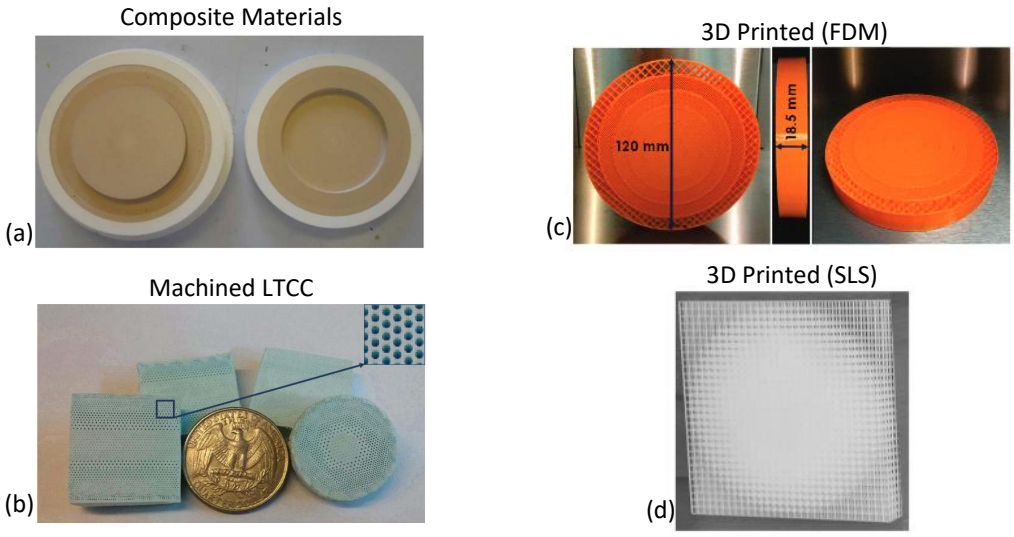

Figure 4.1: Selection of GRIN lenses built with different techniques. (a) Lens from [44], fabricated by molding resin shells mixed with ceramics to achieve the desired permittivity profile. (b) Lenses from [45] fabricated by drilling holes in low temperature co-fired ceramics to achieve the needed gradient. (c) 3D printed lens from [47] fabricated out of polylactic acid (PLA) using fused deposition modeling (FDM). (d) Selective Laser Sintering (SLS) manufactured lens from [48].

- Section 4.2 presents the proposed scanning method and contrasts it with beam switching techniques from the open literature.
- Section 4.3 discusses the process to design the effective dielectric materials needed to recreate the permittivity distribution of the lens.
- Section 4.4 shows the data obtained from far field measurements and contrasts it to the full-wave simulations.
- Section 4.5 provides summary and conclusions on the results obtained in this chapter.

4.1 Planar GRIN Lens Design

4.1.1 General Design Equations

The design of the lens is based on the field transformation method described in [47]. This is not the only way to obtain the flat GRIN lenses. [44] uses transformation optics to conformally map

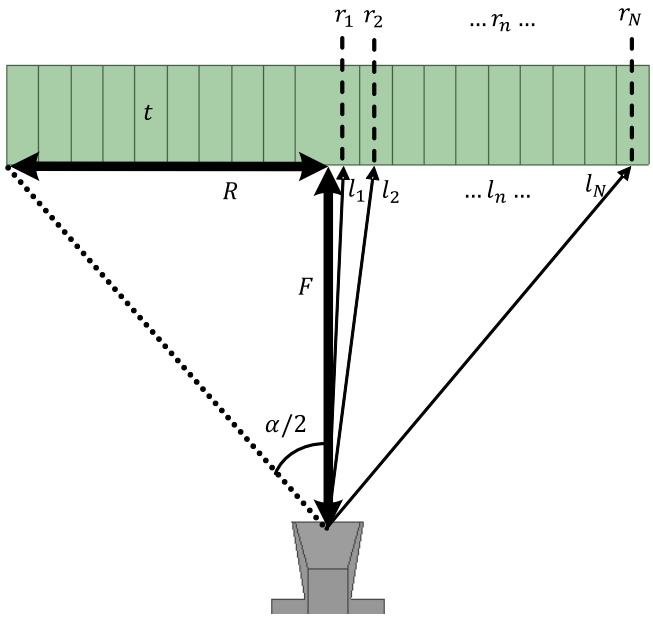

Figure 4.2: Side view of the lens-antenna subsystem with the labeled variables

the spherical Luneburg solution to a disk. The mapping results in a lens that has index gradations along both the radial and height dimensions. Using the field transformation method in [47] results in a lens with uniform permittivity along the height of the lens.

The lens herein presented uses a set of concentric rings, each with a different index of refraction. The index of refraction is varied radially such that a plane wave incident on one face of the lens exits the opposite face with a phase delay that closely approximates a spherical wavefront. The focal length, F in Fig. 4.2, is the distance to the focal point where the rays from this spherical wave add constructively. By reciprocity, the rays of an antenna with its radiation phase center at this focal point will be collimated into a plane wave on the opposite side, resulting in increased directivity. Using the geometry in Fig. 4.2, the equations to design the lens are:

$$k_0 l_i + k_i t = k_0 l_n + k_n t \tag{4.1}$$

$$l_n = \sqrt{F^2 + R^2 \left(\frac{1 + 2(n-1)}{2N} \right)^2} \tag{4.2}$$

$$l_i + t\sqrt{\epsilon_r(r_i)} = l_n + t\sqrt{\epsilon_r(r_n)} \tag{4.3}$$

$$t = \frac{l_N - l_1}{\sqrt{\epsilon_{r,\max}} - \sqrt{\epsilon_{r,\min}}} \tag{4.4}$$

Equation (4.1) relates the electrical length of two from an incident plane wave as they reach the focal point, at a distance F from the surface of the lens. One ray goes through the i-th ring with wavenumber k_i while the other goes through the n-th ring having wavenumber k_n. The indices i and n are integers ranging from 1 to N, N being the number of rings used. l_n are the physical lengths of the paths between the focal point and the mid-radii of each ring, as shown in Fig. 4.2. Through geometry, (4.2) can be determined which relates the path lengths, l_n, to the focal length, F; lens radius, R; and number of rings, N. Dividing (4.1) by the free space wavenumber, k_0, results in (4.3). If the relative permittivities of the rings, $\epsilon_r(r_i)$, are constant enough with frequency then (4.3) is a frequency independent design equation for this kind of lens. Solving (4.3) for the thickness, t, using the first and last rings yields (4.4). The substitutions $\epsilon_{r,\max} = \epsilon_r(r_1)$ and $\epsilon_{r,\min} = \epsilon_r(r_N)$ have been made to emphasize that this relates the range of permittivities that can be printed. From (4.4) it can be seen that a larger range in the achievable permittivity will lead to thinner lenses. Conversely, if the fabrication process is limited to a narrow range of permittivities, the lens will have to be thicker to compensate for the proper phase delays. The distance through the center of the lens is shorter than the distance through the edge of the lens so the maximum permittivity is found at the center and tapers off towards the edge.

4.1.2 Design of the Lens Antenna

The initial lens design was to use the full range of permittivities available in the 3D printer's resin. More details on material measurement and design are provided in the following sections but initially it suffices to know that solid sample of Formlab's Tough RS-F2-TOTL-05 resin was measured to have a permittivity of 2.9 and this was used as the upper bound in the initial designs.

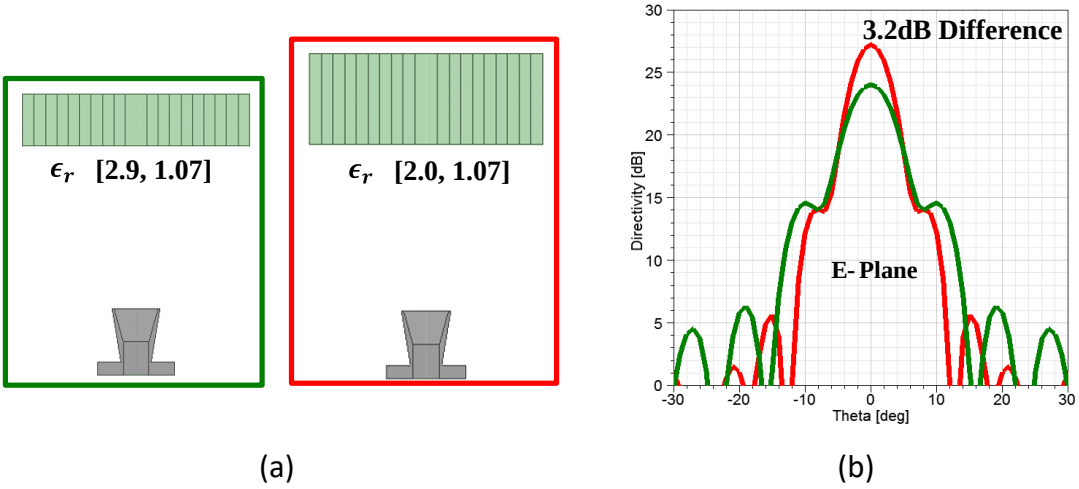

Figure 4.3: Comparison of the two permittivity ranges. (a) Side view of the lenses enclosed in colored squares that correspond to the plots in (b) which shows the E-Plane cut of the directivity at 28 GHz. An increase in peak directivity of 3.2 dB is observed with the smaller permittivity profile.

The lower bound was selected to be 1.07 as this is the permittivity of Rohacel 31 HF. As in [51], this would be a viable replacement for the 3D printed material for the outer ring, where manufacturing limitations would restrict the lowest obtainable permittivity. The resulting lens had unexpectedly low directivity and it was found that by reducing the range of permittivities a significant increase in directivity was obtained. The comparison between a lens with the first range, 2.9-1.07, and a second lens with the permittivity range of 2.0-1.07 is seen in Fig. 4.3. The improvement is adjudicated to the improved match between air and the lens layers when a lower permittivity is used.

Another parameter to tune is the subtended angle, α, identified in Fig. 4.4(a). This parameter controls how the antenna illuminates the lens and is related to the radius, R and focal length F by expression (4.5).

$$\tan\left(\frac{\alpha}{2}\right) = \frac{R}{2F} \tag{4.5}$$

Constraining F to 40 mm and generating the requisite 10 layer lenses with a permittivity range of 2 to 1.07 allowed doing a sweep in subtended angle. This implies a change in the radius of the

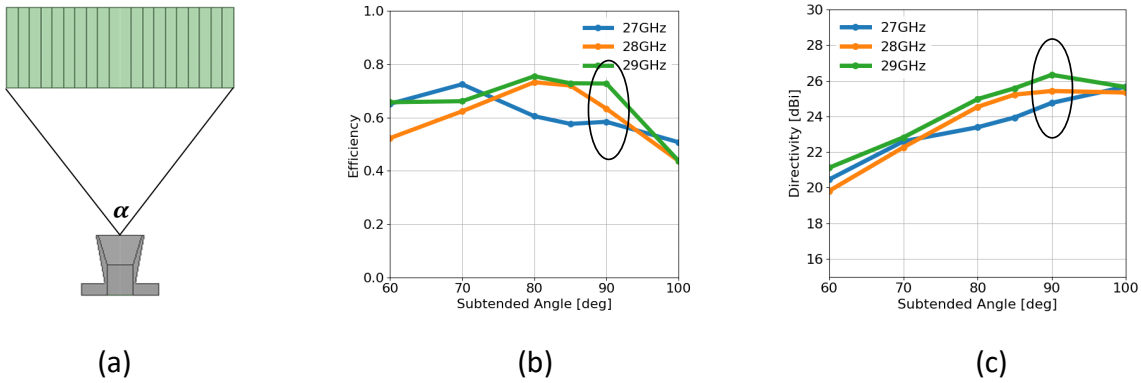

Figure 4.4: (a) Side view identifying the subtended angle, α. (b) Aperture efficiency as the value of α is varied. (c) Peak directivity as the value of α is varied.

different lenses. Circled in Fig. 4.4(b) and (c) are the aperture efficiency and directivity for $\alpha = 90°$ which yielded the best result among the values sampled. This α corresponds to $R = 80$ mm.

With the goal of reducing the complexity of the design, the effect of the number of rings was studied. The model shown in Fig. 4.5(a) was chosen. It has 4 rings, contrasted to the 10 rings being used in the previous models. Using between 10 and 4 rings had little effect on the directivity but Fig. 4.5(b) shows how with 3 and 2 rings the directivity drops off sharply. The dimensions of the final design are summarized in Table 4.1. The feed antenna is the square aperture horn discussed in Chapter 2. The simulated and measured far-field performance will be discussed in a later Section 4.4.

4.2 Scanning with the Planar GRIN Lens

4.2.1 Rotating the Lens

When offsetting the lens from the focal length as shown in Fig. 4.6(a) to scan the beam it is seen that the beam quality quickly degrades. The blue curves in Fig. 4.6(c) show the directivity for $\beta = 10°$, $20°$, $30°$, $40°$. The beam at broadside ($\beta = 0°$) is shown in black. Not only is directivity reduced but there does not seem to be a simple relation between β and the angle of the far-field

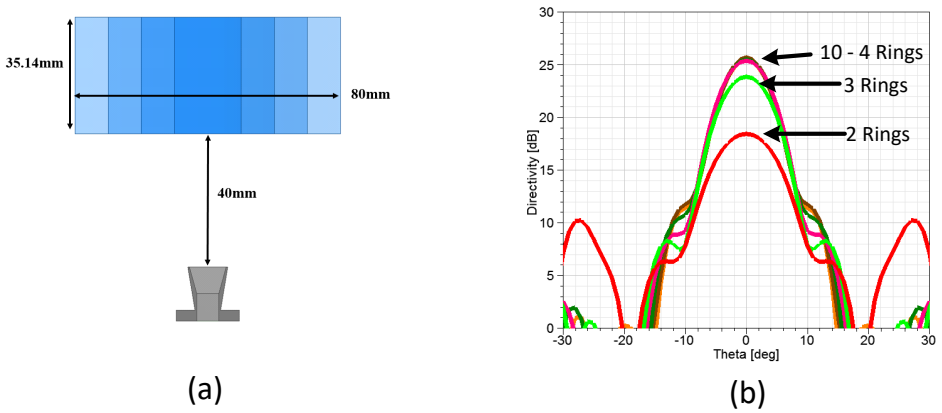

Figure 4.5: (a) Side view of the final lens with 4 rings. Key geometrical dimensions are indicated. (b) E-Plane directivity at 28 GHz as the number of rings, N, is varied from 10 to 2. 10-4 rings are indistinguishable but at 3 and 2 rings there is significant degradation.

Table 4.1: Cylindrical GRIN Lens Parameters

Parameter	Value	Description
F	40 mm	Focal Length
R	40 mm	Lens Radius
α	90°	Subtended Angle
t	35.14 mm	Lens thickness
N	4	Number of rings
$\epsilon_r(r_1)$	2.00	Relative permittivity at the center ($\epsilon_{r,\max}$)
$\epsilon_r(r_2)$	1.81	Relative permittivity at the second ring
$\epsilon_r(r_3)$	1.49	Relative permittivity at the third ring
$\epsilon_r(r_4)$	1.07	Relative permittivity at the outer ring ($\epsilon_{r,\min}$)

beam. To mitigate the scan loss a new method of scanning is proposed, as schematically shown in Fig. 4.6(b). The approach is to keep the horn static while moving the lens in an arc such that the focal point always remains at the antenna's phase center. The resulting beams for inclinations of $\theta = 10°, 20°, 30°, 40°$ are seen in red in Fig. 4.6(c). They are seen to outperform the blue curves, allowing for a wider scan angle with lower scan loss, and the angle θ accurately predicts the direction of the resulting beam. When contrasted with the array element switching discussed in [45, 51], this method sacrifices the switching speed for better far-field performance. Another positive when compared to the array-element switching method is that the resulting beams are

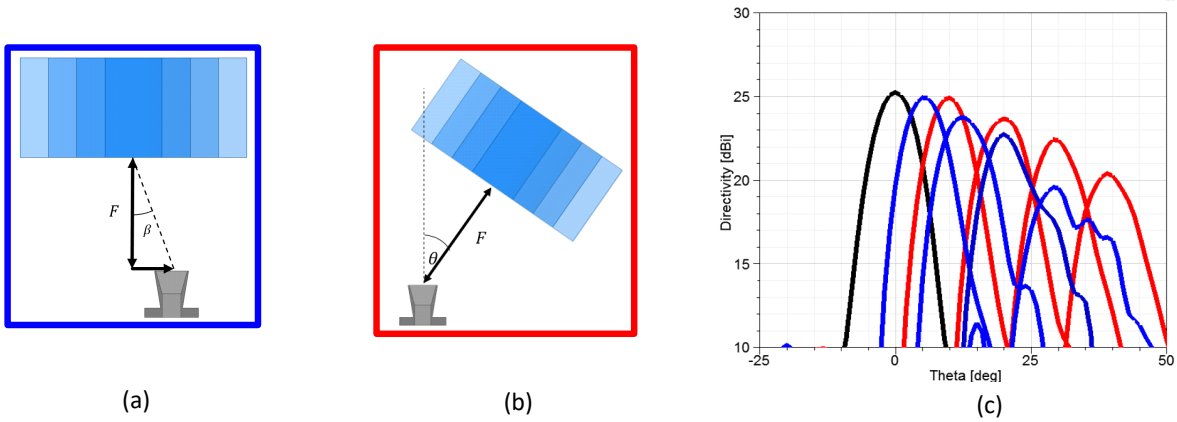

Figure 4.6: (a) Scanning by offsetting the antenna from the focal point. Implemented by switching between array elements in [45, 51]. (b) Scanning by rotating the lens while keeping the focal point at the antenna's phase center. (c) Directivity for both plots. The blue is for the configuration in (a) and the red for the configuration in (b). The black pattern is the broadside pattern which is common for both cases.

not limited to discrete positions. Instead the full conical area is potentially available, subject to the accuracy of the mechanical control system. This method allows for the lens to be swept in inclination and azimuth while keeping the focal point on the antenna.

Fig. 4.7 shows the result form beam scanning with more detail. As mentioned before, within the angles tested, the correspondence between the lens' inclination and the beam direction is exact; meaning if the lens is inclined at 20°, the beam is directed at $\theta = 20°$. The scan loss up to 40° of inclination is less than 4.6 dB along both planes of symmetry of the CP horn. In both planes, it can be seen that as the lens moves further away from zenith, the spillover radiation from the feed becomes more pronounced. In Fig. 4.7 this effect is visible as the directivity increases at $\theta = -15°$. which is still 10 dB down from the main beam at an inclination of 40°. This increased spillover as well as non-optimal illumination of the lens at lower angles leads to the scan loss visible in the results. The axial ratio is predicted to degrade as the beam is scanned but in simulation the worst case is at $\theta = 40°$ where the AR at the peak of the beam degrades to 1.4 dB. Due to the electrical symmetry of the problem, these results can be extended for all azimuth angles on an 80° cone (i.e. from $\theta = -40°$ to $\theta = 40°$)

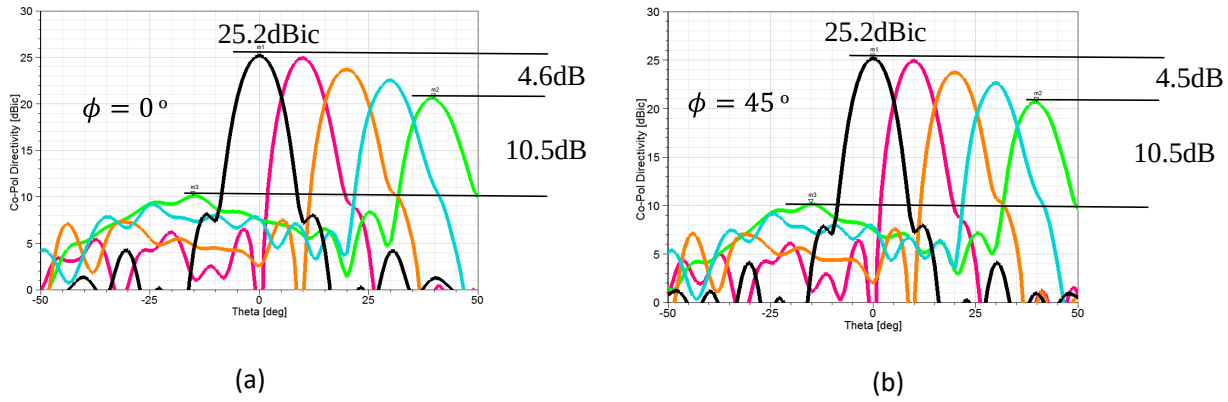

Figure 4.7: (a) Simulated scanning at $\phi = 0°$. (b) Simulated scanning at $\phi = 45°$. The inclination is $\theta = 0°$, 10°, 20°, 30°, 40°. All patterns are CP. Cross-pol is too low to be shown on this scale.

4.2.2 Effect on STAR Subsystem Performance

Similar to the analysis performed for the spherical lens in the previous chapter, the S-parameters are used to evaluate how this mechanical beam steering with the planar lens affects the expected Tx/Rx isolation. Fig. 4.8 summarizes the results. The use of three different azimuth angles is to illustrate sensitivity across the different symmetry cases as identified in Fig. 3.9. $\phi = 0°$ corresponds to case B, 45° corresponds to C, and 22.5° corresponds to case D. Case A happens when the inclination, θ, is zero in all the plots.

Fig. 4.8 shows that both S_{21} and $\Gamma_2 - \Gamma_1$ are elevated when the lens is offset in this asymmetrical way. The isolation results shown in Fig. 4.8(g)-(i) for 3 frequencies in the band indicate that an isolation better than 43 dB is achievable at least in simulation. This value is practical when compared to other STAR systems in the literature (see Table 1.2.6).

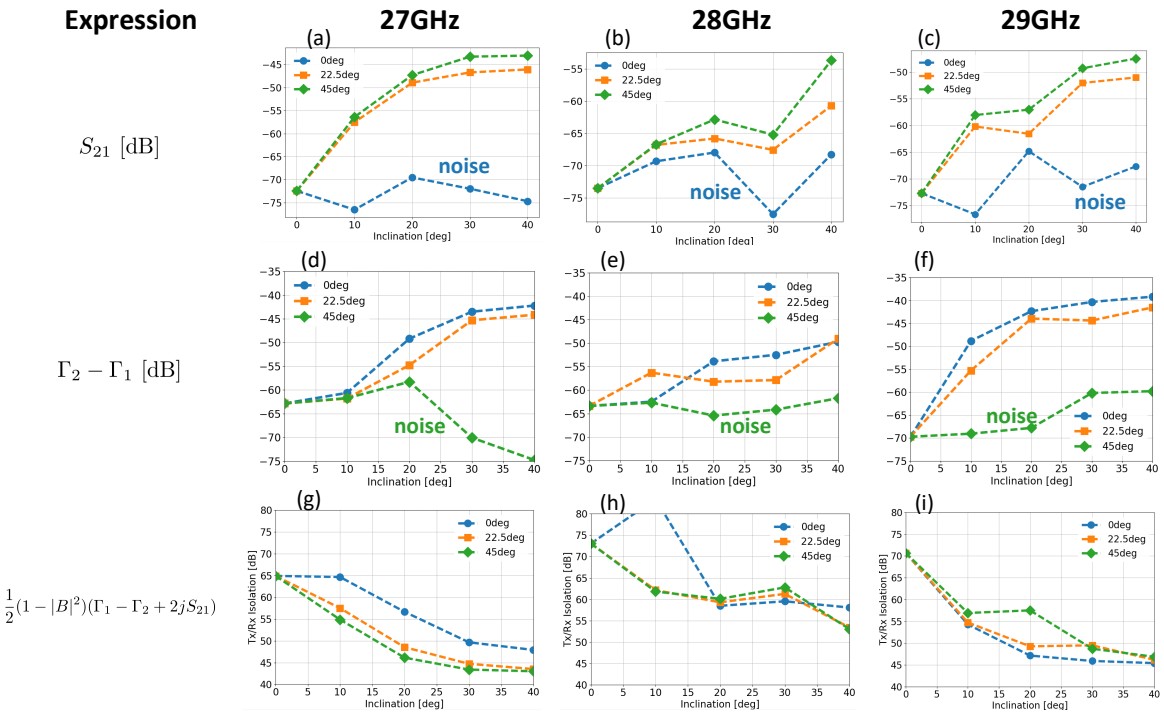

Figure 4.8: Simulated performance with an ideal BC-BFN as the lens is inclined. 3 Different azimuth angles are chosen for each plot to show how the special cases outlined in Fig. 3.9 behave. Plots that should be ideally zero are identified to indicate that they are numerical noise. (a), (b), and (c) are the magnitude of S_{21} at 27, 28, and 29 GHz respectively. (d), (e), and (f) are the magnitude of $\Gamma_2 - \Gamma_1$ at 27, 28, and 29 GHz respectively. (g), (h), and (i) are the Tx/Rx isolation as obtained from (2.15).

4.3 Designing Effective Permittivity for Flat GRIN Lens

4.3.1 Designing Effective Permittivity

In order to fabricate the lens a triangular unit cell such as the one in [45,51,89] and pictured in Fig. 4.9 is deployed. S is the separation between hole centers and as a rule of thumb, kept below $\lambda/3$ at the highest frequency (29 GHz in this case). This size consideration keeps the cell electrically small and the material is effectively uniform. The permittivity is varied by modifying the radius, r, of the holes. More material means a higher permittivity and less a lower permittivity.

The relationship between the achieved permittivity and the physical dimensions is not linear

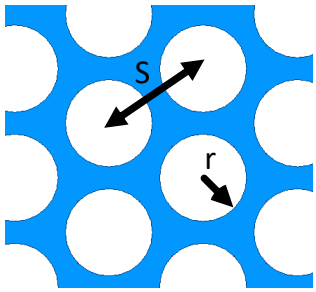

Figure 4.9: Top side of the unit cell. S is the separation between hole centers and as a rule of thumb, kept bellow $\lambda/3$ at the highest frequency (29 GHz in this case). The permittivity is varied by modifying the radius, r, of the holes.

and so a design curve is developed by simulating different unit cells and extracting the resulting parameter. Fig. 4.10(a) shows the simulation setup to extract material parameters. By printing a solid piece of resin, the relative permittivity of Formlab's Tough RS-F2-TOTL-05 resin was experimentally determined to be 2.9. This is obtained by fitting the sample in a flange as shown in Fig. 4.10(b) and measuring the network parameters. To convert these measurements to material parameters, the following equations from [90] are used.

$$\chi = \frac{S_{11}^2 - S_{21}^2 + 1}{2S_{11}} \tag{4.6}$$

$$\Gamma = \chi \pm \sqrt{\chi^2 - 1} \tag{4.7}$$

$$P = \frac{S_{11} + S_{21} - \Gamma}{1 - (S_{11} + S_{21})\Gamma} \tag{4.8}$$

$$\epsilon_r \mu_r = \left(\frac{\lambda}{\lambda_c}\right)^2 - \left[\frac{\lambda}{2\pi l} \ln \frac{1}{P}\right]^2 \tag{4.9}$$

$$\mu_r^2 = \left(\frac{1+\Gamma}{1-\Gamma}\right)^2 \frac{\left(\frac{\epsilon_r \mu_r}{\lambda^2} - \frac{1}{\lambda_c}\right)}{\left(\frac{1}{\lambda^2} - \frac{1}{\lambda_c}\right)} \tag{4.10}$$

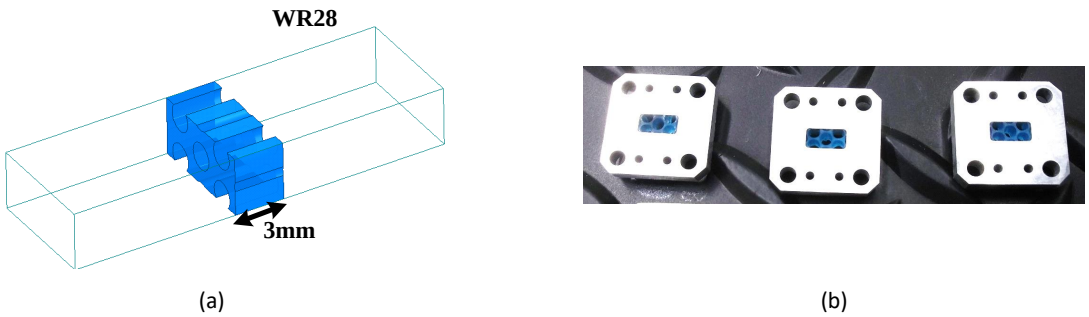

Figure 4.10: (a) Full wave model to simulate the unit cell within a WR28 waveguide. (b) 3D printed samples for measuring.

In the above expressions, λ is the wavelength, λ_c is the wavelength of the guide's cutoff frequency, and l is the length of the sample. The parameters combined with the measured S-parameters (S_{11} and S_{21}) allow determining the relative permittivity, ϵ_r, and permeability, μ_r. A known limitation of these expressions to extract material parameters comes about due to an ambiguity introduced by the complex logarithm calculated in (4.9). This creates a tradeoff between the length of the sample and the highest permittivity that can be unambiguously determined. Fig. 4.11 illustrates this tradeoff. To generate the plots, the S-parameters for an analytical section of WR28 are synthesized. Each section is designed to be filled with a different permittivity. The relative permittivity is varied from 1 to 6. The material in the synthesized sample is calculated at different frequencies, selected to represent $1.0001f_c$, $1.25f_c$, $1.5f_c$, $1.75f_c$, and $2f_c$; f_c being the waveguide cutoff frequency. If there were no ambiguity, all the plots in Fig. 4.11(a) would lie on the $x = y$ diagonal line. The calculated values however deviate from this expected result. Higher frequencies (i.e. when sample is electrically longer) are only able to measure lower ranges of permittivity. Observing this behavior, a sample length of 3 mm was chosen as the measurements could unambiguously determine relative permittivity values below 3 for frequencies under 31 GHz. Fig. 4.11(b) shows that the permeability measurement is similarly affected by the ambiguity. μ_r is maintained at 1 in all the samples synthesized.

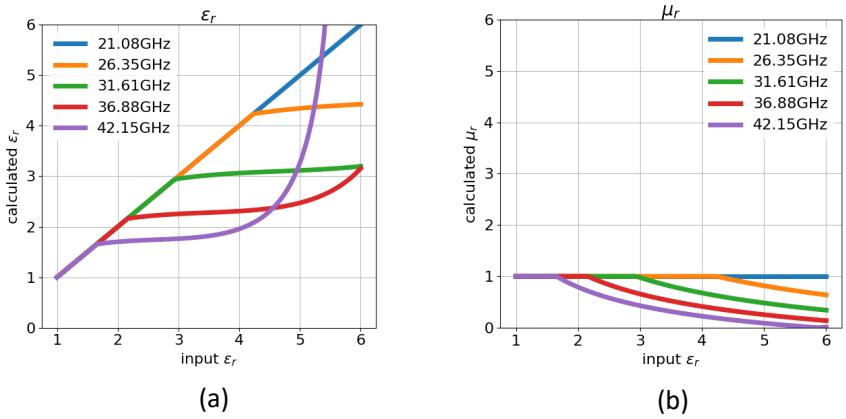

Figure 4.11: Calculated relative permittivity and permeability to illustrate ambiguity. (a) Calculated relative permittivity as the permittivity of the sample is increased. (b) Calculated relative permeability as the permittivity of the sample is increased. S-parameters for the samples are analytically generated for a section of WR28. Input μ_r is maintained at 1 and the sample length is 3 mm

4.3.2 Lens Design and Fabrication

The final design curve is obtained by varying the radius of the holes in Fig. 4.10(a) and is shown in Fig. 4.12. The spacing is kept at $\lambda/3$ at 29 GHz and the length of the sample at 3 mm. The radius of the unit cells for the different rings in the lens are determined by identifying where the values in Table 4.1 are on this design curve. The first three permittivites have dimensions that can be fabricated. However, outlined with a vertical dotted line, is the region beyond which the radius would create walls in the unit cell that are smaller than 0.25 mm. These are beyond what can be reliably printed in the Formlab's Form 2 printer. Rohacel 31 HF is instead used for the last layer.

Three samples of each of the materials to be 3D printed are fabricated and tested. Their resulting permittivity as well as a summary of their average is shown in Fig. 4.13. Air is included as a sanity check for the measured values. The plots which show how all 3 samples overlay with each other indicate good repeatability of the process and close agreement with the expected relative permittivity is obtained. With confidence in the fabrication process established the lens shown in Fig. 4.14 is fabricated.

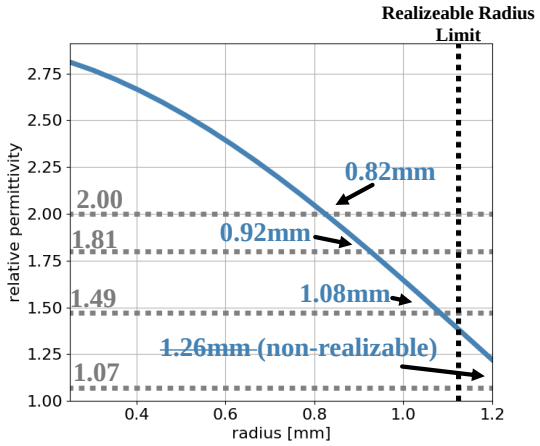

Figure 4.12: Design curve obtained through full wave simulation. Identified are the permittivities from Table 4.1 and the corresponding radius for the holes in their unit cells. The vertical line denotes where the wall thickness would go bellow the 0.25 mm that can be reasonably realized.

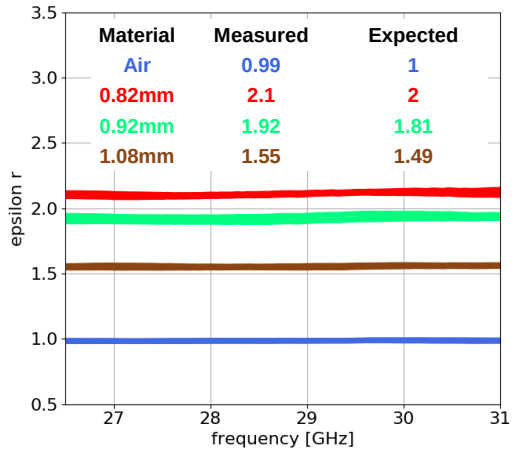

Figure 4.13: Measured material parameters of different samples, identified by the radius of their holes.

4.4 Measured Performance

4.4.1 Far-Field

The measurements of the scanned CP patterns agree very well with the simulation and the results are seen in Fig. 4.15(a). The resulting directivities are a little lower than expected but the

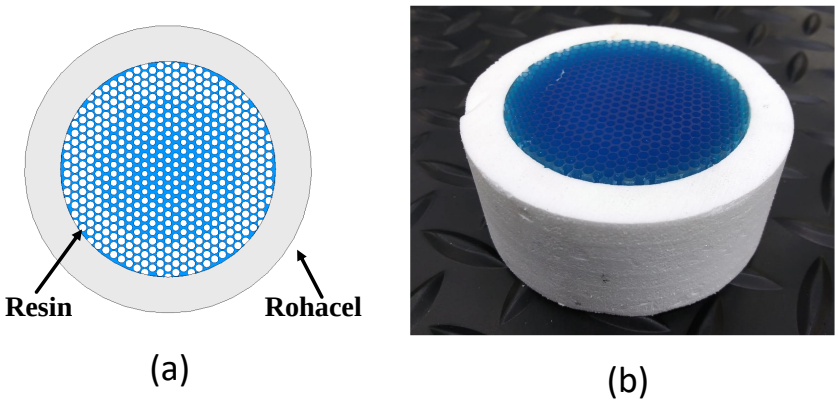

Figure 4.14: (a) CAD model of the lens identifying in blue the parts to be 3D printed with the Tough RS-F2-TOTL-05 Resin and in white the ring to be constructed in Rohacel 31 HF. (b) Picture of the fabricated lens.

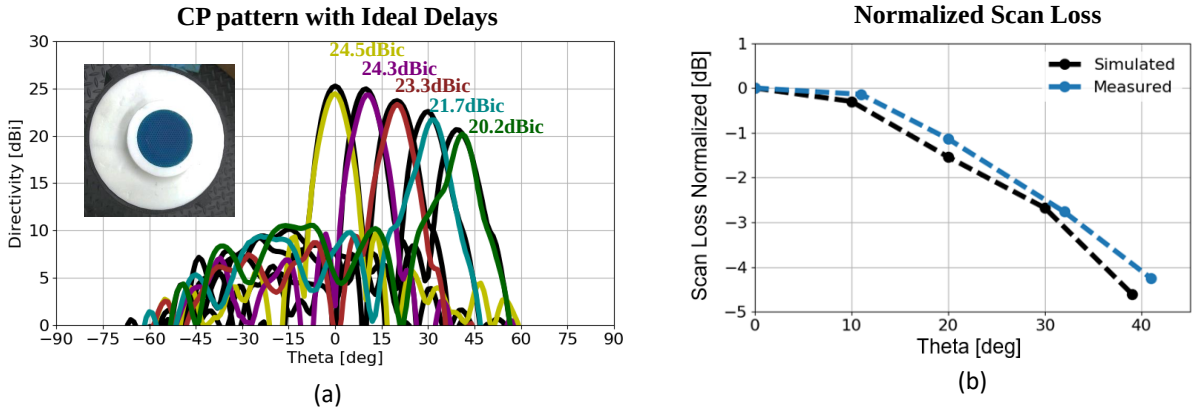

Figure 4.15: (a) Comparison of the measured (colored) and simulated (black) CP directivity patterns. (b) Comparison of the simulated and measured scan loss at the different angles.

scan loss shown in Fig. 4.15(b) tracks very closely with the simulated data. In these patterns the rise in the spillover beam as the lens is inclined is properly captured in both, measurement, and simulation.

There is however an increased cross-polarized component that rises significantly to -15 dB once the beam moves off broadside. This increase in cross polarization is not present in the simulated plots and is attributed to the small anisotropicity of the effective material that is used to

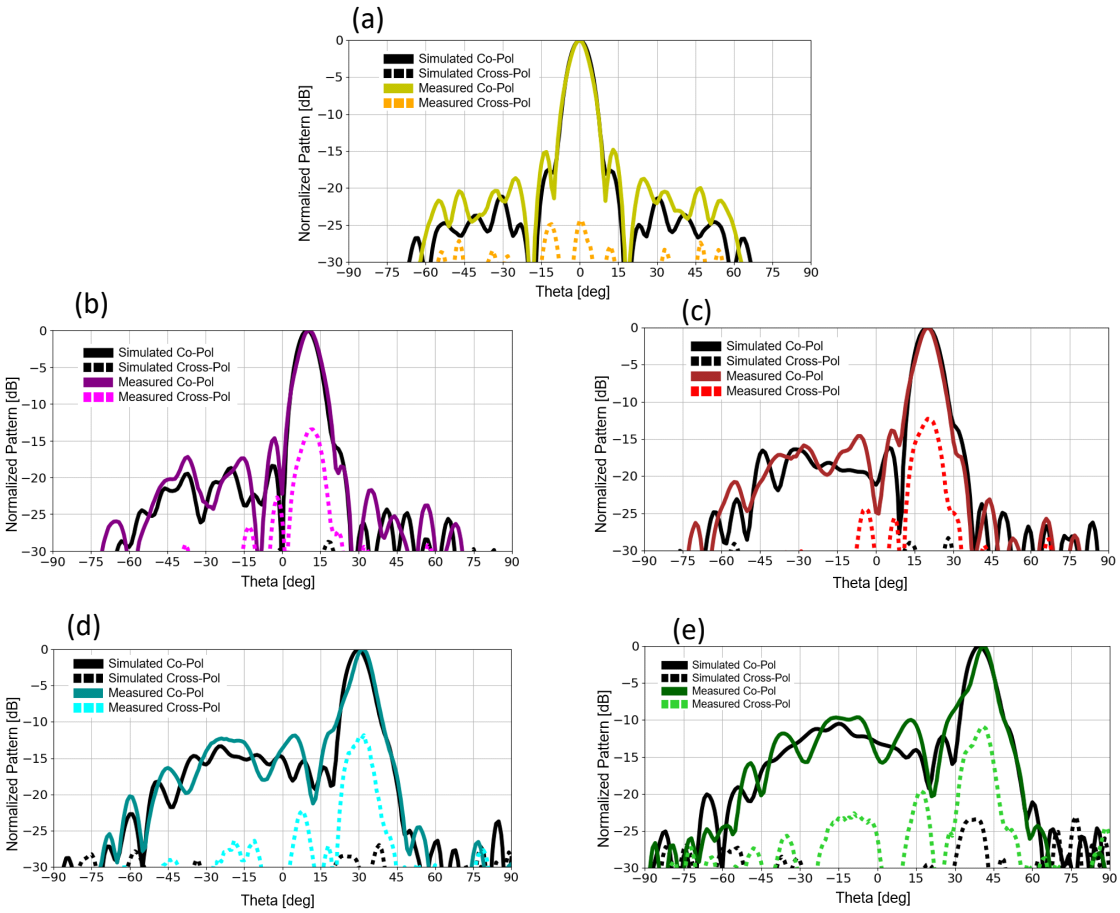

Figure 4.16: Comparison of the measured (colored) and simulated (black) normalized patterns. Cross polarized patterns included with dotted lines. The inclinations shown are (a) 0°, (b) 10°, (c) 20°, (d) 30°, (e) 40°.

fabricated the lens. It is not captured in simulation since all lens simulations are made with fully homogeneous materials. Accurately simulating the perforated lens was found to be impractical due to the memory requirements meshing each perforation would require. As an alternative, with the interest of demonstrating increased cross-polarization of circularly polarized waves when traveling in these materials a quick proof of concept simulation is employed. Using a doubly periodic boundary a unit cell of the material is constructed to simulate an infinite slab as seen in Fig. 4.17(a). No significant difference is observed when looking at the linear components in Fig. 4.17(b) as the rays through the solid and perforated sample behave the same. The effective permittivity of the

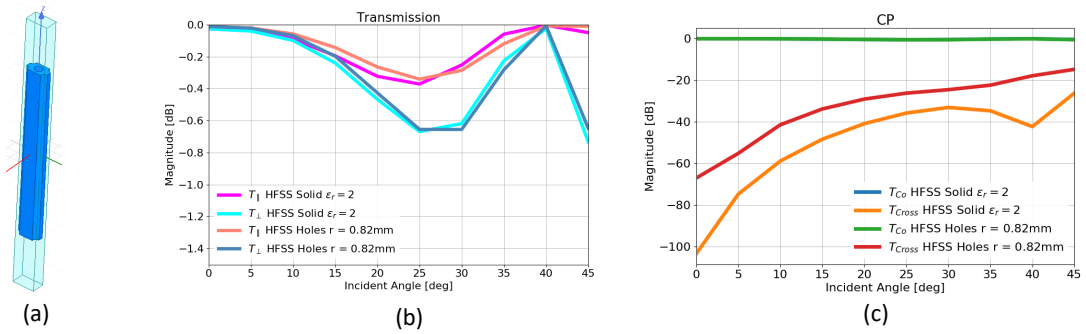

Figure 4.17: (a) Doubly periodic model simulating an infinite slab. The height of the material matches the thickness of the lens, 33.8 mm. (b) Amplitude of the parallel and perpendicular wave components as the incident angle of the wave is modified. (c) Converting the linear components to circular polarization to show that the perforated slab has a higher cross polarization.

perforated sample is the same as the solid sample chosen and it is chosen to be 2. When these components are converted to CP then a difference arises as seen in Fig. 4.17(c). The two co-polarized lines are on top of each other at 0 dB however the cross pols do not agree. The cross polarized component of the perforated slab yields an average of 16.6 dB increase in polarization, demonstrating how the anisotropicity of the material can lead to increased circular cross-polarization.

4.4.2 BC-BFN STAR

To experimentally validate that this scanning has little effect on the Tx/Rx isolation the lens is integrated with the BC-BFN and OMT described in Chapter 2 and is seen in Fig. 4.18(a). In Fig. 4.18(b) the peak coupling is seen to go from -33.6 dB without the lens to -31.7 dB with the lens inclined at 40°. This shows a great insensitivity to the lens's position allowing beam-scanning without degrading the STAR performance. The power dissipated at the BC-BFN's auxiliary load is investigated to ensure that the resilience of the isolation did not come at the cost of efficiency. The power consumed therein remained similarly unaffected at around -14 dB.

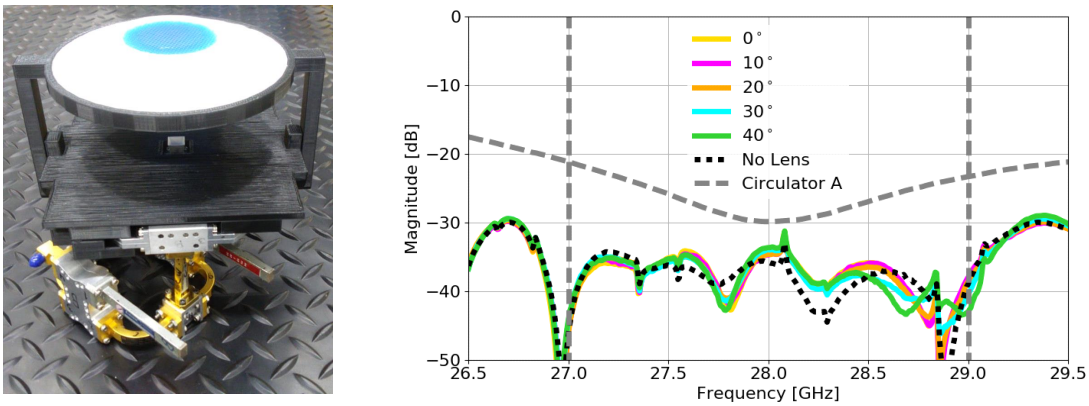

Figure 4.18: (a) Picture of the assembled BC-BFN lens antenna subsystem using the system described in Chapter 2 and (b) measured Tx/Rx coupling at different inclinations

4.5 Conclusions

Beam steering by moving the planar lens on a sphere of constant radius is demonstrated computationally with a scan loss of 4.5 dB at 40° elevation. High system isolation, greater than 43 dB, is maintained in computational models. The system is fabricated using consumer grade 3D printing hardware and tested to demonstrate beam-steerable STAR performance with satisfactory far-field performance. This demonstrates that in cases where the speed of electrical beam switching is less critical, mechanically steering the lens allows for a system with improved far field parameters. Little detriment is measured on the Tx/Rx isolation of the fabricated system from using the lens to mechanically beam steer, specifically, the isolation is degraded by less than 2 dB at the most severe angle. The results in this chapter clearly indicate that mechanically steerable lenses with artificial dielectrics can be used in STAR systems. Impact of intrinsic material inhomogenities on isolation is not significant.

Chapter 5

STAR for Lens Based Retrodirective Systems

5.1 Introduction

Retrodirective (RD) systems that provide enhanced radar cross section (RCS) have long been of interest for airborne, satellite and naval communications as well as wide-angle and wide-bandwidth radar targets. Commercial applications such as RF identification of vehicles and items have been emerging in more recent times as well. RD arrays (RDA) use an array to enhance the RCS in the direction of the received signal. In Van-Atta RDA (VA-RDA) [52–58], retrodirectivity is achieved by interconnecting the elements as shown in Fig. 5.1(a). Passive VA-RDAs can be implemented with transmission lines of equal length to provide equal phase delay between pairs of elements that mirror each other with respect to the center of the array. It is possible to increase the RCS of a VA-RDA further by introducing amplification in the interconnect between elements. Modulation of the singal also allows encoding a response. In that case the RD properties of the array act as self steering for the VA-RDA. Replacing the RD-BFN in Fig. 5.1 for heterodine phase conjugators would also allow achieving retrodirectivity [59] [56]. Due to the non-linear characteristics of their RD-BFN, they are not a focus of the work herein.

Use of completely passive components, such as Luneburg lens reflectors [60–62] provides a simple way to achieve wide-angle and wide-bandwidth retrodirectivity. The Luneberg lens is a spherically symmetric graded index (GRIN) of refraction lens [79]. In general, this lens focuses an incoming plane wave from any given direction onto a focal point on the opposite side of the lens. The set of focal points creates a focal surface in the shape of a sphere, concentric to the lens. The

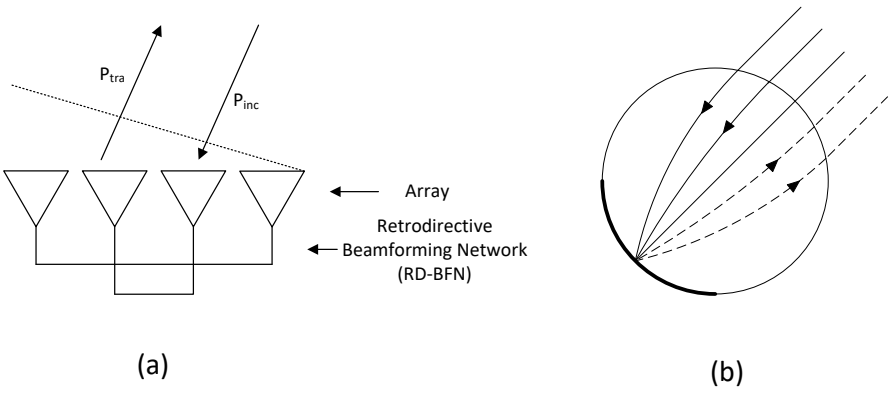

Figure 5.1: (a) 4-element linear Van-Atta RDA showing the interconnects between the array elements that make up the RD-BFN. The interconnects must provide the same phase delay between pairs of elements. (b) Passive Luneburg lens reflector with focal points on its surface. One side of the spherical Luneburg lens is coated with a conductor. The lens focuses the incoming plane waves to this point and reflects all the energy back in the direction of incidence

radius of the focal surface can be greater than, equal to, or less than the radius of the lens itself. By placing reflective material on this focal surface it is possible to create a passive reflector. The schematic for a lens with the focal point at the surface is visible in Fig. 5.1(b). Retrodirectivity is achieved by substituting the reflective materials with antennas having a RD-BFN that connects the receiving antenna to itself. An active RD system using a 2D Luneburg lens was developed in [63] and reported 10dB measured improvement in RCS. Recently [91] the Rotman lens was designed to achieve an active RDA as well.

The effect on RCS due to the BFN (not retrodirective) for an array using series [92] and corporate [93] feed networks has been extensively described. This work has been expanded by [94] who added mutual coupling between antennas to the model by using the element's embedded impedance. The array elements in [94] were not necessarily equal, improving the general applicability of their setup. The formulations in [92–94] provide equations that are explicitly functions of different BFN dimensions but ignore higher order reflections within the BFN. In the case of corporate BFN a suitable truncation depth must be selected for the reflections and coupling coefficients as the array grows. This chapter presents a formulation for the BFN component of the RCS as a function of the

measured S-parameters and the radiation properties of the individual elements, be they arranged in an array, lens manifold, or other grouping of radiating ports. The formulation presented in Section 5.3 includes all higher order reflections and their mutual coupling through the BFN and the antennas.

RD systems endowed with active components that amplify the incoming signal [53–55,57,63, 91] are at risk of entering a positive feedback loop. Feedback loops can be formed from element reflections and element to element coupling, generally simultaneously. [53] makes an estimate for the maximum usable loop gain to be about 20dB for dipole arrays with between -14.7 to -27.8 dB of mutual coupling. [91] reports empirically determining 9dB of amplification before the Rotman configuration, loaded with several reflect-amplifiers, would become unstable. To allow designing systems that work at their utmost, the research herein uses the convergencce criteria of the infinite series of higher order reflections and element couplings to obtain a stability condition and shows algebraic solutions to the maximum usable amplifier gain for various common RD-BFN's.

Antenna reflections are often in the -10 dB to -15 dB range but STAR achieves measured couplings in the -30 dB range or better (see Table 1.2.6). This means that a higher level of amplification can be used, a level that is not available with current bi-directional amplifiers. Utilizing STAR allows using more conventional directional amplifiers with COTS options spanning large bandwidths. A dual-polarized lens feed, such as a horn antenna, integrated with the balanced circulator BFN (BC-BFN) discussed in Chapter 2 receives and transmits using the same polarization, frequency, and aperture. By interconnecting the Tx and Rx ports with a directional amplifier, it is possible then to receive the incoming signal, amplify it, and re-broadcast the same or altered amplified waveform.

This chapter is organized as follows:

- Section 5.2 discusses the RCS formulations from various sources in the literature as they apply to arrays and lens based reflectors.

- Section 5.3 develops a new mathematical framework to express the RCS due to the BFN

network of a multiport system. The calculation of the max-usable loop gain for different retrodirective networks from said equations is also discussed.

- Section 5.4 the equations derived from the previous section are compared to full-wave simulations of the RCS of two dipoles establish their validity.
- Section 5.5 the BC-BFN is used as an exemplar to demonstrate how STAR might be used to enhance the capabilities of an active lens reflector and its performance is compared to passive lens reflectors.
- Section 5.6 provides summary and conclusions on the results obtained in this chapter.

5.2 Theory

5.2.1 Single Antenna RCS

RCS is defined as [95]:

$$\sigma = \lim_{r\to\infty}\left[4\pi r^2 \frac{P_s}{P_{inc}}\right] = \lim_{r\to\infty}\left[4\pi r^2 \frac{|\boldsymbol{E}_s|^2}{|\boldsymbol{E}_{inc}|^2}\right] = \lim_{r\to\infty}\left[4\pi r^2 \frac{|\boldsymbol{H}_s|^2}{|\boldsymbol{H}_{inc}|^2}\right] \tag{5.1}$$

where P_{inc} in the power of an incident plane wave and P_s is the power of the scattered plane wave. The $\boldsymbol{E}$ and $\boldsymbol{H}$ vectors are the electric and magnetic fields with the corresponding subscripts. Following [96, 97] and using the nomenclature from [98] it is possible to separate the antenna RCS, σ, into two components:

$$\sigma = \left|\sqrt{\sigma_{\text{res}}} + \sqrt{\sigma_{\text{ant}}}e^{j\phi_r}\right|^2 \tag{5.2}$$

where σ_{ant} is the RCS due to the antenna mode component which is dependent on how the antenna is loaded and σ_{res} is the residual component, sometimes called the structural component, and it is defined as what is missing from the antenna component to completely represent the RCS. As RCS is a ratio of power incident to power scattered, it does not include phase information. The $e^{j\phi_r}$ term allows representing the phase needed to properly sum the two components. σ_{res} generally has no simple solution but can be determined numerically or experimentally. σ_{ant} however can be fully described for a single antenna using the gain pattern and the load connected to the antenna port.

In [96] Green begins from

$$\boldsymbol{E}_s(Z_L) = \boldsymbol{E}_s(0) - \frac{I(0)}{I_t}\frac{Z_L}{Z_L + Z_a}\boldsymbol{E}_t \tag{5.3}$$

which defines $\boldsymbol{E}_s(Z_L)$ as the electric field scattered by an antenna loaded with a load impedance Z_L. The other terms are: the field scattered by the antenna when it is shorted, $\boldsymbol{E}_s(0)$; the short circuit current produced at the antenna terminals due to an incident wave, $I(0)$; the antenna input impedance, Z_a; and $\boldsymbol{E}_t$ which is the field radiated by the antenna when an input current I_t is applied at the terminals. Green reworks (5.3) to obtain

$$\boldsymbol{E}_s(Z_L) = \boldsymbol{E}_s(Z_a^*) - \frac{I(Z_a^*)}{I_t}\boldsymbol{E}_t\Gamma_m \tag{5.4}$$

which now expresses $\boldsymbol{E}_s(Z_L)$ in terms of the fields scattered by the antenna when it is conjugate matched, $\boldsymbol{E}_s(Z_a^*)$, and the current generated by an incident wave at the antenna ports when the antenna is conjugate matched, $I(Z_a^*)$. In (5.4) Γ_m is a modified reflection coefficient defined as

$$\Gamma_m = \frac{Z_L - Z_a^*}{Z_L + Z_a}. \tag{5.5}$$

Fig. 5.2 graphically identifies where this reflection coefficient is defined compared to the antenna input reflection coefficient. From this expression Green defines the residual/structural RCS from the first term, $\boldsymbol{E}_s(Z_a^*)$. This component would generally have to be experimentally determined. The antenna component is defined from the second term in (5.4) as

$$\sigma_{\text{ant,Green}} = \frac{\lambda^2}{4\pi}G_{\text{inc}}G_{\text{obs}}|\Gamma_m|^2 \tag{5.6}$$

where G_{inc} and G_{obs} are the antenna gain in the direction of incidence and observation. As seen, the antenna component of RCS depends solely on the antenna's radiation patterns as well as the modified reflection coefficient. Tuning the load impedance can be used to modify the properties of σ_{ant}, sometimes to the purpose of canceling the σ_{res} component [98]. Circulators may be used in conjunction with phase shifters, delay lines, or other components to control the properties of σ_{ant} and in [99–101] this approach is used to estimate σ_{ant} and reduce overall RCS.

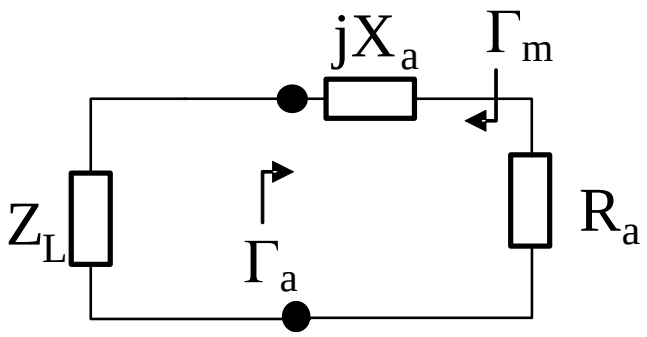

Figure 5.2: Circuit diagram graphically identifying the definition of the antenna reflection coefficient, Γ_a, and Green's modified reflection coefficient Γ_m. The antenna impedance is shown by its real and imaginary parts such that $Z_a = R_a + jX_a$.

Hansen [97] arrives at a similar but distinct set of equations. Using (5.3) as the starting point, Hansen reworks it into

$$\boldsymbol{E}_s(Z_L) = \boldsymbol{E}_s(0) - \frac{1}{2}\frac{I(0)}{I_t}(1+\Gamma_a)\boldsymbol{E}_t \tag{5.7}$$

which bares similarities to (5.4) but using fields and currents with a shorted antenna rather than the terms with a conjugate matched load. From (5.7) Hansen defines

$$\sigma_{\text{Hansen}} = \left|\sqrt{\sigma_{\text{res}}} - (1+\Gamma_a)\sqrt{\sigma_{\text{ant}}}e^{j\phi_r}\right|^2 \tag{5.8}$$

which differs from Green's definition in which the residual/structural component was based on the fields scattered by a conjugate matched load. The second term separates the Γ_a from the σ_{ant} but together they allow for a tuning similar to Green's σ_{ant} term. These differences in definition are found in various sources in the literature and care should be taken to understand which convention is being cited. (5.9) is also derived in [97] and is a counterpart to (5.4) which does away with the conjugate loads and instead uses a matched load. The expression also does away with Γ_m and uses Γ_a instead. Equations (5.4) and (5.9) are equivalent when Z_a is real.

$$\boldsymbol{E}_s(Z_L) = \boldsymbol{E}_s(Z_a) - \frac{I(Z_a)}{I_t}\boldsymbol{E}_t\Gamma_a \tag{5.9}$$

5.2.2 RCS of VA-RDA's

In a VA-RDA, when the antenna elements are well matched to the retro-directive beam forming network (RD-BFN) the expression for σ_{ant} as a function of antenna parameters becomes (5.10) [56, 58]

$$\sigma_{\text{ant,VA-RDA}} = \frac{\lambda^2}{4\pi} G_{\text{inc}} N G_{\text{amp}} G_{\text{obs}} A F_{\text{obs}} \tag{5.10}$$

where G_{inc} is the gain in the direction of wave incidence, G_{obs} is the gain in the direction of observation, N is the number of array elements, G_{amp} is the amplification of the RD-BFN and AF_{obs} is the value of the array factor (AF) in the observed direction. It should be reiterated that this only accounts for the σ_{ant} in (5.2). σ_{res} for a VA-RDA should still be determined computationally or experimentally to account for specular reflections or other forms of scattering from the array and associated structure. This expression ignores any higher order reflections and coupling between array elements. These contributions may be negligible for passive systems ($G_{\text{amp}} \leq 1$) or systems with very little amplification but, as is shown in a later section, the feedback and higher order reflections become more significant with higher levels of amplification.

5.2.3 Series and Corporate Fed Arrays

References [92, 93] use Green's expression as a starting point and present more detailed expressions for the RCS of dipole arrays fed by series and parallel networks respectively. The starting equation is

$$\sigma_{\text{monostatic}} = \frac{4\pi A_e^2}{\lambda^2} \left| \sum_{n=1}^{N} \Gamma_n e^{j\boldsymbol{k}\cdot\boldsymbol{d}_n} \right|^2 |F_{\text{norm}}|^2 \tag{5.11}$$

which relates monostatic RCS to the antenna effective area, A_e; the normalized element scattering pattern, F_{norm}; and the signal reflected from the BFN to each antenna port, Γ_n. The complex exponential in the summation is used to account for the phase delay due to the element's position in the array, $\boldsymbol{d}_n$, and the wave-vector along which the observation is being made, $\boldsymbol{k}$. Γ_n is further defined for series and corporate feed networks in terms of the properties of the sub-components and the entire formulation is subject to various assumptions:

1) Devices of the same type are assumed to have identical electrical characteristics. All the radiating elements have the same reflection and transmission coefficients.

2) The feed devices are well matched and therefore higher order reflections can be neglected.

3) Lossless devices in the BFN are assumed.

When defining the Γ_n for the corporate feed networks a truncation level must be selected beyond which the reflections in the BFN are assumed negligible. Reference [94] relaxes the 1st requirement and expands the definition of the Γ_n terms to include information about the embedded array element. Specifically, the shape of the array elements is allowed to vary, modifying their impedance and the effect of the active impedance is examined.

5.2.4 Luneburg Lens Reflectors

The monostatic RCS of an ideal passive Luneburg lens reflector is described fully as a function of its radius, R_{LL} [61, 62]

$$\sigma_{\text{mono,LL Reflector}} = \frac{4\pi(\pi R_{LL}^2)^2}{\lambda^2}. \tag{5.12}$$

which is the same expression as a round PEC plate. The lens reflector will maintain this performance over the angle that is coated with the reflective surface. If the reflector is replaced by an antenna manifold then an expression similar to (5.10) is obtained

$$\sigma_{\text{ant,LL Antenna}} = \frac{\lambda^2}{4\pi} G_{\text{inc}} G_{\text{amp}} G_{\text{obs}} \tag{5.13}$$

with $N = 1$. This is under the assumption that only one antenna is active which is good provided teh entire manifold is well designed.

5.3 BFN Feedback Model

The common assumption of the hitherto discussed models is that feedback is negligible and the BFN is assumed to provide simple amplification. [92, 93] present expressions that include some feedback within the BFN, however, their analysis is limited to series and corporate BFN for arrays.

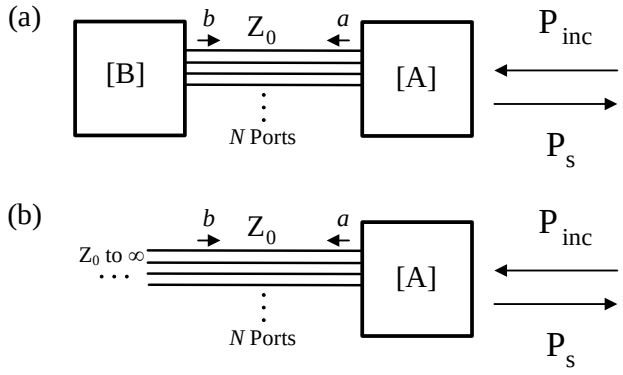

Figure 5.3: Schematic diagram showing (a) antenna and BFN and (b) replacing the RD-BFN for the set of equivalent impressed sources $\boldsymbol{b}$ on infinite transmission lines of characteristic impedance Z_0

Furthermore a finite truncation level must be chosen. The analysis that follows herein will present a framework for determining the σ_{ant} with an arbitrary BFN.

The limits between the antenna and BFN can be delimited at any convenient set of ports. This will result in two subsystems with scattering matrices $[A]$ and $[B]$ respectively as shown in Fig. 5.3. Both matrices are assumed referenced to a real impedance Z_0 at all ports. For the model herein discussed, the portion labeled as the antenna should have radiated fields associated with each port. The field scattered by the full system due to an incident wave, is described as

$$\boldsymbol{E}_s = \boldsymbol{E}_s(Z_0) + \boldsymbol{E}_s(\text{BFN}). \tag{5.14}$$

The terms to the right are more conceptual than strict functions and $\boldsymbol{E}_s(Z_0)$ represents the scattered field when the antenna ports are loaded with the impedance Z_0 and $\boldsymbol{E}_s(\text{BFN})$ represents the fields generated by the presence of the BFN. The physical reasoning behind this separation can be understood through Huygen's equivalent wave sources [102] which allow replacing the BFN in Fig. 5.3(a) for infinite transmission lines and a set of impressed wave sources $\boldsymbol{b}$. The resulting far-field is then a superposition of the field generated by the impressed wave sources, $\boldsymbol{E}_s(\text{BFN})$, and the field scattered by the antenna loaded by the semi-infinite lines, $\boldsymbol{E}_s(Z_0)$. Converting (5.14) to RCS

while keeping the same labels yields

$$\sigma = \left| \sqrt{\sigma_{Z_0}} + \sqrt{\sigma_{\text{BFN}}} e^{j\phi_r} \right|^2 \tag{5.15}$$

where σ_{Z_0} is the RCS of the system with all ports terminated with the reference impedance. If Z_0 is chosen to be realizable, it is possible to obtain this value through empirical studies or numerical simulations. σ_{BFN} is the component of the RCS due to the presence of the BFN. Both these components are generally out of phase with each other by some unknown phase ϕ_r.

The following section describes a closed form solution for σ_{BFN} in terms of radiation patterns and scattering parameter matrices. The formulation herein described makes no assumptions as to their spatial orientation or about how they are connected, if they are connected, within their respective BFN's. Specific BFN's relevant to RD systems are discussed in the later subsections to illustrate how the model indicates the limit of the system's RCS enhancement.

5.3.1 BFN RCS Component

The power received by a single antenna can be described by the equation

$$P_{\text{rec}}^{(n)} = P_{\text{inc}} \frac{\lambda^2}{4\pi} G_{\text{inc}}^{(n)} \tag{5.16}$$

where $P_{\text{rec}}^{(n)}$ is the power received by the n-th antenna with gain $G_{\text{inc}}^{(n)}$ in the direction of incidence [103] and from which a wave amplitude vector [104] $\boldsymbol{a_0}$ can be defined with elements

$$a_0^{(n)} = \sqrt{G_{\text{inc}}^{(n)}} \frac{E_{\text{inc}}^{(n)}}{|E_{\text{inc}}^{(n)}|} = g_{\text{inc}}^{(n)} \tag{5.17}$$

where $a_0^{(n)}$ represents the excitation from an incoming wave at port n. Compared to the usual definition of a wave vector, $a_0^{(n)}$ is normalized by a $\sqrt{P_{\text{inc}} \frac{\lambda^2}{4\pi}}$ factor such that

$$\left| \sqrt{P_{\text{inc}} \frac{\lambda^2}{4\pi}} a_0^{(n)} \right|^2 = P_{\text{rec}}^{(n)} = P_{\text{inc}} \frac{\lambda^2}{4\pi} G_{\text{inc}}^{(n)} \tag{5.18}$$

The definition of $g_{\text{inc}}^{(n)}$ in (5.17) allows succinctly accounting for the phase of the electric field pattern in the direction of incidence, E_{inc}. This phase information is necessary for the proper combination

of the radiation from all ports. The BFN's response to the $\boldsymbol{a_0}$ excitation is found as $\boldsymbol{b_0} = [B]\boldsymbol{a_0}$. This $\boldsymbol{b_0}$ in turn excites the antenna. A well designed antenna would radiate most of the energy but there will generally be some level of reflection and mutual coupling between the antennas. This creates a new set of wave vectors coming from the antenna, $\boldsymbol{a_1} = [A]\boldsymbol{b_0}$. The cycle then repeats itself and the recursive relationship

$$\boldsymbol{b_i} = [B]\boldsymbol{a_i} \tag{5.19a}$$

$$\boldsymbol{a_{i+1}} = [A]\boldsymbol{b_i} \tag{5.19b}$$

is defined which uses $\boldsymbol{a_0}$ as the initial case. $\boldsymbol{b}$, identified in Fig. 5.3, is defined as the sum of all the wave vectors incident on the antenna ports. The infinite series has a well known algebraic expression [105] that allows writing $\boldsymbol{b}$ as a function of $\boldsymbol{a_0}$. The derivation is as follows:

$$\begin{aligned}
\boldsymbol{b} &= \sum_{i=0}^{\infty} \boldsymbol{b_i} \\
&= \boldsymbol{b_0} + \boldsymbol{b_1} + \boldsymbol{b_2} + ... \\
&= [B]\boldsymbol{a_0} + [B]\boldsymbol{a_1} + [B]\boldsymbol{a_2} + ... \\
&= [B]\boldsymbol{a_0} + [B][A]\boldsymbol{b_0} + [B][A]\boldsymbol{b_1} + ... \\
&= [B]\boldsymbol{a_0} + [B][A][B]\boldsymbol{a_0} + [B][A][B][A][B]\boldsymbol{a_0} + ... \\
&= [B]\left([I] + [A][B] + ([A][B])^2 + ...\right)\boldsymbol{a_0} \\
\boldsymbol{b} &= [B]\left(\sum_{i=0}^{\infty}([A][B])^i\right)\boldsymbol{a_0} \\
\boldsymbol{b} &= [B]\left([I] - [A][B]\right)^{-1}\boldsymbol{a_0}
\end{aligned} \tag{5.20}$$

where $[I]$ is the identity matrix, and the -1 exponent expresses the matrix inversion of the expression within parenthesis. The resulting power scattered from an antenna excited by $\boldsymbol{b}$ is given by

$$P_s = P_{\text{inc}}\frac{\lambda^2}{16\pi^2 r^2}\left|\sum_{n=1}^{N} b^{(n)} g_{\text{obs}}^{(n)}\right|^2. \tag{5.21}$$

and when (5.21) is placed into (5.1) an expression for the $\sigma_{\text{RD-BFN}}$ is obtained as

$$\sigma_{\text{BFN}} = \frac{\lambda^2}{4\pi} \left| \sum_{n=1}^{N} b^{(n)} g_{\text{obs}}^{(n)} \right|^2 . \tag{5.22}$$

which expresses the σ_{BFN} solely in terms of antenna patterns and measurable network quantities. This expression bares significant similarities to (5.11), however, the definition of the Γ_n focused on features in the series or corporate BFN. The $b^{(n)}$ are defined in terms of the network parameters of both, the antenna and the BFN. These parameters can be obtained analytically or numerically and the expression would remain applicable. The elements could be all equal or all different, lossy or perfectly conducting. There is also no truncation of the series so all higher order reflections are accurately captured.

When using a reflect amplifier with a single antenna, such as when a single antenna is used with a Luneburg lens, $[B]$ and $[A]$ are scalar quantities. $[B] = g_{\text{amp}}$ and $[A] = \Gamma_a$, where g_{amp} is defined such that $|g_{\text{amp}}|^2 = G_{\text{amp}}$ and Γ_a is the reflection coefficient looking into the antenna. This allows substituting in (5.22) to obtain

$$\sigma_{\text{BFN}} = \frac{\lambda^2}{4\pi} \left| \frac{g_{\text{amp}}}{1 - \Gamma_a g_{\text{amp}}} \right|^2 G_{\text{inc}} G_{\text{obs}}. \tag{5.23}$$

Contrasting (5.10), (5.13), and (5.23), the expression for the RCS of the system becomes less linear as a function of amplifier gain as the antenna reflections become more significant. This behavior is not accounted for in the previous expressions.

5.3.2 Convergence

Much like the geometric series, (5.20) is a valid solution to the infinite series but subject to a convergence criteria. This value is known as the spectral radius, ρ, defined in [105] as

$$\rho\left([A][B]\right) = |e_{\max}| \tag{5.24a}$$

$$\det\left([I]e - [A][B]\right) = 0 \tag{5.24b}$$

where $|e_{\max}|$ is the largest magnitude of the set of eigenvalues that are solutions to (5.24b) and det() is the determinant of a matrix. In order for (5.20) to converge, the spectral radius of $[A][B]$

must be below unity, i.e.:

$$\rho\left([A][B]\right) = |e_{\max}| < 1. \tag{5.25}$$

If the spectral radius is greater than or equal to 1 then the sums of the $\boldsymbol{a_i}$ and $\boldsymbol{b_i}$ vectors never converge to a finite value. In systems with amplifiers this would lead to the energy of the system increasing until the amplifier is saturated. Once the linearity of $[A]$ or $[B]$ is compromised, the recursive relationships in (5.19) would no longer hold and the derivation in (5.20) would no longer be valid. The RCS may still converge to a finite value but non-linear behavior is beyond the scope of the herein presented expressions.

5.3.3 Retrodirective Beam Forming Networks

The convergence criteria (5.24b) can be evaluated from measured S-parameters for any kind of BFN. However, when designing an active RD system it is of interest to know when instability or non-linear effects start to interfere. Fortunately, many common RD-BFN's allow for an algebraic solution to (5.24b) for stability as a function of some parameter. The examples herein will focus on the amplifier's gain.

A RD-BFN network's S-parameter matrix can, by convenient labeling of the ports so that related ports are contiguous, be described as a block-diagonal matrix

$$[B] = \begin{bmatrix} [B_{\mathrm{s}}] & [\,0\,] & \dots & [\,0\,] \\ [\,0\,] & [B_{\mathrm{s}}] & \ddots & \vdots \\ \vdots & \ddots & \ddots & [\,0\,] \\ [\,0\,] & \dots & [\,0\,] & [B_{\mathrm{s}}] \end{bmatrix}. \tag{5.26}$$

The sub-networks $[B_s]$ may have any number of ports depending on how retrodirectivity is being achieved. Some examples are:

$$[B_s] = \begin{bmatrix} 0 & g_{\mathrm{amp}} \\ g_{\mathrm{amp}} & 0 \end{bmatrix} \tag{5.27a}$$

$$[B_s] = \begin{bmatrix} 0 & 0 \\ g_{\text{amp}} & 0 \end{bmatrix} \tag{5.27b}$$

$$[B_s] = g_{\text{amp}} \tag{5.27c}$$

where $20\log_{10}(g_{\text{amp}})$ is some amplifier's gain in dB. In (5.27), the first two subnetworks are two port networks, which would be commonly useful in VA-RDAs. The (5.27a) is the bidirectional amplifier and (5.27b) is the directional amplifier. In (5.27c) $[B_s]$ is a scalar quantity suitable to describe the RD-BFN using reflect amplifiers used with lenses in [63, 91].

Inspecting (5.26) and (5.27) it is evident that the scalar g_{amp} can be factored out such that

$$[B] = [B']g_{\text{amp}} \tag{5.28}$$

and defining

$$e = e'g_{\text{amp}} \tag{5.29}$$

allows rewriting the eigenvalue problem from (5.24b) as

$$\det\left([I]e' - [A][B']\right) = 0 \tag{5.30}$$

which has the advantage that it is independent of the quantity g_{amp}. Then through (5.29) the stability condition in (5.25) is rewritten as

$$|e_{\max}| = |e'_{\max}g_{\text{amp}}| < 1 \tag{5.31}$$

from where it follows that the series converge as long as

$$|g_{\text{amp}}| < \frac{1}{|e'_{\max}|} \tag{5.32}$$

This expressions defines the maximum gain that can be applied into the system before the feedback renders it unstable. This is the maximum loop gain and is expressed in dB as

$$G_{\max} = 20\log_{10}\left(\frac{1}{|e'_{\max}|}\right) \tag{5.33}$$

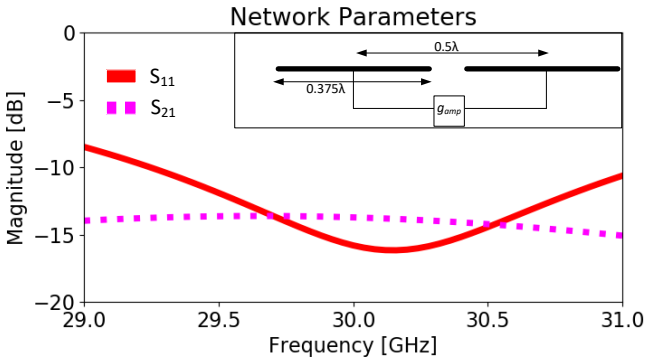

Figure 5.4: Network parameters for the 2 dipole array shown in the inset.

5.4 Numerical Results

In order to test the hitherto derived equations, a simple set of dipoles is used. The geometry, shown in the inset of Fig. 5.4, is 2 dipoles connected to an ideal bi-directional amplifier (network described by (5.27a)). These problems are simulated using Altair's FEKO v2019.2 which allows exciting the system with an incident plane wave and integrating the full-wave simulation with a linear circuit model of the RD-BFN. The individual dipoles are tuned to resonate at a frequency of 30GHz and placed along each other's radiation null, separated by half a wavelength. The resulting network parameters can be seen in Fig. 5.4. Though the antennas are well matched bellow -10 dB, the reflection coefficient is non-zero. The dipoles are also not perfectly isolated from each other.

The monostatic RCS as a function of amplifier gain for the 2-dipole configuration is shown in Fig. 5.5. The dashed line is the ideal case which ignores any kind of feedback and follows (5.10). The full-wave simulation clearly does not follow this simple line. It increases suddenly as $G_{\text{amp}} \to G_{\text{max}}$. (5.22) is shown in blue and it agrees very well with the full-wave result, matching the deviations from the simple equation. The max usable loop gain is significantly lower than individual reflections or coupling which are independently cited in previous works as the maximum limit. The value can be easily obtained numerically solving the eigenvalue problem of (5.30) since the simplicity of this

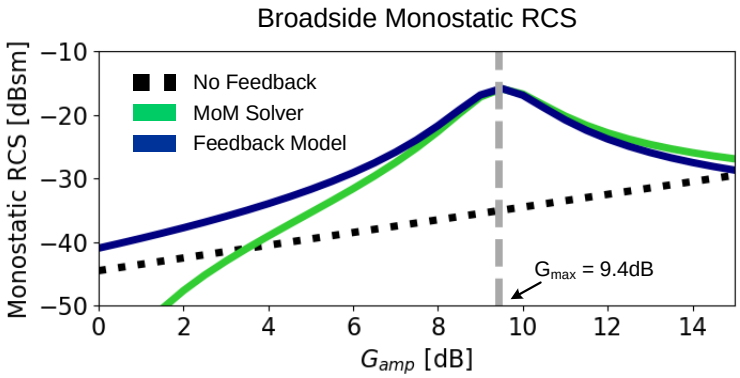

Figure 5.5: Monostatic RCS for the 2-dipole configuration shown in Fig. 5.4 at broadside and a frequency of 30GHz

example allows algebraically expressing the solution in dB as

$$G_{\max} = \min\left\{-20\log\left(|S_{21} \pm S_{11}|\right)\right\} \tag{5.34}$$

where S_{11} and S_{21} are the reflection coefficient and port coupling of a symmetric and reciprocal two port antenna network. This equation makes it clear that the feedback stability is limited due to the combination of both the reflection and coupling.

5.5 STAR Active Lens Retroreflector

5.5.1 Balanced Circulator BFN

When separating the Tx and Rx ports in a STAR antenna subsystem it makes intuitive sense to use a circulator as their ideal behaviour readily translates into 3 ports; Tx port, antenna port, and Rx port. Antennas, however well designed, often have reflections in the range of -10 to -15 dB over their operating bandwidth. In a retro-directive system using the single circulator shown in Fig. 5.6, the incident power arrives as the Rx signal, go through the amplifier, and is re-transmitted. However the Tx signal is reflected with the Γ_a reflection coefficient and feed back into the Rx path, then amplified, and back in the loop. From the discussion above it is readily found that $G_{\max} = -20\log\Gamma_a$. It should be noted that this assumes a circulator with infinite isolation. If the coupling between the circulator's "isolated" ports is added as B then the expression for the max

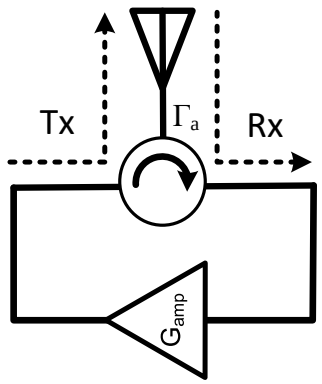

Figure 5.6: Single circulator with amplifier connecting the Rx and Tx.

usable loop gain becomes:

$$G_{\max} = -20 \log \left(|\Gamma_a + B| \right). \tag{5.35}$$

Having these two values cancel out is not the focus within this writing but recent work such as [71] has devised ways to tune the antenna reflections and circulator leakage to achieve a high level of self interference cancellation in a narrow band. This method would require designing the system such that B and Γ_a have comparable amplitudes and are phased to interfere destructively. While it is possible to do so in a narrow band, a wider bandwidth system will generally see these two interact in and out of phase at different frequencies.

The BC-BFN (discussed in Chapter 2) is designed to completely remove both the antenna reflections and the circulator leakage. A signal received goes from the Rx port, through the amplifier and to the Tx side where it is introduced into the BC-BFN which re-radiates it. The BC-BFN has a leakage from the Tx to the Rx port described by (2.15).

The added complexity of the BC-BFN is justified when the max usable loop gain is calculated. Populating (5.30) with $[A]$ being the S-parameters looking into the Tx and Rx ports in Fig. 5.7 and $[B]$ an ideal unidirectional amplifier, such as in (5.27b) results in

$$\det \left([I]e' - \begin{bmatrix} S_{\mathrm{Tx,Tx}} & S_{\mathrm{Tx,Rx}} \\ S_{\mathrm{Rx,Tx}} & S_{\mathrm{Rx,Rx}} \end{bmatrix} \begin{bmatrix} 0 & 1 \\ 0 & 0 \end{bmatrix} \right) = 0 \tag{5.36}$$

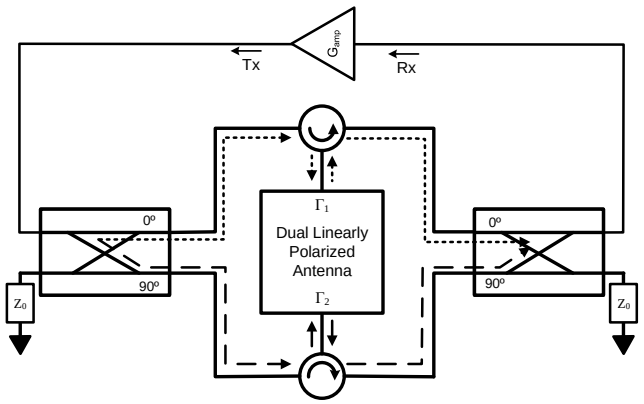

Figure 5.7: Balanced circulator BFN showing the amplifier connecting the Rx and the Tx.

where $S_{\mathrm{Tx,Tx}}$ and $S_{\mathrm{Rx,Rx}}$ are the reflection coefficients at the Tx and Rx ports respectively. $S_{\mathrm{Rx,Tx}}$ is described in (2.15) and $S_{\mathrm{Tx,Rx}}$ is the coupling in the reverse direction which is different due to the non-reciprocal nature of the system. Solving for e' yields the eigenvalues $e' = 0,\ S_{\mathrm{Rx,Tx}}$ and subsequently through (5.33) it is obtained that, in dB,

$$G_{\max} = -20\log\left(S_{\mathrm{Rx,Tx}}\right) \tag{5.37}$$

which shows that the max usable loop gain is independent of $S_{\mathrm{Tx,Tx}}$, $S_{\mathrm{Rx,Rx}}$, or $S_{\mathrm{Tx,Rx}}$. Furthermore, when compared to the expression for the single circulator max loop gain, it is seen that rather than being limited by the magnitude of the reflection coefficients and circulator leakage it is limited by how symmetrical the reflections and overall system can be made to be.

5.5.2 Lens Antenna and BC-BFN

In order to evaluate the concept, measured data from the lens antenna discussed in Chapter 3 is used as an example. Their measured isolation is included in Fig. 5.8. With an amplifier that is independent of frequency, the minima in Fig. 5.8 become the upper bound for the amplifiers gain. For contrast, the measurement using only one circulator and the isolation of the COTS circulators by itself are included to show the improvement provided by the BC-BFN.

It is important to note that the RCS response will not be linear with G_{amp} up to $G_{\mathrm{amp}} = G_{\max}$.

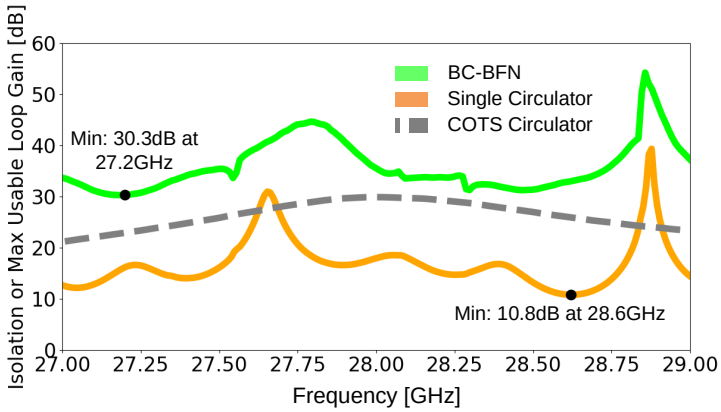

Figure 5.8: Isolation, equal to Max usable gain for the single circulator and balanced circulator networks. The nominal isolation for the COTS circulators employed is included for reference. The balanced circulator clearly out-performs the single circulator and even the COTS component.

Solving (5.20) for the present case yields a scalar expression relating the incident and transmitted signals as

$$b = \frac{g_{\text{amp}}}{1 - S_{\text{Rx,Tx}} g_{\text{amp}}} a_0 \tag{5.38}$$

which when converted to dB is clearly not linearly proportional to G_{amp}. The expression has a singularity at $g_{\text{amp}} = \frac{1}{S_{\text{Rx,Tx}}}$, and this is related to the stability condition mentioned above. This singularity increases very rapidly as $g_{\text{amp}} \to \frac{1}{S_{\text{Rx,Tx}}}$. Care should be taken in the relative phase of the two quantities as this would lead to compression and non-linearity of a real amplifier at a much lower amplification level than the above analysis would indicate. The contours that illustrate this point are shown as a function of a normalized g_{amp} in Fig. 5.9. The value of g_{amp} has been normalized by a $\frac{1}{S_{\text{Rx,Tx}}}$ factor such that the normalized value $\hat{g}_{\text{amp}} = g_{\text{amp}} S_{\text{Rx,Tx}}$. This normalization maps the contours to within the unit circle and places the singularity at 1. Due to the g_{amp} in the numerator of (5.38) the amplitude of the function is also scaled by the same factor.

The lens antenna has a measured directivity between 24.5 dBic and 25.1 dBic [32]. The measured directivity is sufficient to evaluate (5.10). The result of said equation is shown in Fig. 5.10. Without the feedback the response in frequency is steady, and follows the response of the pattern. Once feedback is included, the result is seen to vary more as a function of frequency.

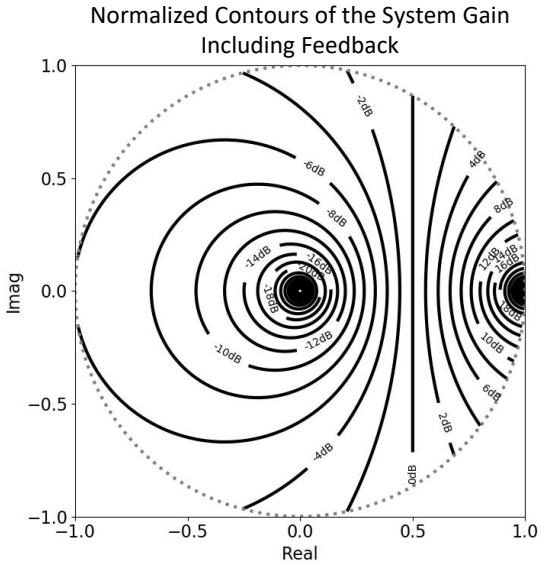

Figure 5.9: The gain of (5.38) as a function of g_{amp} normalized by a $\frac{1}{S_{\text{Rx,Tx}}}$ factor. The amplitude, shown in dB, is also normalized by said factor. Due to the renormalization the singularity is located at 1 and the spectral radius is confined to the unit circle.

This variation is due to the variability of the Tx/Rx coupling as a function of frequency. In the frequencies studied, variability of up to 10 dB is observed in the response when including feedback and utilizing $G_{\text{amp}} = 30$ dB. The simple model with no feedback does not predict this behavior which is significant when estimating the quality of the signal returned by the system. The monostatic RCS of the theoretical reflector is surpassed by 20 dB or more at the studied frequencies. Fig. 5.11 shows the monostatic RCS at different incident angles for select frequencies. In contrast with the theoretical reflector which has a flat response, the pattern for the system with the RD-BFN follows the shape of the antenna pattern at different angles. Future systems can achieve coverage over comparable angles by combining multiple horns in a manifold around the lens.

5.6 Conclusion

The application of STAR techniques to retrodirective systems is explored. A mathematical framework to establish the theoretical limits of the enhancement these systems can provide is developed and compared to previous equations found in the open literature. It is found that a

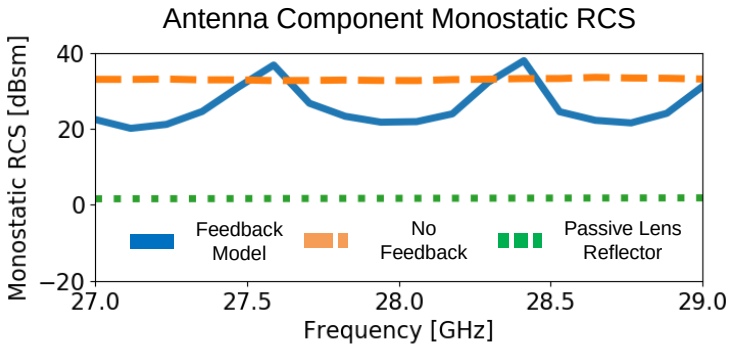

Figure 5.10: Monostatic RCS at broadside from measured data as predicted by equations with feedback (5.20) and without (5.10). $G_{\text{amp}} = 30$ dB for both. They are compared to the passive lens reflector whose MRCS is described by (5.12).

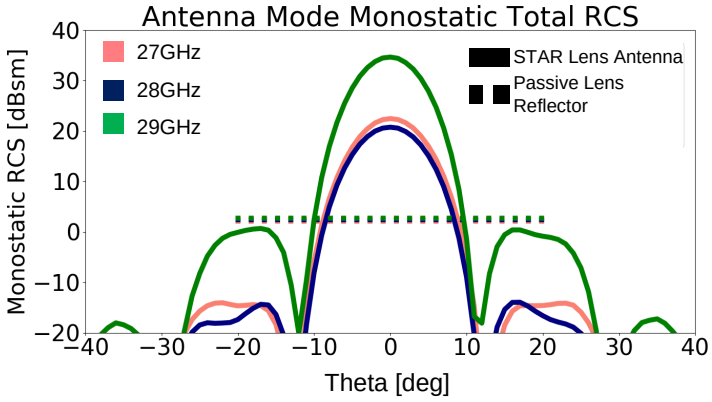

Figure 5.11: Antenna component of the monostatic RCS for the lens based STAR system. The dotted lines are the expected response from (5.12) where the passive lens reflector spans ±25°.

combination of both the mismatch and the element to element coupling limits the possible gain of the system. The new equation allows predicting the antenna component of the RCS for systems with an arbitrary number of antenna ports, example systems being arrays or lens manifolds. The balanced circulator beam forming network is used as an exemplar for how a STAR system would reduce feedback and improve the performance of the subsystem. Data from a measured lens based STAR system is used to run the model and readily show 20 dB of enhancement when compared to the passive lens reflector counterpart. These results clearly show that the STAR techniques can be used to enhance and control the RCS of the target. Equally as important, the processing of the

retrodirected waveforms, while enhancing the range of the system is also enabled. All this is done at the same polarization, thus preserving the scarce spectrum resources.

Chapter 6

Conclusion

6.1 Summary

Full duplex antenna systems of interest for current and future millimeter wave applications are demonstrated in this thesis. Theoretical and experimental framework was developed around waveguide-based technologies and highly directive lens-based antennas and retrodirective apertures. Impact of actual imperfections arising from manufacturing and material imperfections is studied. Novel designs are developed to probe the theory and applications of the different antenna systems.

The coupling paths in an ideal balanced circulator beam forming network (BC-BFN) network have been studied and the term representing imperfect port-to-port isolation in the antenna has been introduced. In order to achieve a dual-polarized waveguide based system with STAR, the class 3 orthomode transducer (OMT) is chosen to connect the antenna and the BC-BFN. Its turnstile junction allows for maintaining symmetry between both polarizations while providing high isolation therefore making this topology an ideal candidate for STAR. The importance of the routing of the lines to the ports has been demonstrated to limit the isolation that can be expected of these systems. A design that routes the lines in such a way that not only the transmitted, but also the reflected signal maintains symmetry has been presented and shown to yield very high isolation in simulation. The system was built and tested to demonstrate that this OMT provides better isolation when integrated with the BC-BFN. Average increase in isolation over the single circulator of 13 dB is obtained.

Impact of mechanical beam steering on isolation of STAR antenna system was also investi-

gated. A planar lens was moved on a sphere of constant radius and over 43 dB of isolation with a scan loss of 4.5 dB at 40° elevation is demonstrated. The system is fabricated using consumer grade 3D printing hardware and tested to demonstrate beam-steerable STAR performance with satisfactory far-field performance. This demonstrates that in cases where the speed of electrical beam switching is less critical, mechanically steering the lens allows for a system with reasonable Tx/Rx isolation and improved far field parameters. Little detriment is measured on the Tx/Rx isolation of the fabricated system from using the lens to mechanically beam steer, specifically, the isolation is degraded by less than 2 dB at the most severe angle. These results clearly indicate that mechanically steerable lenses with artificial dielectrics can be used in STAR systems. Impact of intrinsic material inhomogenities on isolation is not significant.

The application of STAR techniques to enhance the performance of retrodirective systems is also explored. A mathematical framework to establish the theoretical limits of the enhancement these systems can provide is developed and compared to previous equations from the open literature. It is found that a combination of both, the mismatch, and the element to element coupling limits the achievable gain of the system. The new equation predicts the antenna component of the RCS for systems with an arbitrary number of antenna ports, example systems being arrays or lens manifolds. The BC-BFN is used as an exemplar for how a STAR system would reduce feedback and improve the performance of the subsystem. Data from the measured lens based STAR system is used to run the model and readily show 20 dB of enhancement when compared to the passive lens reflector counterpart. These results clearly show that the STAR techniques can be used to enhance and control the RCS of the target. Equally as important, the processing of the retrodirected waveforms, while enhancing the range of the system is also enabled. All this is done at the same polarization, thus preserving the scarce spectrum resources.

This thesis has demonstrated a path for using highly directive millimeter-wave antenna systems in full-duplex applications. It is shown that geometrical, material, and assembly imperfections, while clearly noticeable at these wavelengths, do not detrimentally preclude these heterogeneous antennas for these needs.

6.2 Contributions

The contributions in this thesis are summarized as:

- Impact of asymmetries in an OMT on the limit BC-BFN isolation is studied and relevant conclusions are presented.
- A TE waveguide OMT design with theoretically infinite isolation in the entire band with BC-BFNs has been demonstrated.
- Demonstrated that asymmetries in the lens positioning do not significantly impact BC-BFN isolation
- Fabricated a spherical lens based high directivity STAR system to experimentally verify theoretical findings.
- Experimentally demonstrated that the asymmetry of the ground plane does not significantly deteriorate the self interference cancellation (SIC) in the half lens STAR system.
- Achieved beam-steerable STAR that covers an equatorial angular sector of a sphere.
- Beam steering by moving the planar lens on a sphere of constant radius is demonstrated with a scan loss of 4.5 dB at 40° elevation.
- Demonstrated high system isolation was maintained with the aforementioned field of view.
- Experimentally demonstrated beam-steerable STAR in a conical field of view.
- Derived closed form expression for the RCS due to the BFN from network parameters and antenna element patterns.
- Derived exact algebraic solution for maximum loop gain in various retrodirective systems.
- Demonstrate benefit of integrating STAR subsystems to augment lens based retrodirective systems and further increase co-polarized monostatic RCS.

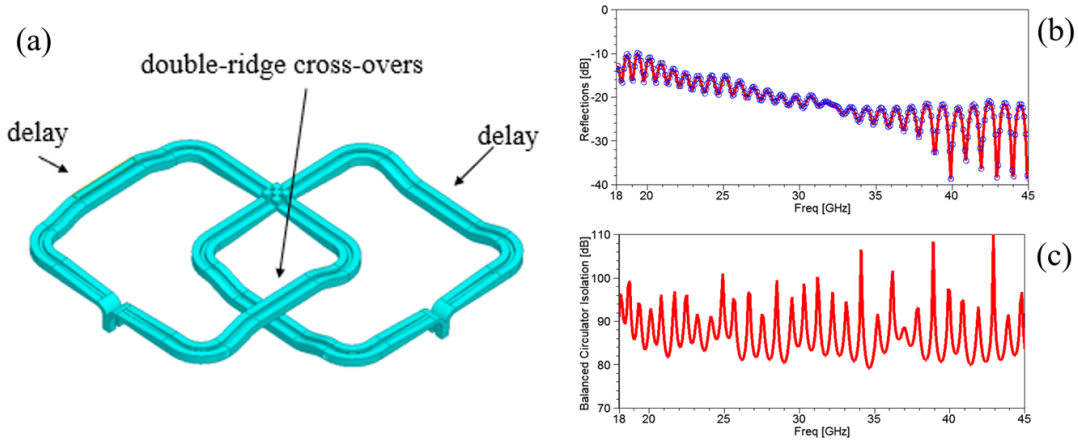

Figure 6.1: (a) Turnstile junction based OMT using ridged waveguide to cover the 18-45GHz band. (b) Magnitude of the reflection coefficients. Both plots lie on top of each other resulting in (c) which shows Tx/Rx isolation better than 80 dB in simulation.

6.3 Future Work

The work presented in this thesis can be expanded in various directions, some of which are briefly discussed below:

6.3.1 OMT and BC-BFN Enhancements

The combined OMT and BC-BFN implemented in WR28 are limited in bandwidth by the choice of circulators. The symmetric OMT design also works with waveguide designs that cover beyond an octave of bandwidth. Fig. 6.1 shows the model and results for an OMT designed to cover 18-45 GHz. The dual ridge cross section is developed in [16]. Accurate machining of the ridges is critical in this design. Coupled with similar waveguide components in the BC-BFN, this leads into the possiblity of a very wide bandwidth and high power full-duplex subsystem.

The circulators are the COTS component likely to bottleneck bandwidth and power handling expansions. A single component suitable for the job may not be available, however, combination of frequency duplexing techniques with multiple circulators may be a way to compensate for the lack

of these components and achieve bandwidths beyond those of the current circulators.

The size of the design presented herein was guided by the COTS components used to build the BC-BFN. Future research could seek to minimize the volume that these components occupy and explore the different trade-offs that entails. Clearly, extensions to higher or lower frequencies are possible, but special care must be taken to ensure all engineering aspects are not detrimentally affected.

6.3.2 Spherical Lens Manifold

With miniaturization more of the BC-BFN subsystems could be placed together around a lens. Further studies could examine the BC-BFN's resilience to asymmetries different horns in the manifold might experience due to the presence of other feeds. Other active components turn this into a multiple input multiple output (MIMO) system and the cross interference between different elements should also be studied. [106] presents cancellation of this cross interference that combines analog circuitry taps with BC-BFN at the antenna layer to handle the self interference. Adaptations of said work along with decoupling techniques at the antenna's propagation layer could enable a full working STAR manifold.

6.3.3 RCS Cancellation

The mathematical framework developed to describe BFN RCS component in Chapter 5 was used to determine max-usable loop gain and model the response. However this same expression might be useful for shaping other characteristics of interest in the scattered pattern. Reference [107] provides a model for determining the phase delays needed to cancel out the residual RCS component and create a null in the total RCS in a specific direction. It would be interesting to use the model described in this thesis to account for coupling and higher order reflections in the system while still having the necessary equations to determine an exact solution, when possible, for the problem.

Bibliography

[1] K. E. Kolodziej, B. T. Perry, and J. S. Herd, "In-band full-duplex technology: Techniques and systems survey," IEEE Transactions on Microwave Theory and Techniques, vol. 67, no. 7, pp. 3025–3041, 2019.

[2] H. Saeidi-Manesh, S. Saeedi, M. Mirmozafari, G. Zhang, and H. H. Sigmarsson, "Design and fabrication of orthogonal-mode transducer using 3-d printing technology," IEEE Antennas and Wireless Propagation Letters, vol. 17, no. 11, pp. 2013–2016, 2018.

[3] A. M. Boifot, E. Lier, and T. Schaug-Pettersen, "Simple and broadband orthomode transducer (antenna feed)," IEE Proceedings H - Microwaves, Antennas and Propagation, vol. 137, no. 6, pp. 396–400, 1990.

[4] A. Navarrini and R. L. Plambeck, "A turnstile junction waveguide orthomode transducer," IEEE Transactions on Microwave Theory and Techniques, vol. 54, no. 1, pp. 272–277, 2006.

[5] V. Singh, A. Gadre, and S. Kumar, "Full duplex radios: Are we there yet?" in Proceedings of the 19th ACM Workshop on Hot Topics in Networks, ser. HotNets '20. New York, NY, USA: Association for Computing Machinery, 2020, p. 117–124. [Online]. Available: https://doi.org/10.1145/3422604.3425925

[6] K. L. Scherer, S. J. Watt, E. A. Alwan, A. A. Akhiyat, B. Dupaix, W. Khalil, and J. L. Volakis, "Simultaneous transmit and receive system architecture with four stages of cancellation," in 2015 IEEE International Symposium on Antennas and Propagation USNC/URSI National Radio Science Meeting, 2015, pp. 520–521.

[7] D. Korpi, M. Heino, C. Icheln, K. Haneda, and M. Valkama, "Compact inband full-duplex relays with beyond 100 db self-interference suppression: Enabling techniques and field measurements," IEEE Transactions on Antennas and Propagation, vol. 65, no. 2, pp. 960–965, 2017.

[8] B. F. Allen, N. Jastram, and D. Filipovic, "A reactive impedance surface for enhancing antenna isolation on cylindrical platforms," in 2017 IEEE International Symposium on Antennas and Propagation USNC/URSI National Radio Science Meeting, 2017, pp. 2661–2662.

[9] P. V. Prasannakumarr, "Wideband bi-static and monostatic star antenna systems," Ph.D. dissertation, Dept. Electrical, Computer and Energy Engineering, CU Boulder, Boulder, CO, 2019.

[10] S. Yen, L. B. Boskovic, and D. S. Filipovic, "Co-circularly polarized van atta array enabled by quasi-monostatic star antennas," IEEE Transactions on Antennas and Propagation, pp. 1–1, 2021.

[11] M. Elmansouri, P. Valaleprasannakumar, E. Tianang, E. Etellisi, and D. Filipovic, "Single and dual-polarized wideband simultaneous transmit and receive antenna system," in 2017 IEEE International Symposium on Antennas and Propagation USNC/URSI National Radio Science Meeting, 2017, pp. 1105–1106.

[12] D. S. Filipovic, M. A. Elmansouri, P. V. Prasannakumar, and E. G. Tianang., "Signal processing electronic attack rfic(spear)," CU Boulder Antenna Research Group, Boulder, CO, USA, Tech. Rep., 2018.

[13] R. N. Pack, "Wideband dual-polarized digital direction of arrival sensors," Ph.D. dissertation, Dept. Electrical, Computer and Energy Engineering, CU Boulder, Boulder, CO, 2019.

[14] H. Nawaz and I. Tekin, "Three ports microstrip patch antenna with dual linear and linear co-polarisation characteristics," Electronics Letters, vol. 53, no. 8, pp. 518–520, 2017.

[15] Y. Zhang and J. Li, "A dual-polarized antenna array with enhanced interport isolation for far-field wireless data and power transfer," IEEE Transactions on Vehicular Technology, vol. 67, no. 11, pp. 10 258–10 267, 2018.

[16] P. V. Prasannakumarr, "Passive front-ends for wideband millimeter wave electronic warfare," Ph.D. dissertation, Dept. Electrical, Computer and Energy Engineering, CU Boulder, Boulder, CO, 2014.

[17] M. E. Knox, "Single antenna full duplex communications using a common carrier," in WAMICON 2012 IEEE Wireless Microwave Technology Conference, 2012, pp. 1–6.

[18] E. A. Etellisi, M. A. Elmansouri, and D. S. Filipovic, "Wideband monostatic simultaneous transmit and receive (star) antenna," IEEE Transactions on Antennas and Propagation, vol. 64, no. 1, pp. 6–15, 2016.

[19] E. A. Etellisi, M. A. Elmansouri, and D. S. Filipović, "In-band full-duplex multimode lens-loaded eight-arm spiral antenna," IEEE Transactions on Antennas and Propagation, vol. 66, no. 4, pp. 2084–2089, 2018.

[20] M. A. Elmansouri, A. J. Kee, and D. S. Filipovic, "Wideband antenna array for simultaneous transmit and receive (star) applications," IEEE Antennas and Wireless Propagation Letters, vol. 16, pp. 1277–1280, 2017.

[21] A. Hovsepian, "Wideband, scanning array for simultaneous transmit and receive (star)," Master's thesis, Dept. Electrical and Computer Engineering, Ohio State University, Columbus, OH, 2017.

[22] A. Kee, M. Elmansouri, and D. S. Filipovic, "Circularly polarized pifa array for simultaneous transmit and receive applications," in 2017 IEEE International Symposium on Antennas and Propagation USNC/URSI National Radio Science Meeting, 2017, pp. 2303–2304.

[23] H. S. Jang, W. G. Lim, W. I. Son, S. Y. Cha, and J. W. Yu, "Microstrip patch array antenna with high isolation characteristic," Microwave and Optical Technology Letters, vol. 54, no. 4, pp. 973–976, 2012.

[24] J. Ha, M. A. Elmansouri, P. Valale Prasannakumar, and D. S. Filipovic, "Monostatic co-polarized full-duplex antenna with left- or right-hand circular polarization," IEEE Transactions on Antennas and Propagation, vol. 65, no. 10, pp. 5103–5111, 2017.

[25] A. K. Bhattacharyya, "Comparison between arrays of rotating linearly polarized elements and circularly polarized elements," IEEE Transactions on Antennas and Propagation, vol. 56, no. 9, pp. 2949–2954, 2008.

[26] E. A. Etellisi, M. A. Elmansouri, and D. S. Filipovic, "Wideband monostatic co-polarized co-channel simultaneous transmit and receive broadside circular array antenna," IEEE Transactions on Antennas and Propagation, vol. 67, no. 2, pp. 843–852, 2019.

[27] K. E. Kolodziej, P. T. Hurst, A. J. Fenn, and L. I. Parad, "Ring array antenna with optimized beamformer for simultaneous transmit and receive," in Proceedings of the 2012 IEEE International Symposium on Antennas and Propagation, 2012, pp. 1–2.

[28] K. E. Kolodziej and B. T. Perry, "Vehicle-mounted star antenna isolation performance," in 2015 IEEE International Symposium on Antennas and Propagation USNC/URSI National Radio Science Meeting, 2015, pp. 1602–1603.

[29] R. Lian, T. Shih, Y. Yin, and N. Behdad, "A high-isolation, ultra-wideband simultaneous transmit and receive antenna with monopole-like radiation characteristics," IEEE Transactions on Antennas and Propagation, vol. 66, no. 2, pp. 1002–1007, 2018.

[30] E. A. Etellisi, M. A. Elmansouri, and D. Filipovic, "Broadband full-duplex monostatic circular-antenna arrays: Circular arrays reaching simultaneous transmit and receive operation," IEEE Antennas and Propagation Magazine, vol. 60, no. 5, pp. 62–77, 2018.

[31] A. H. Abdelrahman and D. S. Filipovic, "Antenna system for full-duplex operation of handheld radios," IEEE Transactions on Antennas and Propagation, vol. 67, no. 1, pp. 522–530, 2019.

[32] C. A. Mulero Hernandez, L. B. Boskovic, M. A. Elmansouri, M. I. Ignatenko, and D. S. Filipovic, "Fixed and steerable beam dual-polarized lens antenna with high tx to rx isolation," IEEE Transactions on Antennas and Propagation, 2021.

[33] P. Valale Prasannakumar, M. A. Elmansouri, and D. S. Filipovic, "Broadband reflector antenna with high isolation feed for full-duplex applications," IEEE Transactions on Antennas and Propagation, vol. 66, no. 5, pp. 2281–2290, 2018.

[34] E. A. Etellisi, M. A. Elmansouri, and D. S. Filipović, "Wideband multimode monostatic spiral antenna star subsystem," IEEE Transactions on Antennas and Propagation, vol. 65, no. 4, pp. 1845–1854, 2017.

[35] M. A. Elmansouri, A. J. Kee, and D. S. Filipovic, "Wideband antenna array for simultaneous transmit and receive (star) applications," IEEE Antennas and Wireless Propagation Letters, vol. 16, pp. 1277–1280, 2017.

[36] P. Afanasyev, S. Matitsine, V. Sledkov, P. Lagoiski, L. Matytsine, T. DeMarco, and T.-T. Chia, "Multi-beam luneburg lens antenna for cellular communications," in 2015 9th European Conference on Antennas and Propagation (EuCAP), 2015, pp. 1–4.

[37] B. Schoenlinner, X. Wu, J. Ebling, G. Eleftheriades, and G. Rebeiz, "Wide-scan spherical-lens antennas for automotive radars," IEEE Transactions on Microwave Theory and Techniques, vol. 50, no. 9, pp. 2166–2175, 2002.

[38] G. Peeler and H. Coleman, "Microwave stepped-index luneberg lenses," IRE Transactions on Antennas and Propagation, vol. 6, no. 2, pp. 202–207, 1958.

[39] B. Fuchs, L. Le Coq, O. Lafond, S. Rondineau, and M. Himdi, "Design optimization of multishell luneburg lenses," IEEE Transactions on Antennas and Propagation, vol. 55, no. 2, pp. 283–289, 2007.

[40] S. Baev, B. Hadjistamov, and P. Dankov, "Lüneburg lenses as communication antennas," vol. 102, pp. 67–84, 01 2009.

[41] A. Sayanskiy, S. Glybovski, V. P. Akimov, D. Filonov, P. Belov, and I. Meshkovskiy, "Broadband 3-d luneburg lenses based on metamaterials of radially diverging dielectric rods," IEEE Antennas and Wireless Propagation Letters, vol. 16, pp. 1520–1523, 2017.

[42] Y. Li, L. Ge, M. Chen, Z. Zhang, Z. Li, and J. Wang, "Multibeam 3-d-printed luneburg lens fed by magnetoelectric dipole antennas for millimeter-wave mimo applications," IEEE Transactions on Antennas and Propagation, vol. 67, no. 5, pp. 2923–2933, 2019.

[43] C. Wang, J. Wu, and Y. Guo, "A 3-d-printed multibeam dual circularly polarized luneburg lens antenna based on quasi-icosahedron models for ka-band wireless applications," IEEE Transactions on Antennas and Propagation, vol. 68, no. 8, pp. 5807–5815, 2020.

[44] C. Mateo-Segura, A. Dyke, H. Dyke, S. Haq, and Y. Hao, "Flat luneburg lens via transformation optics for directive antenna applications," IEEE Transactions on Antennas and Propagation, vol. 62, no. 4, pp. 1945–1953, 2014.

[45] M. Imbert, J. Romeu, M. Baquero-Escudero, M. Martinez-Ingles, J. Molina-Garcia-Pardo, and L. Jofre, "Assessment of ltcc-based dielectric flat lens antennas and switched-beam arrays for future 5g millimeter-wave communication systems," IEEE Transactions on Antennas and Propagation, vol. 65, no. 12, pp. 6453–6473, 2017.

[46] Y. He and G. V. Eleftheriades, "Matched, low-loss, and wideband graded-index flat lenses for millimeter-wave applications," IEEE Transactions on Antennas and Propagation, vol. 66, no. 3, pp. 1114–1123, 2018.

[47] S. Zhang, Y. Vardaxoglou, W. Whittow, and R. Mittra, "3d-printed graded index lens for rf applications," in 2016 International Symposium on Antennas and Propagation (ISAP), 2016, pp. 90–91.

[48] K. V. Hoel and S. Kristoffersen, "Characterization of variable density 3d printed materials for broadband grin lenses," in 2017 IEEE International Symposium on Antennas and Propagation USNC/URSI National Radio Science Meeting, 2017, pp. 2643–2644.

[49] K. V. Hoel, S. Kristoffersen, M. Ignatenko, and D. Filipovic, "Half ellipsoid luneburg grin dielectric lens loaded double ridged horn antenna," in 12th European Conference on Antennas and Propagation (EuCAP 2018), 2018, pp. 1–5.

[50] S. G. Wirth and I. L. Morrow, "Near-field microwave sensor composed of 3d printed antennas and lenses," in 2018 IEEE MTT-S International Conference on Numerical Electromagnetic and Multiphysics Modeling and Optimization (NEMO), 2018, pp. 1–4.

[51] S. Manafi, "Enabling ridge waveguide technology for wideband millimeter-wave decoys," Ph.D. dissertation, Dept. Electrical, Computer and Energy Engineering, CU Boulder, Boulder, CO, 2018.

[52] L. Van Atta, "Electromagnetic reflector," United States of America Patent 2,908,002, October 6, 1959.

[53] R. C. Hansen, "Communications satellites using arrays," Proceedings of the IRE, vol. 49, no. 6, pp. 1066–1074, 1961.

[54] S. Andre and D. Leonard, "An active retrodirective array for satellite communications," IEEE Transactions on Antennas and Propagation, vol. 12, no. 2, pp. 181–186, 1964.

[55] A. F. Snyder, "Active retrodirective antenna array employing spiral elements and tunnel diode amplifiers," United States of America Patent 3,508,269, April 21, 1970.

[56] R. Y. Miyamoto and T. Itoh, "Retrodirective arrays for wireless communications," IEEE Microwave Magazine, vol. 3, no. 1, pp. 71–79, 2002.

[57] Shyh-Jong Chung, Shing-Ming Chen, and Yang-Chang Lee, "A novel bi-directional amplifier with applications in active van atta retrodirective arrays," IEEE Transactions on Microwave Theory and Techniques, vol. 51, no. 2, pp. 542–547, 2003.

[58] Y.-C. Guo, F. Wei, and L. Chen, "Retrodirective array technology," Progress in Electromagnetics Research B, vol. 5, pp. 153–167, 01 2008.

[59] C. Pon, "Retrodirective array using the heterodyne technique," IEEE Transactions on Antennas and Propagation, vol. 12, no. 2, pp. 176–180, 1964.

[60] J. I. Bohnert and H. Coleman, "Applications of the luneberg lens," Naval Research Laboratory, Washington D.C., Tech. Rep. 7, 3 1957.

[61] C. S. Liang, D. A. Streater, Jian-Ming Jin, E. Dunn, and T. Rozendal, "A quantitative study of luneberg-lens reflectors," IEEE Antennas and Propagation Magazine, vol. 47, no. 2, pp. 30–42, 2005.

[62] C. S. Liang, D. A. Streater, Jian-Ming Jin, E. Dunn, and T. Rozendal, "Ground-plane-backed hemispherical luneberg-lens reflector," IEEE Antennas and Propagation Magazine, vol. 48, no. 1, pp. 37–49, 2006.

[63] L. Xue, H. I. Cantu, and V. F. Fusco, "Two-dimensional luneburg lens rcs augmentation using mmic reflection amplifier," in 2007 Loughborough Antennas and Propagation Conference, 2007, pp. 81–84.

[64] Ansys, "Anssys electromagnetics suite, hfss."

[65] Altair, "Feko."

[66] Dasault Systemes Deutschland GmbH, "Cst microwave studio."

[67] , "Python 2.7.18." [Online]. Available: https://docs.python.org/2.7/

[68] ——, "Scipy." [Online]. Available: https://www.scipy.org/

[69] Alexander Arsenovic, "scikit-rf." [Online]. Available: https://scikit-rf.readthedocs.io

[70] "Home," Jan 2021. [Online]. Available: https://luneberg.com/?lang=en

[71] S. Khaledian, F. Farzami, B. Smida, and D. Erricolo, "Inherent self-interference cancellation for in-band full-duplex single-antenna systems," IEEE Transactions on Microwave Theory and Techniques, vol. 66, no. 6, pp. 2842–2850, 2018.

[72] C. A. Mulero Hernandez, M. Elmansouri, and D. S. Filipovic, "High-directivity beam-steerable lens antenna for simultaneous transmit and receive," in 2019 IEEE International Symposium on Phased Array System Technology (PAST), 2019, pp. 1–5.

[73] H. Jin, Y. M. Huang, H. Jin, and K. Wu, "E-band substrate integrated waveguide orthomode transducer integrated with dual-polarized horn antenna," IEEE Transactions on Antennas and Propagation, vol. 66, no. 5, pp. 2291–2298, 2018.

[74] M. A. Abdelaal, S. I. Shams, and A. A. Kishk, "Asymmetric compact omt for x-band sar applications," IEEE Transactions on Microwave Theory and Techniques, vol. 66, no. 4, pp. 1856–1863, 2018.

[75] J. A. Ruiz-Cruz, J. R. Montejo-Garai, C. A. Leal-Sevillano, and J. M. Rebollar, "Ortho-mode transducers with folded double-symmetry junctions for broadband and compact antenna feeds," IEEE Transactions on Antennas and Propagation, vol. 66, no. 3, pp. 1160–1168, 2018.

[76] C. Montgomery, R. Dicke, and E. Purcell, Principles of Microwave Circuits. Peter Peregrinus on behalf of the Institution of Electrcial Enginners, 1987, pp. 459–466.

[77] G. Engargiola and A. Navarrini, "K-band orthomode transducer with waveguide ports and balanced coaxial probes," IEEE Transactions on Microwave Theory and Techniques, vol. 53, no. 5, pp. 1792–1801, 2005.

[78] N. Jastram, M. A. Altarifi, L. Boskovic, and D. S. Filipovic, "On the split-block realization of millimeter-wave ridge waveguide components," IEEE Microwave and Wireless Components Letters, vol. 28, no. 4, pp. 296–298, 2018.

[79] S. P. Morgan, "General solution of the luneberg lens problem," Journal of Applied Physics, vol. 29, no. 9, pp. 1358–1368, 1958.

[80] A. Fletcher, T. Murphy, A. Young, and L. Rosenhead, "Solutions of two optical problems," Proceedings of the Royal Society of London. Series A. Mathematical and Physical Sciences, vol. 223, no. 1153, pp. 216–225, 1954. [Online]. Available: https://royalsocietypublishing.org/doi/abs/10.1098/rspa.1954.0110

[81] A. V. Boriskin, A. Vorobyov, and R. Sauleau, "Two-shell radially symmetric dielectric lenses as low-cost analogs of the luneburg lens," IEEE Transactions on Antennas and Propagation, vol. 59, no. 8, pp. 3089–3093, 2011.

[82] B. Simakauskas, "Phase center stabillization of a horn antenna and its application in a luneburg lens feed array," Master's thesis, Dept. Electrical, Computer and Energy Engineering, CU Boulder, Boulder, CO, 2015.

[83] Shung-Wu Lee and Y. Rahmat-Samii, "Simple formulas for designing an offset multibeam parabolic reflector," IEEE Transactions on Antennas and Propagation, vol. 29, no. 3, pp. 472–478, 1981.

[84] D. Gray, J. Thornton, H. Tsuji, and Y. Fujino, "Scalar feeds for 8 wavelength diameter homogeneous lenses," in 2009 IEEE Antennas and Propagation Society International Symposium, 2009, pp. 1–4.

[85] D. Gray and J. Thornton, "Scan performance of low index lens reflector," in IET International Radar Conference 2013, 2013, pp. 1–6.

[86] J. Thorton and K. C. Huang, Modern Lens Antennas for Communications Engineering. Wiley, 2013, pp. 228–232.

[87] H. Barba Molina, J. Gonzalez Marin, and J. Hesselbarth, "Modified planar luneburg lens millimetre-wave antenna for wide-angle beam scan having feed locations on a straight line," IET Microwaves, Antennas & Propagation, vol. 11, no. 10, pp. 1462–1468, 2017. [Online]. Available: https://ietresearch.onlinelibrary.wiley.com/doi/abs/10.1049/iet-map.2017.0005

[88] J. G. Marin and J. Hesselbarth, "Lens antenna with planar focal surface for wide-angle beam-steering application," IEEE Transactions on Antennas and Propagation, vol. 67, no. 4, pp. 2757–2762, 2019.

[89] A. Petosa and A. Ittipiboon, "Design and performance of a perforated dielectric fresnel lens," vol. 150, no. 5, 1994, pp. 309–314.

[90] W. B. Weir, "Automatic measurement of complex dielectric constant and permeability at microwave frequencies," Proceedings of the IEEE, vol. 62, no. 1, pp. 33–36, 1974.

[91] P. Keshavarzian, M. Okoniewski, and J. Nielsen, "Active phase-conjugating rotman lens with reflection amplifiers for backscattering enhancement," IEEE Transactions on Microwave Theory and Techniques, vol. 68, no. 1, pp. 405–413, 2020.

[92] D. C. Jenn and Seunghoon Lee, "Inband scattering from arrays with series feed networks," IEEE Transactions on Antennas and Propagation, vol. 43, no. 8, pp. 867–873, 1995.

[93] D. C. Jenn and V. Flokas, "In-band scattering from arrays with parallel feed networks," IEEE Transactions on Antennas and Propagation, vol. 44, no. 2, pp. 172–178, 1996.

[94] H. L. Sneha, H. Singh, and R. M. Jha, "Scattering analysis of an unequal-length dipole array in the presence of mutual coupling," IEEE Antennas and Propagation Magazine, vol. 55, no. 4, pp. 333–351, 2013.

[95] C. A. Balanis, Advaned Engineering Electromagnetics. Wiley, 2012, no. 2.

[96] R. B. Green, "The general theory of antenna scattering," Ph.D. dissertation, Ohio State University, 1963.

[97] R. C. Hansen, "Relationships between antennas as scatterers and as radiators," Proceedings of the IEEE, vol. 77, no. 5, pp. 659–662, 1989.

[98] B. A. Munk, On Radar Cross Section of Antennas in General. John Wiley and Sons, Ltd, 2005, ch. 2, pp. 15–55. [Online]. Available: https://onlinelibrary.wiley.com/doi/abs/10.1002/0471457531.ch2

[99] C. Knop and G. Lichtenwalter, "Radar echo reduction using circulators," IEEE Transactions on Antennas and Propagation, vol. 14, no. 6, pp. 789–790, 1966.

[100] N. Nakamoto, T. Takahashi, T. Nomura, M. Otsuka, and H. Miyashita, "A method to measure the antenna mode and structural mode for antenna rcs reduction using circulator and phase shifter," in 2014 International Symposium on Antennas and Propagation Conference Proceedings, 2014, pp. 21–22.

[101] N. Nakamoto, T. Takahashi, T. Fukasawa, and N. Yoneda, "Rcs reduction of array antenna using circulator and phase shifter," in 2017 IEEE Conference on Antenna Measurements Applications (CAMA), 2017, pp. 190–193.

[102] E. F. Kuester, Theory of Waveguides and Transmission Lines, 2017, ch. 3.

[103] C. Balanis, Antenna Theory: Analysis and Design. Wiley, 2012. [Online]. Available: https://books.google.com/books?id=v1PSZ48DnuEC

[104] D. M. Pozar, Microwave Engineering, 4th ed. Wiley, 2013.

[105] P. J. Olver and C. Shakiban, Applied Linear Algebra, 2nd ed. Springer, Cham, 2018, ch. 9, pp. 475–563.

[106] M. E. Knox, "Simplified tapped delay line architecture for active cancellation in a 2×2 ibfd mimo transceiver," in 2019 IEEE 20th Wireless and Microwave Technology Conference (WAMICON), 2019, pp. 1–5.

[107] N. Nakamoto, T. Takahashi, T. Fukasawa, N. Yoneda, and H. Miyashita, "Rcs synthesis of array antenna with circulators and phase shifters and measurement method for deterministic rcs reduction," IEEE Transactions on Antennas and Propagation, vol. 69, no. 1, pp. 135–145, 2021.